2021

Radioimmunoconjugate for cancer molecular imaging

Nouri Elmekharam
Virginia Commonwealth University

Elmekharam, Nouri

Radioimmunoconjugate for cancer molecular imaging

A dissertation submitted in partial fulfillment of the requirements for the degree of PhD at Virginia Commonwealth University.

by

NOURI ELMEKHARAM

Director: Professor Jamal Zweit & Professor Nicholas Farrell
Department of Radiology & Chemistry

Virginia Commonwealth University
Richmond, Virginia
May 5th, 2021

Dedication

In loving memory of my father whom I miss every day, knowing that if he were present, he would be very happy to see the completion of this process.

To my mother for her ongoing love and support, for whom I am so glad and thankful to God that she can be here and see this accomplishment which would not have happened without her care, support and encouragement.

Acknowledgement

I would like to express my sincere gratitude to Dr. Zweit for the opportunity to pursue my doctoral studies in his laboratory. I am especially thankful for his guidance and kind support and positive attitude which drove me to continue my studies and overcome challenges.

Also, I would like to thank Dr. Sundaresan Gobalakrishnan for his support, and guidance for experimental design and using imaging tools, his experience and guidance were invaluable to my work.

I would like to thank UVA Late Dr.John C, Herr Lab members for providing anti-SAS1B antibodies for this project.

I wish to thank the members of my advisory committee, Dr. Nicholas P Farrell, Dr. Masoud Manjili, Dr. Sundaresan Gobalakrishnan and Dr. Youngman Oh for agreeing to be members in PhD Committee and provide me with guidance, encouragement and feedback on my research work. Thank you for challenging me to think critically about my research.

Special thanks for Dr. Youngamn for providing us the monoclonal antibody IgG.

Special thanks to Dr. J. Turner, Director of Instrumentation at chemistry department for his help for using UV/Vis analyzer.

I would like to thank my past and present colleagues in Dr. Zweit's laboratory, Philip McDonagh PhD , Huseyin.Cicek, Celina Thadigiri for their help in using HPLC and TLC and thank to Li Wang for her help in cell culture and animal work to my friend and colleague Ali Gawi for been together spurting each other.

I wish to extend my deepest gratitude to my family: Thank you to my wife Dr.Amal Gebali whose love, patience, and care made hard times easier and good times better. Thank you for taking care of the kids, believing in me, holding my hand, and supporting my hopes and dreams. Thank you to my two daughters Ranim and Sara and two sons Anas and Elyas for your endless love and for your patience and understanding of my busy time during my graduate studies.

Table of Contents

List of Tables

List of Figures

List of Schemes

Page

List of Abbreviations

SAS1B	Sperm acrosomal SLLP1 binding protein
^{89}Zr	Zircunum-89
^{67}Cu	Copper-67
p-SCN-Bn- DOTA	Para Isothiocyanatobenzyl-1, 4, 7, 10-tetraazacyclododecane tetra acetic acid
DFO	Deferoxamine
PET	Positron emission tomography
SPECT	Single-photon emission computed tomography
MRI	Magnetic resonance imaging
HPLC	High-performance liquid chromatography
TLC	Thin-layer chromatography
UV	Ultra Violet
UVA	University of Virginia
FDA	Food and Drug Administration
NCBI	National Center for Biotechnology Information
mAbs	Monoclonal antibodies
SNU539	Seoul National University cell line
DNA	Deoxyribonucleic acid
CTLA4	Cytotoxic T-lymphocyte-associated protein 4
PD-1	Programmed cell death protein 1
PD-L1	Programmed death-ligand 1
FDA	Food and Drug Administration
DNA	Deoxyribonucleic acid
RIT	Radioimmunotherapy
AE	Auger electron
LET	Liner energy transfer
CD20	B-lymphocyte antigen

MeV	Megaelectronvolt
keV	Kiloelectronvolt
NLS	Nuclear localization sequence
kDa	Kilodalton
Fabs	Antibodies fragments
Fc	Fragment crystallizable region
VH	Heavy chain variable
LH	Light chain variable
BFC	Bifunctional chelators
α++	Alpha particule
β-	Beta minus particule
β+	Beta plus particule (Positron)
¥	Gamma photon
uCi	Micro curie
%ID/g	Percent injected dose per gram of tissue
NIRdye800CW	Near-infrared dye
A549	Non-Small Cell Lung Carcinoma
Sk-OV3	Ovarian cancer cell line
HOPO	Octadentate hydroxypyridinone ligand

Abstract

RADIOMMUNOCONJUGATE FOR CANCER MOLECULAR IMAGING

By Nouri Elmekharam, MSc.

A dissertation submitted in partial fulfillment of the requirements for the degree of Doctor of Philosophy in Chemical Biology at Virginia Commonwealth University.

Virginia Commonwealth University, 2021

Major Director: Professor Jamal Zweit
Department of Radiology

Over expression of Sperm Acrosomal SLLP1 Binding protein (SAS1B) on the surface of uterine cancer and the availability of different anti-SAS1B monoclonal antibodies (mAbs) that specifically bind to it, offered an opportunity to label these antibodies with radionuclides for cancer imaging. Although optimizing *in vivo* stable radiolabeling is challenging, imaging this type of aggressive cancer will improve the treatment strategy. The objective of this work is to develop a radiolabeled anti-SAS1B antibodies with Zircunum-89 (^{89}Zr) and Copper-67 (^{67}Cu) and determine, *in vitro* and *in vivo* their uptake and biodistribution. Two anti-SAS1B monoclonal antibodies (SB2, and SB5) were labeled indirectly with ^{89}Zr and ^{67}Cu, using Deferoxamine (DFO) and Para Isothiocyanatobenzyl-1, 4, 7, 10-tetraazacyclododecane tetra acetic acid (p-SCN-Bn-DOTA) respectively. Different molar ratios of anti-SAS1B to the linker were investigated for conjugation, (1:3, 1:5, or 1:10) to determine the optimum conjugation molar ratio to take forward for labeling. The optimized conjugate was used to produce a radiolabeled mAb which was used for both *in vitro* cell uptake experiments and *in vivo* tumor imaging and biodistribution study. Results show specific uterine cancer cell uptake of radiolabeled

SB2 and SB5 indicating the specificity of anti-SAS1B to its target SAS1B surface antigen expressed on SNU539 uterine cancers cells.

[^{89}Zr]-DFO-SB5 PET imaging revealed uptake in the SNU539 tumor xenograft, albeit with minimal uptake. Uptake was also observed in bones and this is more likely due to detachment of the ^{89}Zr from DFO, and subsequent accumulation in bone. The biodistribution profile from imaging data was reflected in the *ex vivo* biodistribution of [^{89}Zr]-DFO-SB5.

The second mAb SB2 was radiolabeled indirectly using [^{67}Cu]-DOTA and such radio-conjugate was used to assess its uptake by SNU539 and Sk-OV3 cancer cell lines, which express SAS1B antigen. The [^{67}Cu]-DOTA-SB2 was taken up by both cell lines and this uptake was significantly higher than that of ^{67}CuCl2 or [^{67}Cu]-DOTA, indicating more specific uptake in the case of radiolabeled Mab.

In the absence of radionuclides, the MAb SB2 was conjugated to the near-infrared (NIR) fluorescence dye (IR800CW) to enable the potential for optical imaging. Using fluorescence microscopy, SB2 mAb labeled with the NIR dye showed more binding to SNU539 and Sk-OV3 and no binding to A549, which is consistent with its lack of SAS1B expression. Presence of fluorescence signals in uterine cancer cells that express SAS1B surface antigens compared with cells do not express SAS1B as negative control.

The labeled anti-SAS1B antibodies SB2 and SB5 were evaluated *in vitro* and *in vivo*. The results demonstrated the specific binding of both labeled antibodies to the surface uterine cancer receptors (SAS1B) through *in vitro* cell uptake and *in vivo* tumor uptake.

Labeled anti-SAS1B mAbs with radionuclides or fluorescent probes could yield an imaging version of the mAb that can be used to determine SAS1B receptor status in such tumors. Such determination could impact more individualized treatment of SAS1**B**-expressing cancers.

CHAPTER 1: INTRODUCTION

1.1 Introduction

The challenge of accurate whole-body cancer detection and reporting on biological changes, for example changes in tumor metabolic activity, has empowered the development of molecular imaging paradigms. These approaches are capable of studying the biology underlying the progression of disease and its response to therapy. Over the last two decades, molecular imaging has played an important role in the management of cancer patients, aiding in early detection, accurate staging, and objective monitoring of response to treatment [1]. A number of molecular imaging modalities have been used to support cancer diagnosis and therapy. These include SPECT, PET, MRI, and optical imaging using fluorescence or bioluminescence. These modalities have the capabilities to image multiple targets using affinity probes labeled with different radioisotopes or fluorescence agents. Radioisotopes based imaging engages three important components: radioisotope, carrier, and binding target. Many radioisotopes have been used for imaging and therapy, based on their specific properties [3]. Developments in antibodies production and engineering has led to the availability of antibodies against a variety of targets, such as growth factors, cytokines, and cell surface receptors, making antibodies useful in molecular imaging in a variety of disease models [4] [5]. Targeted antibodies for tumor imaging are a promising approach to evaluating and improving cancer therapy [6]. More than 70 such antibodies were approved by the FDA for clinical use [5]. Many human tumors overexpress a variety of surface cell receptors which have been used as a basis of receptor-targeted imaging [7]. Tumor receptor imaging offers valuable information, including evaluation of the entire tumor burden as well as characterization of the heterogeneity of tumor receptor expression. Tumor receptors have been some of the earliest targets for tumor imaging and therapy with notable successes in cancer therapy and imaging, for example, endocrine-related cancers such as breast, prostate, and thyroid cancers. The high affinity of radiolabeled antibody for receptors on tumor cells has caused particular interest in targeting strategies [8]. An advantage of labeling antibodies is their well-defined structure with an abundance of functional amino acids capable of binding to modified functional groups of a linker used for labeling antibodies indirectly by radionuclides [9]. Although there is potential in using radiolabeled antibodies for imaging and therapy, it is still challenging to synthesize a high yield of radiolabeling stable *in vitro* and *in vivo* [10] [11]. Many factors can affect antibody conjugation, labeling, and *in vivo* biodistribution [12].

A novel tumor-selective cell surface biomarker, SAS1B (sperm acrosomal SLLP1 binding protein), has been discovered and patented at University of Virginia (UVA) [13]. Initially, SAS1B was found to be expressed on ovary and oocytes and was restricted among adult tissue [14],[15]. In addition, SAS1B was not detected in a variety of additional normal human tissues and no ASTL expressed sequence tags have been deposited in the NCBI Unigene database from normal tissues [13] [14]. Studies *in vitro* identified that the SAS1B target is overexpressed on the surface of a wide range of aggressive malignancies such as uterine, ovarian, pancreatic, and renal cancers [13]. Different Anti-SAS1B mAbs were designed at UVA and investigated for targeting SAS1B expressed on the surface of cancer cell lines [16]. Anti-SAS1B antibodies provide an attractive molecular target to develop highly tumor-specific radio-immuno-pharmaceuticals.

In this project, two mAbs (SB2 and SB5) were selected for labeling with radionuclides Zirconumm-89 (^{89}Zr) and cooper-67 (^{67}Cu) and used *in vitro* and *in vivo* work. The work described here builds on the development of anti-SAS1B mAbs, carried out in our collaborator's laboratory at UVA, by developing a radiolabeled version of the SAS1B mAb (SB2 and SB5) and investigating its targeting credentials and overall pharmacokinetics *in vivo* animal tumor model of uterine cancer. This is being investigated through both *ex vivo* biodistribution and *in vivo* molecular imaging studies.

1.2 Hypothesis

SAS1B antigen has been shown (in vitro) to be overexpressed on the surface of a number of aggressive malignancies, including uterine, ovarian and pancreatic cancer. Monoclonal antibodies have been produced against SAS1B target antigen. We hypothesize that the development of a radiolabeled version of the MAbs would serve as a tool to study the binding of the radiolabeled Mab to SNU539 tumors expressing SAS1B *in vivo*.

The overall objective is to evaluate the biological behavior and targeting of radiolabeled anti-SAS1B mAb (SB2/SB5) in uterine cancer xenografts expressing the SAS1B protein. In order to achieve this, a stable radioimmunoconjugate has to be developed and characterized. Both PET and SPECT radionuclides will be used to produce radioimmunoconjugates that can be evaluated by *in vivo* molecular imaging. The *in vivo* results obtained will complement the information obtained from *in vitro* assays and unravel the kinetics of delivery, retention, and clearance following IV administration of the radiolabeled conjugate. This objective will be investigated through the following specific aims.

1.3 Specific Aims.

1.3.1 Aim 1: Conjugation and Radiolabeling

The production of radiolabeled anti-SAS1B mAbs involves two steps: i) conjugation of the bi-functional chelate to the mAb through covalent attachment; and ii) radiolabeling of the conjugated mAb by the radionuclide. Radiolabeled conjugates were evaluated by High-performance liquid chromatography (HPLC) with UV and Radio-detection (radio-HPLC) in terms of reaction yields, radiochemical and chemical purity. Radio-TLC was used to determine radiolabeling yield and determine radiochemical purity, and this method will be validated by the radio-HPLC data. Further purification of the radiolabeled conjugate will be carried out using PD10 desalting columns to separate the radiolabeled mAb from low molecular weight species, such as free radionuclide and non-mAb associated radioactive signal.

1.3.2 Aim 2: *In Vitro* Evaluation

The *in vitro* cell uptake and retention of the radiolabeled mAb will be evaluated using uterine cancers cell lines SNU539 (Seoul National University) **which is expressing the SAS1B protein expressed in the SAS1B.)** Uptake kinetics was determined by incubating the radiolabeled mAb and measuring the radioactivity, as a function of time, using radiotracer analysis. The immunoreactive fraction of the radiolabeled mAb will also be evaluated and compared to that of the unlabeled mAb, in order to determine the effect of radiolabeling on the immunoreactivity of the mAb.

1.3.3 Aims 3: *In Vivo* Evaluation

SNU539 uterine cancer cells will be implanted subcutaneously in nude mice and allowed to grow to produce xenografts, as tumors expressing the SAS1B target protein. The radiolabeled mAb against SAS1B antigen will be evaluated in this model using either PET or SPECT live animal imaging and validated by *ex vivo* biodistribution analysis of tissues including tumors.

CHAPTER 2: BACKGROUND

2.1 Cancer

According to the WHO, cancer is a leading cause of death worldwide. There were about 10 million deaths in 2020 and the estimation of new cases in 2021 was about 17 million worldwide. The American Cancer Society estimates that in 2021, approximately 1,898,160 Americans will be diagnosed with cancer and of those, approximately 608,570 are expected to die [2]. Poor outcomes from the disease are exacerbated by a combination of failure to detect cancer until too late and ineffective treatment options [3].

Cancer is a broad term describing a large group of diseases that result when cellular changes cause the uncontrolled growth and division of cells with the ability to infiltrate and destroy normal body tissue. Normal cells have a specific life cycle, growth, division, and death in a manner which is determined by the type of cell. A cell receives instructions to die through a natural and beneficial phenomenon called apoptosis, which allows the body to replace it with a newer cell that functions better [4]. Cancer disrupts the apoptosis process. Cells continue to divide without stopping. Most cancers begin as a result of changes or mutations in the gene which happen over a person’s lifetime, such as errors occurring during cell division or damage to DNA caused by certain environmental exposures to chemicals, certain radiation, and specific viruses [5]. Cancer can sometimes begin as a result of faulty genetic changes inherited and passed down in families, but this is rare. Depending on the type of cancer, some involve rapid cell growth while others grow and divide at a slower rate. Cancers are named based upon the area where they begin and the types of cells they produce. Some forms of cancer result in visible growths called tumors. Others, such as cancers of the blood, do not form tumors.

Although advances are being made in the area of cancer diagnosis, treatment options are still limited [6].

2.2 Cancer Imaging

Imaging plays an important role in comprehensive cancer care with many advantages including real time monitoring, accessibility without tissue destruction, minimal or no invasiveness, and the ability to function over wide ranges of time and size scales involved in biological and pathological processes [7]. The major contributors to a reduction in mortality for certain cancers are early detection and monitoring the treatment of cancer through screening based on imaging [8]. The development in molecular imaging increases imaging speed to match that of physiological processes [9]. For instance FDG-PET, and subsequently FDG-PET/CT, has become a keystone in several oncologic procedures such as tumor staging and restaging, treatment efficacy assessment during or after treatment end and radiotherapy planning [10]. Image guided and targeted minimally invasive therapy has the promise to improve outcome and reduce collateral effects [11]. The research activities in targeted imaging of receptors, gene therapy expression, and cancer stem cells have been increased and this might translate into clinical use in the next decades [7],[12]. Close collaboration between academia and biotechnology, information technology and pharmaceutical industries will lead to development of targeted imaging and therapeutic agents.

2.3 Cancer Treatment Modalities

Currently there are many modalities for cancer treatments, and appropriate applications depend upon the specific type of cancer [13]. Established treatment approaches include surgery, chemotherapy, and radiotherapy. Chemotherapy and radiotherapy have been employed for many years to kill cancer cells, but in most cases the treatment is more effective in prolonging survival [14].Therefore, many cases require a combination of treatments, such as surgery with chemotherapy and/ or radiation therapy [15]. Despite dose-limiting toxicity and low specificity, prolonged survival has been achieved for many cancer patients [16]. Unfortunately, many patients ultimately die due to cancer recurrence, severe side effects of the treatment, or a combination of both. A number of therapeutic approaches have been proposed in order to minimize the chances of relapse in cancer patients [17]. These include hormone-based therapy, gene therapy, cell-based therapy including stem cell therapy, and immunotherapy [18],[19]. Cancer treatment based on immunotherapy has been introduced to specifically target cancer cells and minimize side effects induced by conventional treatment [20].

2.3.1 Surgery

Surgery has been the first standard of care for cancer diagnosis and treatment for more than a century [21]. Surgery to establish diagnosis is usually done through a procedure in which a small piece of tissue is removed and sent to a histopathology laboratory where it is examined for the presence of cancer cells, type of cancer cells, and the stage. When cancer is diagnosed in the early stages, surgery to remove the tumor could be the best option and completely curative [22]. However, surgery is the only option for a solid tumor and local treatment. Therefore, the use of surgery is dependent on the location of the tumor and the stage. When the cancer is late stage, it has metastasized into other areas and invaded other tissues. In that case, surgery is not the only option for treatment, and in most cases, the cancer is not completely curative [22]. Sometimes surgery is done to prevent cancer when the patient is at high risk for a particular type of cancer based on family history and genetic studies [23]. For example, surgery to remove a breast would be appropriate in a woman with a high risk of breast cancer [24]. Also, surgery could be done to treat a problem caused by advanced cancer. This is called palliative, or supportive, surgery and is used along with other treatments to correct a problem that is causing additional discomfort or disability [25]. For instance, surgery done to remove a blockage in the abdomen when the cancer has grown large enough to block (obstruct) the intestine. In some cases, palliative surgery is done to treat pain when the pain is hard to control with medicine alone. In most cases when cancer is in the late stages, surgery is done not to treat or cure the cancer but to bring relief and help the patient to feel better.

2.3.2 Chemotherapy

Chemotherapy uses chemical agents (anti-cancer or cytotoxic drugs) to inhibit vigorously growing malignant cells [26]. Chemotherapy is a systemic method and, in most cases, is recommended for cancer that has already spread to other areas of the body. Chemotherapy drugs interact with cancer cells through different ways. Some of the drugs interfere primarily with DNA synthesis and mitosis (cell cycle phases M and S), while other drugs work by preventing cells from dividing [27]. Based on their chemical structures and the way they act, chemotherapy agents divide into different categories. Alkylating agents were the first anti-cancer drugs used and the most commonly-used anticancer drugs in chemotherapy [28]. These agents act during all phases of the cell cycle, directly on DNA, causing cross-linking of DNA strands, abnormal base pairing, or DNA strand breaks, thus preventing the cell from dividing [29]. Antimetabolites are agents altering the function of enzymes required for cell metabolism and protein synthesis by replacing natural substances as building blocks in DNA molecules [30] . Some anticancer agents are derived from plants and are called plant alkaloids. They specifically block the ability of a cancer cell to divide and become two cells [31]. Other chemotherapy drugs called antitumor antibiotics act by binding with DNA and preventing RNA (ribonucleic acid) synthesis [32]. The cytotoxicity of chemotherapy drugs affects both cancer cells as well as normal cells. The drugs destroy cells that divide rapidly under normal circumstances such as digestive tract, cells in bone marrow and hair follicles [33],[34]. This effect is not permanent, however, as normal tissues are able to repair themselves and continue to grow. The most common absorbed side effects are mucositis (inflammation of the lining of the digestive tract), alopecia (hair loss), and myelosuppression (decreased production of blood cells, hence also immunosuppression).

There are different plans to treat cancer cases. In some cases chemotherapy is used as the primary treatment, such as in Hodgkin's disease, leukemia, Burkitt's lymphoma, localized diffuse large cell lymphoma, Wilms' tumor, small cell lung cancer, and testicular cancer [21]. Sometimes chemotherapy is combined with other cancer modalities to increase the effectiveness of treatment. For example, chemotherapy is given prior to or after other treatments such as surgery or radiotherapy as an adjuvant treatment to shrink the tumor and make it easier to resect. Adjuvant chemotherapy is also used to reduce the risk of recurrence or prolong survival. When cure is not possible, chemotherapy may be given as palliative therapy for the purpose of helping to make the cancer patient's life as comfortable as possible [35].

2.3.3 Radiotherapy

Radiotherapy remains an important modality among the standards of care for cancer treatment. More than fifty percent (50%) of all cancer patients receive radiotherapy during their course of illness [36]. Radiotherapy uses ionizing radiation and produces free radicals to kill cancer cells and shrink tumors. This is accomplished by damaging the cell structure and DNA in the cell nucleus, hence, reducing cell proliferation [37]. The most common way to deliver radiation to cancer cells is through external beam radiation therapy. However, only limited tumors can be irradiated by high-energy x-rays delivered by a beam to the main tumor [38]. An alternate way using brachytherapy to deliver radiation is through internal radiation therapy, which is done by using a solid source such as seeds, ribbons, or capsules which contain a radiation source and placing them in the body near the tumor [39]. This is also limited to specific type of cancer and is similar to external beam therapy. The other method to provide internal therapy is through systematic therapy when the source of the radiation is in liquid form, allowing the treatment to travel in the blood to tissues, seeking out and killing cancer cells. Additionally, a more specific approach for cancer irradiation is provided by targeted radionuclides which utilize monoclonal antibodies as a vehicle and bind to specific cancer cell antigens [40]. This increases the therapeutic effects of antibodies and minimizes the side effects of nonspecific targeting. Radionuclides emit therapeutic radiation such as alpha, beta particles, and Auger electron which damage the DNA and cell content with different density of energies [41] (Figure 1). Although radiation damages both normal cells and cancer cells, the goal of using targeted radionuclides is to maximize the radiation dose to abnormal cancer cells, while minimizing exposure to normal cells which are adjacent to cancer cells or in the path of the radiation [42]. Normal cells usually can repair themselves at a faster rate and can retain normal function status faster than cancer cells. Cancer cells in general are not as efficient as normal cells in repairing the damage caused by radiation treatment, which results in differential cancer cell killing.

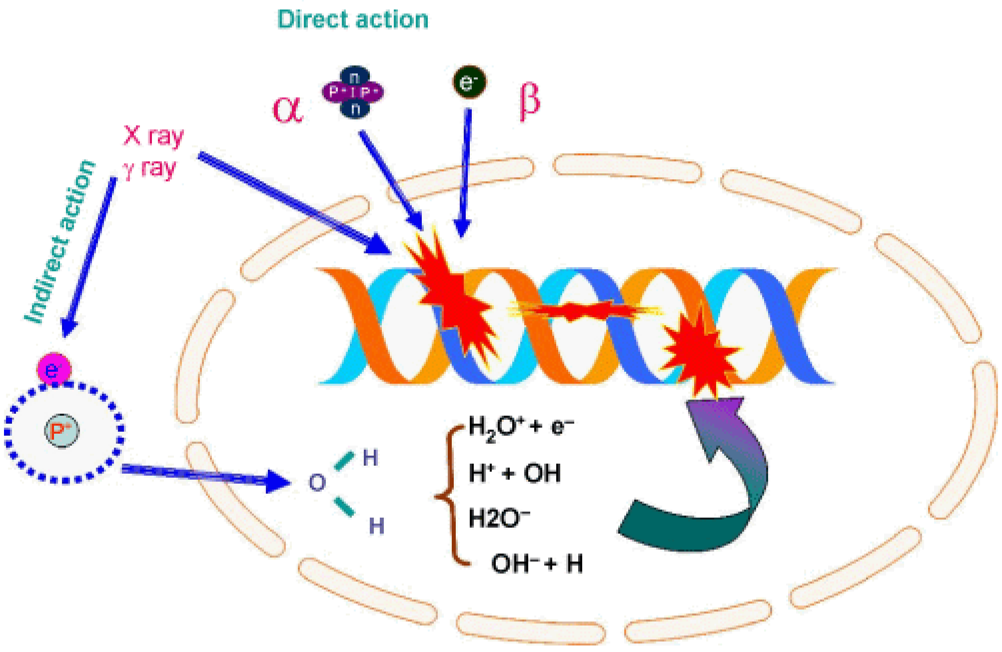

Figure 1. Direct and indirect effect of ionizing radiation on the cell DNA.

2.3.4 Targeted and Biological Therapy

Conventional therapies such as radiation, chemotherapy, and surgery have been used as standard care of cancer treatment for many years [43]. In addition to their potential to kill cancer, however, there are significant side effects on healthy surrounding tissues and organs [44]. Therefore, scientists and researchers have been working to discover methods of treatment that are capable of killing only cancer cells while not affecting healthy tissues at the same time. As scientists and researchers gain a better understanding of the mechanisms and metabolisms of the cells, such as how they replicate, become malignant, their methods of obtaining the nutrients that allow them to survive, and the biological environment of cancer cells, this understanding could lead to specific drugs which would stop the growth of, or even kill, very specific cells such as those that have become cancerous [45]. This process is referred to as “targeted therapies.” It involves the use of very specific methods which interfere with some aspect of cellular life while not harming healthy cells. In cases where biological molecules are used, these therapies are sometimes called “molecular-targeted drugs.”[46].

Biological therapy uses the body’s immune system, either directly or indirectly, to specifically kill cancers cells or minimize the side effects that may be caused by cancer treatments [47]. Biological therapy includes immunotherapy (such as vaccines, cytokines, and some antibodies), gene therapy, hormone therapy, and some targeted therapies [48].

2.3.5 Immunotherapy

Cancer immunotherapy has emerged as a promising approach to therapy [49]. Immunotherapy approaches include the use of monoclonal antibodies (mAbs), cancer vaccines, adoptive cancer therapy, and the immune checkpoint blockade therapy [50]. In the past decade, cancer immunotherapy has become a new pillar of cancer treatment as a result of improvements in our understanding of the biological interaction between cancer cells and the immune system. This has led to the successful discovery of checkpoint inhibitor antibodies (checkpoint blockers against CTLA4, PD-1, and PD-L1) which activate the adaptive cancer-immune response [49]. After FDA approval of two melanoma treatments, Ipilimumab and Vemurafenib, the death rate due to melanoma decreased by 7% per year during the years 2013-2017 [51]. Treatment based on antibodies has advanced the clinical management of multiple diseases, including cancer. The number of therapeutic antibodies approved by the FDA has increased in the last few years [52].

Recent studies have demonstrated enhanced effectiveness of immunotherapy when combined with radiotherapy through the “abscopal” effect [53] Yilmaz et al, 2019; Eldridge et al, 2020). The abscopal effect describes the phenomenon that while using local radiation treatment to one area of metastatic cancer, cancer shrinkage may result in an untreated area as a result of the radiation[54]. While this phenomenon was seen as a rare occurrence in the past, it has become more frequent with the arrival of immunotherapy drugs such as checkpoint inhibitors [55]. The combination of immunotherapy and radiotherapy is one of the new promising strategies to minimize the side effects of nonspecific treatment [56]. This modality of treatment is referred to as radioimmunotherapy (RIT).

2.3.6 Radioimmunotherapy (RIT)

Targeting of radionuclides with antibodies for cancer treatment and imaging has been an active field of research since the discovery of mAbs. It has evolved with advancing technologies in molecular biology, radiobiology, and chemistry, and many important preclinical and clinical studies illustrate the benefits [57]. It is a systemic treatment which aims to deliver cytotoxic radiation specifically to cancer cells while minimizing the radiation exposure to healthy tissue [58]. The system utilizes monoclonal antibodies or its fragments as carriers which bind specific antigens on the surface of cancer cells (Figure 2). Radionuclides emit ionizing radiation, which can be utilized as endoradiotherapy for ionization and free radical formation [59]. This causes significant damage to cellular structures and organelles, including the nucleus and the DNA [60]. Currently, there are some radiolabeled antibodies approved for treatment of non-Hodgkin's lymphoma "90Y-ibritumomab tiuxetan (Zevalin) and 131I-tositumomab (Bexxar)" [61], both of which are anti-CD20 monoclonal antibodies coupled with cytotoxic radioisotopes. Also, 177Lu-DOTATATE was approved for gastroenteropancreatic use in 2018 [62]. While radioimmunotherapy was quite successful for hematological malignancies, treating solid tumors remains a challenge [63] as a result of poor tumor penetration of the antibodies and its suboptimal pharmacokinetics while targeting cancer cell surface antigens [64].

With all the different antibody forms made possible through molecular antibody engineering, it is important to keep in mind that radionuclide selection may vary based on the antibody's biodistribution, tumor retention, and blood clearance properties [65]. Also, the type of chelator and conjugation processes may affect antibody binding and radionuclide selection [66]. Even after radiolabeling, stability and retention of binding must be carefully tested [67]. Therefore, a number of factors including physical and chemical properties contribute to the selection of the most appropriate radionuclide for a radioimmunoconjugate [68]. While there are many radionuclides from which to choose, availability and cost have limited the choices for clinical use.

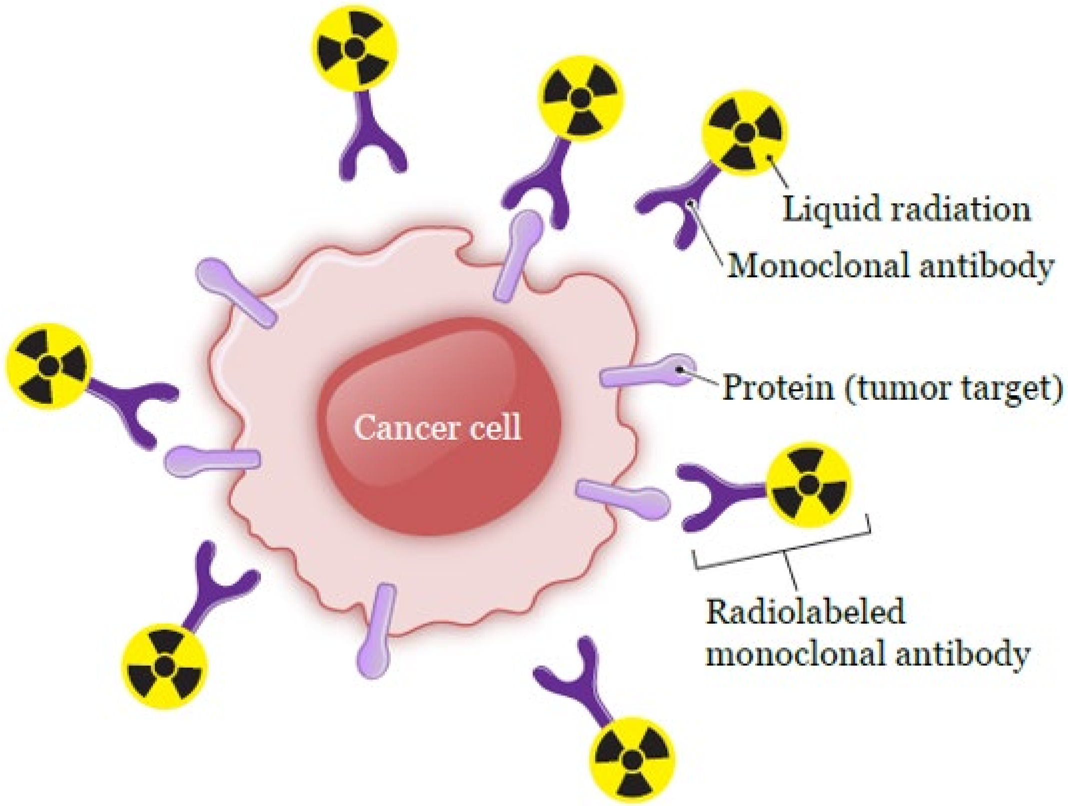

Figure 2. Diagram demonstrating targeted radiolabeled antibody binding to cancer surface antigen.

2.4 Radiolabeling Strategy

The radiolabeling strategy is to attach a particular radionuclide to a mAb, an antibody fragment, or a minibody. It is dependent on the type of radionuclide, (e.g. halogen versus metal), the type of antibody, and the radiochemistry approach used to produce the radio-immuno-conjugate [69].

2.4.1 Radionuclides

There are many radionuclides which have been used successfully for clinical therapy such as iodine-131 (^{131}I), phosphorous-32 [^{32}P], strontium-90 [^{90}Sr], and yttrium-90 [^{90}Y]. Table 1 shows a list of therapeutic radionuclides that have been used either in clinical or research settings. A number of factors are considered when selecting appropriate radionuclides [68]. Such factors include the radionuclide's physical properties, such as the radionuclide half-life, energy and intensity of radiation emitted, and emission characteristics, chemical properties, production methods, and biological behavior such as dissociation from the carrier [68]. In addition, cost, availability, and linkage chemistry play a role in choosing radionuclides for labeling the antibody. Radionuclides can be classified as either diagnostic or therapeutic based on the emission the radionuclide produces. Radionuclides typically used for therapy produce beta particles, alpha particles, Auger electrons, or isomeric transition [70]. Some radionuclides can emit these energy particles together in different ratios [71]. These emissions can irradiate tissue volumes with multicellular, cellular, and subcellular dimensions. Radionuclide action is described by linear energy transfer (LET) [71], which is the amount of energy deposited in tissue per unit path length and is termed liner energy transfer LET. Radionuclides differ in their LET due to type of decay [72] (Figure 4). Therapeutic radionuclides vary in penetrating range and LET, and again depend on the type of decay. Some decay in the form of alpha (α)- or beta-particles (β), or Auger electrons (AEs) and electron magnetic radiation in the form of X-ray or γ ray [71]. Additionally, some radionuclides emit positrons or γ rays. Therefore, they are useful for imaging using positron emission tomography (PET) (e.g.^{15}O, ^{13}N, ^{11}C,^{18}F,^{89}Zr, ^{64}Cu and ^{52}Mn) or single-photon emission computed tomography (SPECT) (e.g.^{123}I and ^{99m}Tc and ^{111}In) [70]. Furthermore, theranostic radionuclides are radionuclides which emit both particulate (e.g. beta or alpha particles) radiation as well as electromagnetic radiation , (e.g. gamma-rays) for therapy and imaging (diagnosis) respectively such as ^{67}Cu, ^{67}Ga, ^{99m}Tc, ^{177}Lu, ^{111}In, ^{123}I, and ^{111}At [70].

Table 1. Main radionuclides which are currently used in Radioimmunotherapy adapted from Reference [73].

Isotope	**Half-life (T1/2)**	**Maximum energy (keV)**	**Maximum range (µm)**	**Emission type**
β−-emitters (LET: 0.2 keV/µm)				
^{90}Y	2.67 d	2280.0	11,300	β−
^{131}I	8.02 d	606.31	2300	β−, ɣ
^{177}Lu	6.65 d	498.3	1800	β−, ɣ
^{67}Cu	61.83 h	577.0	2100	β−, ɣ
^{186}Re	3.72 d	1069.5	4800	β−, ɣ
^{188}Re	17.01 h	2120.4	10,400	β−, ɣ
Auger emitters (LET: 4–26 keV/µm)				
^{111}In	2.80 d	26	17	Auger, ɣ
^{67}Ga	3.26 d	9.6	3	Auger, β−, ɣ
^{195m}Pt	4.02 d	64	76	Auger
^{125}I	59.41 d	31.7	20	Auger, ɣ
α-emitters (LET: 50–230 keV/µm)				
^{213}Bi	45.59 min	8400	90	α, β−, ɣ
^{212}Bi	60.54 min	7800	100	α, β−, ɣ
^{211}At	7.21 h	7500	80	α, EC
^{212}Pba	10.64 h	7800	100	α, β−, ɣ
^{225}Ac	9.92 d	8400	90	α, β−, ɣ
^{227}Th	18.7 d	7400	70	α, β−, ɣ

2.4.1.1 Alpha-Emitting Radionuclides (α-decay)

Some unstable atomic nuclei dissipate excess energy by emitting an alpha particle (helium nucleus) because alpha particles have two positive charges and a mass of four units. The emission from nuclei produces daughter nuclei having a positive nuclear charge or atomic number two units less than their parents and a mass of four units less (Scheme 1).

Alpha-emitting radionuclides are a promising type of radiotherapeutics which show great potential in the treatment of a broad range of malignancies [74]. Alpha particles have high kinetic energy (5-8 MeV) and their range in tissue is about 40-80 μm. An Alpha particle is an helium atom and its nucleus consists of two protons and two neutrons [75]. Alpha particles have a high linear energy transfer (LET) value of 50-230 keV/μm [76] (Figure 4). As a consequence of their high LET, they have greater relative biological effectiveness (RBE) and require less radiation per cell kill than beta particles or x-rays [77]. The path length of alpha-particles is short, so the energy deposited is limited to a few cells. Thus, they are capable of destroying tumors while causing very limited damage to the surrounding healthy tissue [78]. These properties seem to be ideal for treating small cells, such as in micro-metastatic cancer [74]. Alpha-emitting radionuclides offer the exciting prospect of matching the cell-specific nature of molecular targeting with radiation of a similar range of action [74]. However, for alpha therapy to be effective, the radionuclide decay needs to take place at close proximity to the cell or inside the cell. This is dictated by the quality of the site specific targeting molecule, such mAb [79].

$${}^{A}_{Z}\text{Parent} \longrightarrow {}^{A-4}_{Z-2}\text{Daughter} + {}^{4}_{2}\text{He}$$

Scheme 1 Alpha decay

2.4.1.2 Beta-Emitting Radionuclides (Negative Beta decay (β^- -decay))

Negative beta particles are emitted when the nucleus of radioisotopes have an excess number of neutrons. The neutron will convert to proton and emit beta particles which are an energetic electron (of relatively small mass) and an antineutrino which has no rest mass nor electric charge and does not interact readily with matter (Scheme 2). Therefore, the atomic number of this nucleus will increase by one and the mass number will remain the same. These are negative beta particles or negatively charged electrons emitted from the nucleus and their energy in tissue varies from zero up to maximum [60].

About one-third of the maximum energy is equal to the average energy of $\beta-$ particles energy [68]. $\beta-$ particles energy ranges from 0.05 to 2.3 MeV, and they have low LET of about 0.2 keV/µm with a long penetrating range in tissue (1 mm to several mm) [80] (Figure 4). This causes limited ionization and DNA damage involving single-or double-strand DNA breaks, base chemical modifications, and protein crosslinks [80]. Consequently, disregarding other parameters, such as tumor penetration profiles of radionuclide carriers, higher radionuclide concentrations of beta emitters than alpha emitters are required for comparable cell kill.

$\beta-$ particles emitters such as ^{177}Lu, ^{90}Y and ^{131}I have been used in cancer treatment [81]. However, the long beta particles' path that crosses multiple individual cells might cause a "crossfire" effect by energy disposition in normal tissue [71]. Cell survival studies show that cells are more sensitive to radiation when they are arrested in the G2 phase and are in a good oxygenated state (35). The presence of oxygen upon beta particle irradiation generates free radical species that are particularly harmful to the nuclear DNA. Both the rate of beta particle disintegration (half-life) and amount of radioactivity at the target site influence the killing efficacy by competing against the enzymatic repair of the irradiated DNA strands.

$$n \rightarrow p + e^{-} + v^{-}e$$

$${}^{A}_{Z}\text{Parent} \longrightarrow {}^{A}_{Z+1}\text{Daughter} + e^{-} + v^{-}e$$

Scheme 2 Negative beta decay

2.4.1.3 Beta-Emitting Radionuclides (β^{+}-decay) (Positron emission)

When some of the unstable radioisotopes nucleus have an excess number of protons, these protons will convert into neutrons in order to stabilize the nucleus [82] (Figure 3). A proton in the parent nucleus decays into a neutron that remains in the daughter nucleus, and the nucleus emits a neutrino and a positron. The neutrino has no electric charge nor rest mass, while the positron is a positive particle like an ordinary electron in mass but of positive charge. Therefore, positive beta decay produces a daughter nucleus, and in each decaying nucleus emits a positron and a neutrino, reducing its atomic number by one while the mass number stays the same. The positron does not exist for a long period of time in the presence of matter. It will travel a short distance before colliding with an electron of a nearby atom, with which it undergoes annihilation. This annihilation will emit electromagnetic energy in the form of two 511-keV gamma rays that are emitted in almost opposite directions [82] (Figure 3). These are useful photons for imaging because they easily escape from the human body and can be recorded by external detectors. When two opposite gamma-rays detected following the disintegration of positronium, this is called a coincidence line. These coincidence lines offer a unique detection scheme for forming tomographic images with PET. Many radioisotopes decay by positron, such as underging this decay and thereby emit positrons including carbon-11, nitrogen-13, oxygen-15, fluorine-18, copper-64, gallium-68, bromine-78, rubidium-82, yttrium-86, zirconium-89, yttrium-90,[3] sodium-22, aluminium-26, potassium-40, strontium-83.

$$p \rightarrow n + \beta^{+}/e + ve$$

$$^{A}_{Z}\text{Parent} \longrightarrow {}^{A}_{Z-1}\text{Daughter} + e + ve$$

Scheme 3 Positive beta decay

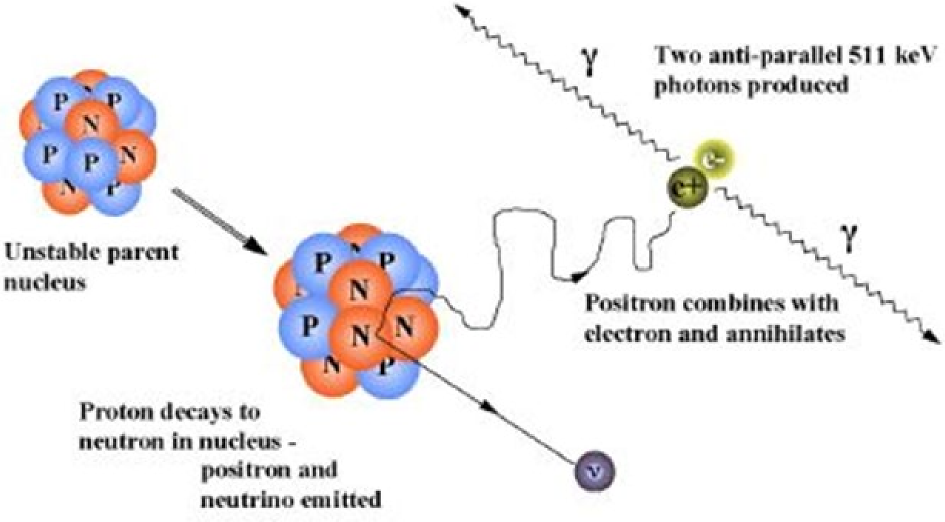

Figure 3. Schematic illustration of an annihilation reaction in tissues. A positron emitted from the nucleus and then annihilates with an electron to produce two gamma rays in opposite direction. Adapted from ref [83].

2.4.1.4 Electron Capture (Inverse Beta Decay)

In this process, a proton-rich unstable nucleus similar to positive beta decay. However, it reduces its nuclear charge to one unit by absorbing an atomic electron to convert the proton to a neutron and a neutrino. The proton captures an electron from the K or L shell. This process reduces the atomic number by one and emits gamma radiation or an x-ray and auger electrons. When the electron is absorbed from the electron orbit, the outer orbital electron will fill the vacancy. This will set off a cascade of electron transitions with their associated characteristic x-rays emission. The transition of losing the outer orbital electron, will result in releasing of energy. When this energy transferred to another electron, the electron will be ejected from the atom and this electron is called an Auger electron [84].

$$\mathbf{p + e \dashrightarrow n + \nu.}$$

$$^{A}_{Z}X + e^{-} \rightarrow \quad {}^{A}_{Z-1}Y \quad + \quad \nu_e$$

Scheme 4 Electron capture decay

2.4.1.5 Auger-Emitting Radionuclides

Auger electrons are low energy atomic orbital electrons emitted following electron capture (EC) decay [79]. They have short ranges of 1-2µm and a high LET. However, they need to be internalized into the cell nucleus to be most effective [79]. If internalized, their high LET means they can be profoundly cytotoxic. Recent work to improve Auger therapy has led to the development of fusion proteins incorporating a nuclear localization sequence (NLS) [70]. The LET of Auger electrons range between 4 and 26 keV/µm (figure 4). This high energy produces clustered damage in DNA and the cell membrane [84]. Also, many of AE-emitting radionuclides emit a small number of internal conversion IC electrons which have high energies and transfer in several millimeters [84].There are many Auger-emitting radionuclides which have been used in nuclear medicine (e.g. ^{99m}Tc, ^{123}I, ^{111}In) [74].

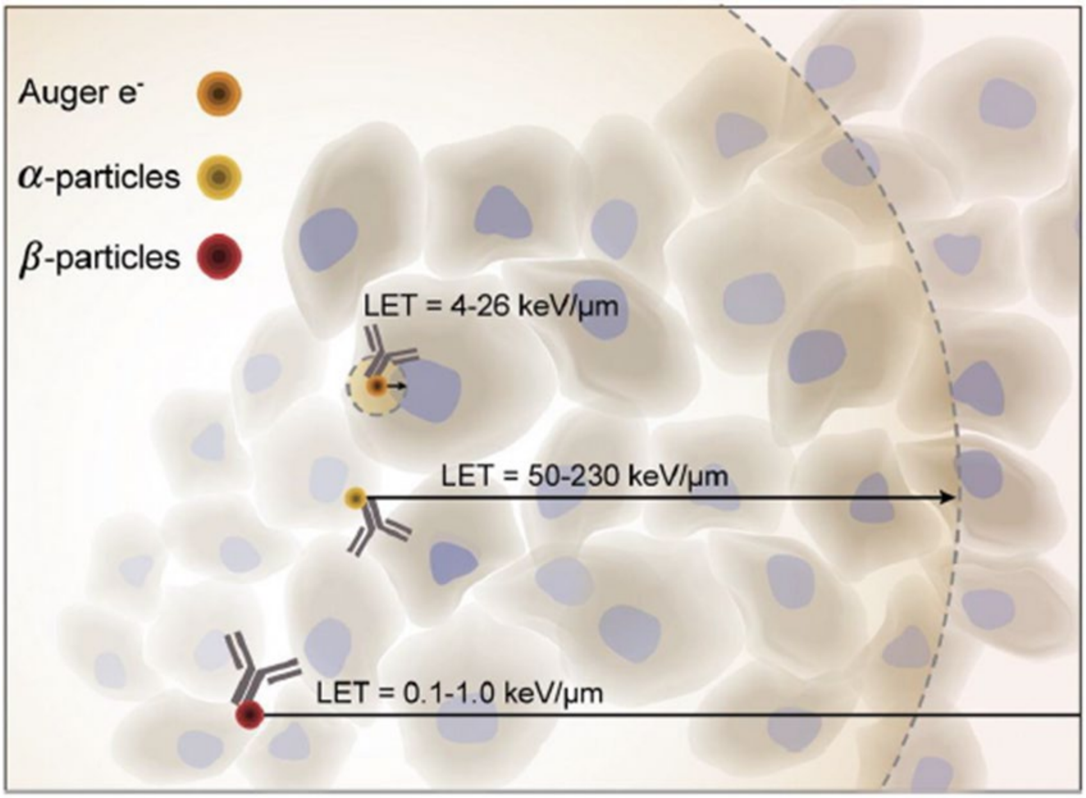

Figure 4. Illustration of the track of α-particles, β-particles or Auger electrons emitted by radiolabeled monoclonal antibodies targeted to cancer cells. The short track length of α-particles (28–100 μm) and Auger electrons (<0.5 μm) results in high linear energy transfer (LET) values of 50–230 keV/μm and 4 to 26 keV/μm, respectively. β-particles have a track length of 2–10 mm resulting in LET of 0.1–1.0 keV/μm. The high LET of α- particles (50–100 μm) and Auger electrons make these forms of radiation more powerful for killing cancer cells than β-particles.Adapted from ref [74].

2.4.1.6 Gamma (γ) Decay

This is an electromagnetic radiation usually followed alpha and beta decays. When the radioactive nucleus emits alpha or beta particles, the new daughter nucleus left is in an excited state and will release energy to allow the proton or neutron to relax back down to ground state. During this transition from a high to a low energy state gamma photon is emitted. Gamma rays are photons, or packets of high electromagnetic energy of extremely short wavelength. The energy of gamma rays ranges from a few keV to ~8 MeV, corresponding to the typical energy levels in nuclei with reasonably long lifetimes. This type of decay does not change the structure or composition of the atom. It only changes the energy because it does not carry any charge or associated mass. Gamma decay includes two other electromagnetic processes, internal conversion and internal pair production. In internal conversation, it always accompanies the predominant process of gamma emission to some extent. This takes place when the excess energy in a nucleus is directly transferred to one of its own orbiting electrons and, as a result, the electron is ejected from the atom. Internal pair production happens when the excess energy is directly converted within the electromagnetic field of a nucleus into an electron and a positron (positively charged electron) that are emitted together. Gamma radiation is emitted by many natural radioisotopes and is also produced artificially in fission in nuclear reactors, high energy physics experiments, nuclear explosions, and accidents. Although gamma rays are harmful due to the fact that they are generally very high energy and, therefore, penetrate matter very easily, it is useful radiation for medical and other purposes. Gamma rays have been used in medicine (radiotherapy and diagnosis), industry (sterilization and disinfection) and the nuclear industry. Gamma rays produce photons indirectly through gamma-ray photon-electron interactions as the gamma radiation travels through a transparent medium. These photons are useful for imaging used by both single photon emission computed tomography (SPECT) and Positron Emission Tomography (PET).

2.5 Antibodies

Due to the affinity, specificity, and selectivity, antibodies and antibody fragments, including minibodies, make attractive vehicles for delivery of radionuclides to tumors for imaging and therapy [85]. Monoclonal antibodies are macromolecules and, therefore, have longer biological half-life because of their size. This enables them to match and label long radioactive decay half-life radionuclides [86].

Monoclonal antibodies (mAbs) are about (150 kDa) (Figure 1), while antibodies fragments <150 kDa (e.g VH or VL domains (15 kDa), scFv (30 kDa), Fab (50 kDa) and Fab'2 (110 kDa (as shown in Figure 5) [85]. Large size antibodies have a longer circulation time than smaller fragments [85]. Monoclonal antibodies are complex molecules comprised of two identical light chains and two identical heavy chains held together by disulfide bonds. Consequently, they form a Y-shaped molecule containing two identical antigen-binding arms (Fabs) and a glycosylated stem region (Fc) separated by a flexible hinge region (Figure 5). The Fc region is responsible for the recruitment of cytotoxic effector mechanisms, including the activation of a complement cascade and interactions with Fc-receptors on immune cells [85]. The Fc also furnishes mAbs with an unusually long serum half-life of several days or weeks through interactions with neonatal Fc receptors [86]. Atypical antibodies consist of about 80% of lysin residuse [87].The advanced technology in antibody engineering has led to producing humanized mAb and its fragments and has improved the conjugation, tumor penetration, and targeting affinity [87]. The use of mAbs is well established and currently more than 150 of them are in clinical development [52]. In this project monoclonal SAS1B antibodies were used for radiolabeling and near-infrared dye labeling.

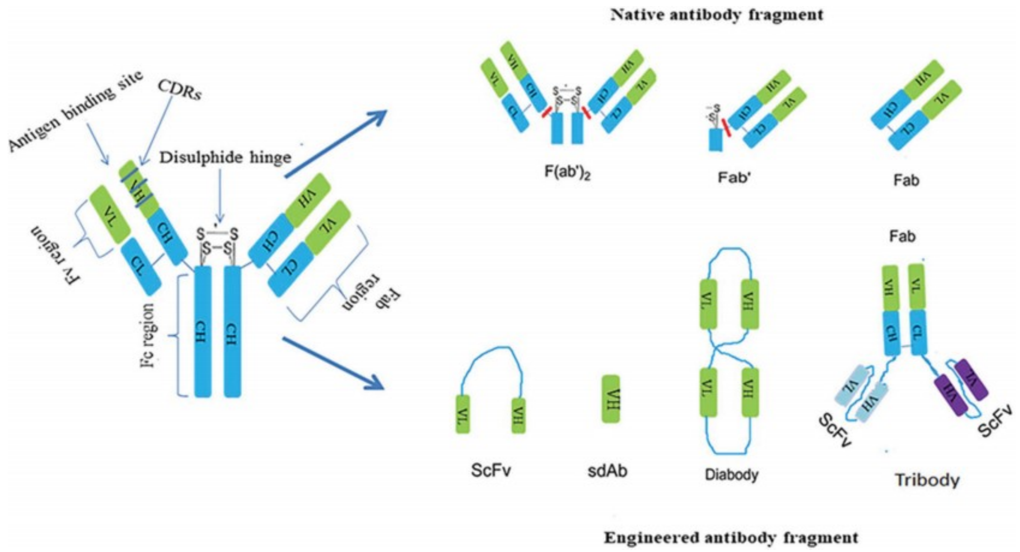

Figure 5. Monoclonal antibody and antibody fragments. Left: Y-shaped structure of antibody. The Fc domain consists of the constant part of the two heavy chains, while the Fab domain consists of the variable part of the heavy chain and the light chain. Right: Native and engineered antibody fragments. Adapted from reference [88].

2.6 Radiochemistry of Radiolabeled Antibodies

Radiolabeling of antibodies can be done either directly or indirectly. While halogen-based radionuclides can be used to directly label antibodies, metal-based radionuclides require a linker (chelator) molecule to conjugate to the antibody [89]. For example, iodine radionuclides are used to either directly label antibodies by electrophilic substitution or indirectly via a conjugation group (Figure 6-A). Most other radionuclides label antibodies indirectly via prostatic group (Figure 6-B) or via complexation by a chelator (Figure 6-C).

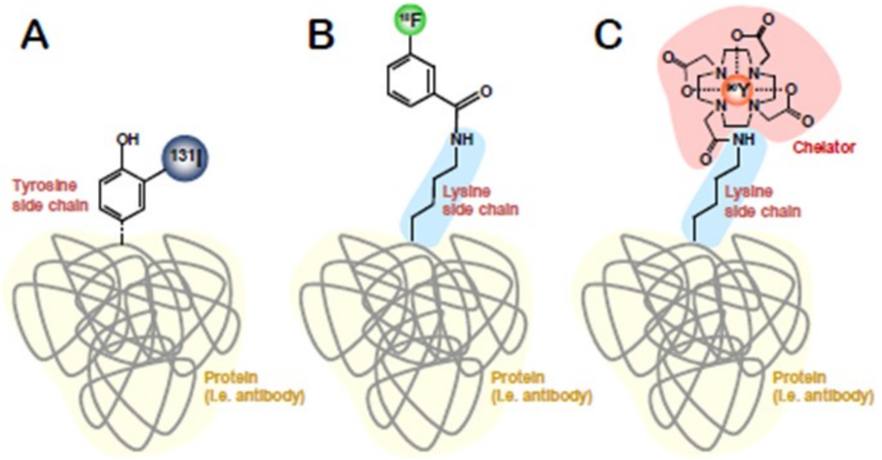

Figure 6. Radiolabeling Strategies A) Direct labeling. (B and C) Indirect labeling. Adapted from Ref [90].

Metal radionuclides, such as zirconium-89, Indium-111, and lutetium-177, require a chelator molecule to label monoclonal antibodies indirectly [89]. There are a wide range of bifunctional chelators. BFCs have been developed for conjugation of targeting constructs with several radionuclides. It is important that BFC produce a large, expedient, and stable yield in radiolabeling [91]. The selection of which radiochemical method to use to prepare radioimmunoconjugates is based on the physiochemical properties of the radionuclide [89]. For instance, the short half-life of some radionuclides does not allow for lengthy reaction conditions, and additional purification steps are unfavorable. Due to the diverse properties and coordination chemistry of radionuclides, it is difficult to design a chelating agent which can bind to all radionuclides. Moreover, selection of BFCs is largely determined by chemical properties, such as oxidation state and coordination chemistry [91], and the resulting radiopharmaceutical must have high solution stability. Therefore, BFCs must form a metal chelate with high thermodynamic stability and kinetic inertness *in vitro* and *in vivo* to avoid both accumulation of radioactivity in normal tissue and interaction with ions available *in vivo* [91]. Several macrocyclic agents have been developed for stability of frequently based radionuclide complexation. There are different approaches to conjugating chelator to antibodies. The functional group of the chelator could be an aromatic isocyanate or an activated ester, which will react with nucleophilic sites (-NH2,-SH, or –OH) of antibody [92]. For example, p-SCN-Bn- DOTA c(S-2-(4-Isothiocyanatobenzyl)-1,4,7,10-tetraazacyclododecane tetra acetic acid), a chelator with isothiocyanate, reacts with the N-terminal amino group of the antibody, additional lysine resides, and even arginine residues [93]. On the other hand, when it reacts with metal ions of radionuclide, DOTA makes a complex structure by coordinating the nitrogen atom of the cyclen ring and carboxy groups of the acetate arms [93]. It is useful to know the sites of crosslinking, as well as the amino acid residues in monoclonal antibodies which bind to the functional group in chelator when choosing the appropriate chelator with specific functional group. This can help avoid undesirable binding of chelator with the antibody, such as binding to Fab regions which may lead to nonspecific binding inside the body [91]. It is necessary to ensure that the conjugation of a chelator to the antibody does not lower the antibody-receptor binding. When the active sequence that confers binding affinity is known, the conjugation can be directed. Moreover, conjugation efficiency depends on optimizing ratio of chelator to monoclonal antibody, pH, time, and the temperature of the reaction [91].

CHAPTER 3: MOLECULAR IMAGING

3.1 Molecular Imaging

Molecular imaging is an attractive approach that enables noninvasive visualization, characterization, and quantification of biological processes (events) taking place at the cellular and subcellular levels in humans and other living systems. Molecular imaging contributes in clinical diagnosis, staging of the disease, treatment, and surgery plan [94]. Molecular imaging can also provide quantitative information which plays an important role in monitoring cancer status over time or in treatment [95]. There are several techniques that are well established imaging modalities. These include techniques based on radiation, optical, nuclear magnetic resonance, and ultrasound properties (Table 2). MRI and computed tomography (CT) depend solely on energy-tissue interactions, whereas others such as PET or optical imaging require the administration of radionuclides or optical probes [95]. Positron emission tomography (PET) and single-photon emission computed tomography (SPECT) are of great interest from the view of high sensitivity as nuclear medical imaging, distribution, and kinetics of a radiolabeled molecular probe in which a radioactive molecular probe is administered into the body [96]. The other attractive methodology is optical molecular imaging which depends on light photons at different wavelengths from visible and infrared ranges resulting from fluorescent and bioluminescent events. For instance, using fluorescent probes that can be detected by using a fluorescent imaging instrument to study distribution and kinetics. This technique does not involve exposure to ionizing irradiation and provides real-time imaging with high spatial resolution inexpensively [97],[98]. The most common imaging techniques and their important characteristics and applications are listed in table 2. Each of these imaging tools brings its own advantages and disadvantages. In order to obtain optimal performance, in most cases the suggestion is to use more than one modality, either in series or combined in one hybrid modalities, *e.g.*, PET/CT or

PET/MR [99],[100]. Most image modalities depend on identifying the imaging target and selecting an appropriate imaging contrast agent or ligand. Based on specific properties, imaging targets can range from cell surface markers or genes and their related products to a particular cellular or pathological process [96]. Usually the agent is in the form of a small molecule, protein, or antibody that can bind to or enter the target environment upon injection into the subject body [101]. In recent years, multimodality probes have been increasingly common for improvements in efficiency.

Table 2.The most common imaging modalities.

Modality	**Spatial resolution**	**Advantages**	**Disadvantages**	**Sensitivity**	**Depth of penetration**	**Type of molecular probe**	**Probe quantity**
CT	50-200um	High spatial resolution penetration depth, fast and cross-sectional image	Low contrast, radiation risk	10^{-8}	Limitless	May be possible	Not used
PET	1-2 mm	High sensitivity; excellent penetration depth; whole-body imaging	High cost of cyclotron needed; radiation risk	10^{-11}-10^{-12}	Limitless	Radiolabeled , directly or indirectly	Nano grams
SPECT	1-2 mm	High sensitivity; no tissue penetration limit; no need for cyclotron	Low spatial resolution; radiation risk; hard to quantify	10^{-9}-10^{-8}	Limitless	Radiolabeled , directly or indirectly	Nano grams
MRI	25-100um	High spatial resolution no tissue penetrating limit No radiation	Relatively low sensitivity and low contrast: high cost :long scanning time	10^{-9}-10^{-8}	Limitless	10^{-2}-10^{-5}	Micrograms-Milligrams
Optical fluorescence imaging	2 – 3 mm^{d}	High sensitivity ; no radiation; inexpensive activalable	Low spatial resolution attenuation by overlying tissues; poor penetration depth	10^{-9}-10^{-12}	<1cm^{f}	Activatable, directly or indirectly	Microgram-Milligram
Optical bioluminescence imaging	3-5mm^{d}	High sensitivity; no radiation; inexpensive and simple equipment operation; non-damaging imaging	Low spatial resolution attenuation by overlying tissues; poor penetration depth	10^{-15}-10^{-17}	1-2cm	Activalable indirectly	Microgram-Milligram
Ultrasound	50-500um	No radiation; excellent sensitivity with microbubbles; high temporal resolution; inexpensive	Poor penetration depth; High spatial resolution; low contrast and strong boundary effect	Excellent when microbubbles used	Millimeters-Centimeters	Limited Activatable, directly	Microgram-Milligram

3.1.2 Positron Emission Tomography (PET)

Positron Emission Tomography (PET) is widely used as a molecular imaging approach for research and clinical needs using different radionuclides Table 3. PET is a minimally invasive imaging procedure with a wideranges of clinical and research applications. PET allows for the three-dimensional mapping of administered positron-emitting radiopharmaceuticals such as ^{18}F-fluorodeoxyglucose (for imaging glucose metabolism). Also, PET enables the study of biologic function in both health and disease. In addition molecular imaging with PET allow the visualization of various molecular pathways including metabolism, prolife-elation, oxygen delivery and consumption, and receptor or gene expression, all of which may be important in the response to ionizing radiation[102]. Furthermore, PET can be used to evaluate novel radiolabeled PET imaging agents, effectiveness of new therapies, and biodistribution of novel pharmaceuticals in suitable animal models.

PET is based on using the advantage of the unique properties of radioactive isotopes that decay via positron emission. The nucleus of these radioisotopes has an excess of protons and, in order to reach stability, protons transform into a neutron, a positron, and a neutrino. The newly formed short-lived positron is ejected from the nucleus and interacts with an electron from the surrounding environment after traveling a distance. This is called positron annihilation, resulting in the emission of two 511 keV gamma rays traveling in opposite directions (Figure 7 and 8). Image acquisition is then based on simultaneous detection (coincidence detection) of these two gamma rays Figure 9. By acquiring a large number of such events, tomographic reconstruction methods can be used to reconstruct two dimensional images of the tracer distribution.

PET scans are now routinely combined with computed tomography (PET/CT) or magnetic resonance imaging (PET/MRI). The functional metabolic imaging of PET is fused with the anatomical structure imaging of CT or MRI, which can obtain information such as function and metabolism, and can also have high spatial resolution and accuracy. Moreover, a variety of PET radiotracers have been introduced.

Table 3.Most comomly used PET radionuclides.

Radinuclide	Imaging modality	Half-life
^{15}O	PET	2.05 min
^{13}N	PET	9.96 min
^{11}C	PET	20.4 min
^{18}F	PET	109.7 min
^{68}Ga	PET	67.6 min
^{64}Cu	PET	12.7 h
^{89}Zr	PET	78.4 h
^{76}Br	PET	13.1 h
^{124}I	PET	4.18 days

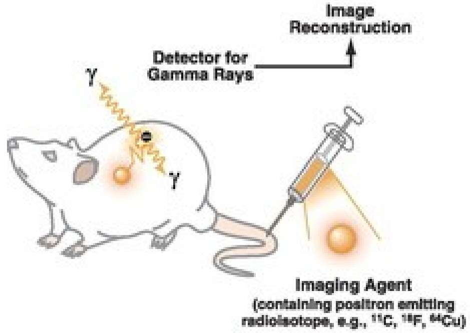

Figure 7. Small animal positron emission tomography (PET). A: schematic illustrating the basic principles of PET. First, a targeted imaging agent (e.g., small molecule, peptide, engineered protein, aptamer, nanoparticle) containing a positron emitting radioisotope is administered to the subject.

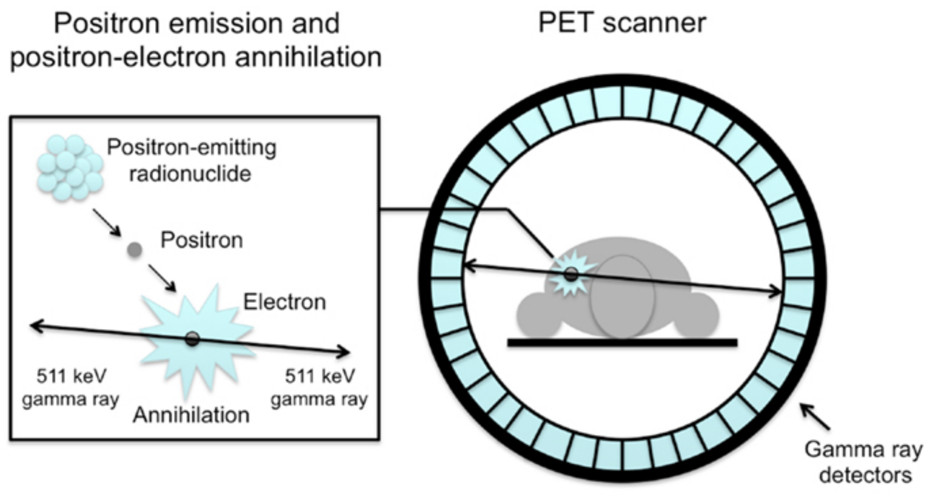

Figure 8. Illustration of an annihilation reaction in tissues and the subsequent coincidence detection in PET detector. Adapted from reference [103].

3.1.2.1 Coincidence Detection

PET records only true coincidence events that originate as a result of positron annihilation along the line between the two parallel opposite detectors (Figure 9-A). These events carry information regarding the spatial location of the positron source. The detector pair should ideally produce signals simultaneously. In cases of true coincidences, but due to limitations of scintillation detector as well as associated electronics, coincidence events are accepted within a finite interval which is of the order of 4 to12 ns. Therefore, two unrelated photons may be detected and get registered as coincidence events (Figure 9-B). These events are called random or accidental events and they provide useful information regarding spatial location of activity distribution which needs to be corrected. These accidental events cause noise and increased background in the final images. In addition, sometimes both of the annihilated photons are diverted from their original direction as a result of Compton interaction and reach the detector to misposition the coincidence event as shown (Figure 9-C).

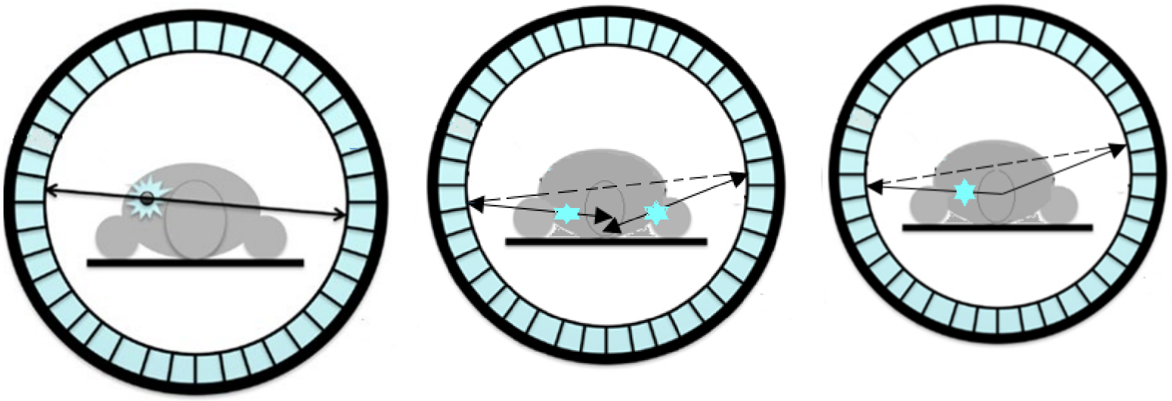

A-True coincidence events B-Random or accidental events C-Scattered coincidence events

Figure 9. Types of coincidence events. True coincidence detection occurs when the two gamma rays are detected from one annihilation event in the time window. Random coincidence occurs when both photons detect in the time window and are from deferent annihilation events. scattered coincidence occur when at least one of the gamma photons under goes Compton scattering, and both photons still detected in the time window.

3.1.2.2 Production and Applications of PET Radionuclides

Positron sources are produced artificially because they are not stable in nature. They are produced by bombarding stable isotopes with positively charged particles. This requires using a cyclotron to generate short-lived radionuclides such as ^{18}F (t1/2 = 109.8 min), ^{64}Cu (t1/2 = 12.7 h), and ^{76}Br (t1/2 = 16.2 h), or ultra-short-lived radionuclides such as ^{11}C (t1/2 = 20.3 min), ^{13}N (t1/2 = 10 min), and ^{15}O (t1/2 = 2.04 min) (143). There many radionuclides that have been used for preclinical and clinical. Table 4 lists some of the most used PET radioisotopes.

Table 4. Example of some radionuclides production.

Radioisotope	Half-life (h)	Decay mode (%)	Application
F-18	1.8	EC β^+(97), (3)	18F-FDG
I-124	100.3	β^+(23), EC(77)	Imaging (PET) Thyroid cancer, Cardiovascular imaging [124I]-MIBG
Cu-64	12.7	β^+(19), β^-(40), EC(41)	Imaging (PET); Therapy Prostate cancer [^{64}Cu]-NODAGA-PSMA)
Ga-68	1.1	β^+(89), EC(11)	Imaging (PET) Neuroendocrine tumors [^{68}Ga]-DOTATOC, [^{68}Ga]-DOTATATE
Zr-89	78.4	β^+(23),EC(77)	Imaging (PET) Variety of cancer-related targets (HER2, ER, PSMA

Usually PET scans are combined with computed tomography (PET/CT) or magnetic resonance imaging (PET/MRI). This provides functional metabolic imaging of PET and anatomical structure imaging of CT or MRI, so in addition to the information of the function and metabolism, it will have high spatial resolution and accuracy.

Positron Emission Tomography (PET) has emerged as one of the greatest tools used for clinical applications (Table 5). FDG PET being better than MRI and CT in detecting lymph node metastasis from SSC [104]. Providing metabolic functional imaging and pathologic processes by using PET images opened newer options for incorporation of this information into patient management protocols. Table 5 shows some useful clinical applications using PET scan.

Table 5. Commonly used PET tracers for clinical molecular imaging of diseases. Adapted from reference [105].

Medical Imaging	**Molecular Target**	**Radiotracer(s)**	**Clinical Applications**
Oncological Imaging	Protein synthesis	^{11}C Methionone,	Protein synthesis in tumors
	Glucose transporter	^{11}C-DG, ^{18}F-FDG	Glucose metabolism in tumors
	Choline transporter	^{11}C-choline	Tumor phospholipid synthesis
	thymidine uptake in DNA/RNA synthesis	^{18}F-FLT, ^{18}F-FMAU; ^{18}F-FU	Tumor cell proliferation
	$\alpha_V\beta_3$ integrin	^{18}F-galacto-RGD	Tumor angiogenesis
	HSV1-tk	^{18}F-FHBG	Suicidal gene therapy
	Hypoxia	^{18}F-FMISO; ^{64}Cu-, ^{60}Cu-ATSM	Tumor hypoxia
	Somatostatin receptor	^{64}Cu-TETA-octreotide	Neuroendocrine tumors
	Estrogen receptor	^{18}F-FES	Breast Cancer
	Androgen receptor	^{18}F-FDHT	Prostate Cancer
Cardiovascular Imaging	Cell metabolism	^{11}C Acetate	Cardiac metabolism
	Fatty acid metabolism	^{11}C Palmitate	Ischemia
	Adrenergic neurotransmission	^{11}C Metahydroxy-ephedrine	Heart failure
	Cardiac Sympathetic Neurons	^{18}F Norephinephrine	Cardiac sympathetic innervation
Neurological Imaging	Dopamine post synaptic receptors	^{11}C Raclopride	Schizophrenia, Addiction
	β-amyloid	^{11}C-PIB	Alzheimer's disease
	NK-1 Receptor	^{18}F SPARQ; ^{11}C-R116301	Depression, Anxiety
	Dopamine transporter	^{18}F FECNT	Schizophrenia, Addiction
	Dopamine metabolism	^{18}F DOPA	Schizophrenia, Addiction

3.2.2 Single photon emission computed tomography SPECT

Single photon emission computed tomography (SPECT) is a nuclear medicine imaging technique using gamma rays. SPECT provides a 3D image to visualize and measure biological processes within living systems. The basic principle for SPECT is based on using the advantage of nuclides such as ^{99m}Tc (t1/2 = 6 h), ^{123}I (t1/2 = 13.3 h), and ^{111}In (t1/2 = 2.8 days), which decay via the emission of single gamma rays with differing energies. When the radionuclide emit gamma-ray inside the body, it can be detected using a single or a set of collimated radiation detectors[106].Two or three gamma cameras rotate and detect gamma rays produced by radionuclides from different angles. The detectors used in current SPECT systems mostly depend on a single or multiple NaI (TI) scintillation detectors [106]. When gamma rays produce light photons (415nm) which enter the scintillator and ionize the iodine atoms, these photons are converted to an electrical signal which is then recorded and used to reconstruct multiple two-dimensional images and generate cross-sectional images [107]. In SPECT, projection data are acquired from different views around the animal or patient (Figure 10 &11). Table shows the most common used radionuclides and it applications.

Table 6. Most commonoly used SPECT radionuclides.

Radioisotope	Half-life (h)	Decay mode (%)	Application
Tc-99m	6.0	IT(100), γ	Used for diagnostic imaging many types of cancer
Ga-67	78.3	EC(100), γ	Imaging (SPECT)
I-123	13.2	EC(100), γ	Imaging (SPECT) Thyroid cancer
In-111	67.2	EC(100), Auger, γ	Imaging (SPECT); Therapy Widely used in clinical practice for diagnosis
Lu-177	159.5	β−(100), γ	Imaging (SPECT); Therapy ^{177}Lu DOTATATE
Cu-67	62	β−(100), γ	SPECT imaging and therapy

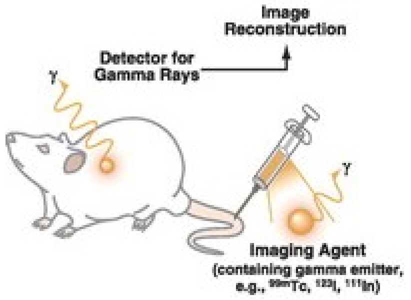

Figure 10. Small animal single photon emission computed tomography (SPECT). A: diagram illustrating the principles of SPECT, i.e., a targeted SPECT imaging agent (containing a gamma emitting radioisotope) is administered to the subject and the gamma rays are detected via a gamma camera (rotated around the subject).

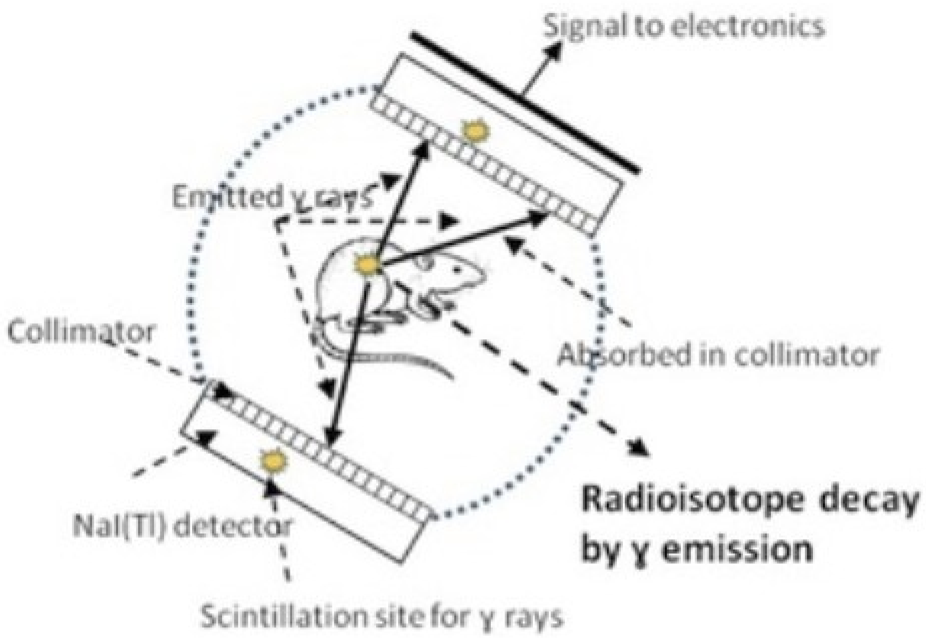

Figure 11. Illustration of the basic principle of SPECT imaging.

3.3 Optical Imaging

Optical imaging techniques offer simplistic while highly sensitive modalities for molecular imaging research. Non-invasive images help with identification and localization of tumor lesions and characterization of processes involved in tumor proliferation and invasion, concurring to the description of tumor features, staging, treatment evaluation, and as image-guided-surgery[108].

Images are generated by using photons of light in the wavelength range from ultraviolet to near infrared. The contrast of optical images can be derived through using exogenous agents such as dyes or probes, or by using endogenous molecules which can provide a signal such as NADH, hemoglobin, collagens, and reporter genes [109]. The strategies of optical imaging are based on the use of injectable fluorescent or luminescent probes that provide the possibility to study tumor features. Currently, most of these probes are used only in animal models, but the possibility of applying some of in clinics also is under evaluation [108].

3.3.1 Fluorescence molecular imaging (FMI)

Fluorescence molecular imaging (FMI) is emerging as a technology with substantial potentials that enable *in vivo* imaging of molecular and cellular processes with high sensitivity[110]. FMI has gained great popularity over the past decade, mainly because of its safe and straightforward use. The application of fluorescence molecular imaging would also help bioengineering scientists investigate disease processes, evaluate therapy response, and develop new drugs. FMI is based on using an engineered imaging of fluorescence agents to target specific disease biomarkers. When fluorescence agents are excited with a light source, fluorescence is emitted as photons during the return to a ground state of electrons excited by photo-stimulation. These photons can be revealed by a high sensitivity camera (CCD mainly) through appropriate band-pass filters to block photons at the excitation wavelength and allow the recording of photographs of emission (fluorescence) photons exiting the tissue surface. Depending on the particular light-sensitive technology employed, there are different operational specifications and spectral regions spanning 400–1,700 nm which can be implemented. For example, a charge-coupled device (CCD), indium gallium arsenide (InGaAs), or a complementary metal-oxide–semiconductor (CMOS). There are also many different fluorescent agents that target biochemical and molecular features of diseases that are being approved for experimental clinical use. For instance, a folate receptor-targeting fluorescence agent has been used to improve detection of ovarian cancer in patients [111]. Also, fluorescently labeled cetuximab has been employed to improve precision in oral cancer surgery [112]. Fluorescence molecular imaging can obtain high sensitivity detection with low instrumentation expense compared with other molecular imaging approaches.

Moreover, a protease-activated fluorescent agent was also considered in humans for detecting soft tissue sarcoma [113]. Additionally, using a targeted heptapeptide for detection of colonic dysplasia and detection of Crohn's disease using a fluorescent labelled antibody targeting tumor necrosis factor has been demonstrated in humans [114]. Fluorescent molecular imaging can obtain high sensitivity detection with low instrumentation expense compared with other molecular imaging approaches.

Fluorescent imaging is also used to assist surgeons in delineating malignant from benign tissue. The increasing availability of fluorescent proteins, dyes and probes enables the non-invasive study of gene expression, protein function, protein-protein interactions and a large number of cellular processes [115]. This body of information has great attention for using fluorescent molecular imaging especially using agents that emit in the near infrared fluorescence range.

3.3.1.1 Near-infrared (NIR) Optical Imaging

High-resolution near-infrared (NIR) optical imaging has become an attractive modality for non-invasive visualization of deep tissues. Because of its high tissue permeability, low absorption and low scattering of NIR light as well as low auto fluorescence, near-infrared (NIR) dyes have received increasing attention in recent years as diagnostic and therapeutic agents in the fields of tumor research and clinical applications. They are small organic molecules that function in the NIR wavelength region (700–1400 nm). Compared to other modalities such as magnetic resonance imaging (MRI), X-ray computer tomography (X-ray CT), and positron emission tomography (PET), NIR optical imaging has a high spatiotemporal resolution (~µm) enough to visualize cellular dynamics at the whole-body level. In addition, NIR optical imaging has no radiation effect. Molecular imaging can also be achieved easily using NIR optical probes, such as antibodies which specifically bind over expressed cancer cell surface antigens.

3.3.1.2 MULTISPECTRAL IMAGING Multispectral Imaging (MSI)

This is a fluorescence-based optical technique which optimizes the opportunities for multiplexing while at the same time overcoming the effects of autofluorescence on detectability and reliable quantitation [116]. In this technique, it is possible to acquire multispectral datasets by simply rotating a filter wheel in front of a CCD camera. The use of electronically tunable filters (no moving parts, continuous tunability) is also attractive. When the multispectral image set is captured, spectral unmixing and signal quantitation and display complete the imaging process. This system offers a high spatial resolution, good reagent flexibility, high throughput, and compatibility with relatively high levels of multiplexing.

The Maestro™ is one of the multispectral imaging systems (CRi, Woburn, MA, 01801) which are used for imaging small animals and their organs separately [116]. The system uses liquid crystal tunable filters which are band-sequential filters and easily coupled to focal plane array detectors employing CMOS, standard CCD, or EMCCD technologies, among others. A complete image can be acquired by sequentially tuning the filter and exposing the sensor at each wavelength. The user can easily vary the exposure time as a function of wavelength. Therefore, this allows the ability to optimize signal-to-noise in situations where sensitivity (emitted photons convolved by imaging receiver characteristics) varies over the spectral range. Moreover, it is possible to maximize signal-to-noise by acquiring only the most informative bands because the wavelengths acquired can be arbitrarily spaced through the spectral range of interest.

3.4 Radio-immuno-Imaging

Many tumors have either unique or over-expressions of specific receptors that can be exploited for both diagnosis and therapy [117]. Currently, there are several approved radiopharmaceuticals specifically targeting cancer surface receptors and a major amount of ongoing research to develop new receptor-based imaging agents (Figure 7) [118]. Tumor receptor imaging provides complementary information which includes evaluation of the entire tumor and characterization of the heterogeneity of tumor receptor expression. The most important element for tumor receptor targeting is the nature of the ligand-receptor interaction [119]. There are several considerations regarding the selection of specific radionuclide, ligand linker, and labels for different situations. Notably, the requirement of imaging probe is that it should be low molecular concentration to avoid saturating the receptor and increasing the background because of nonspecific uptake, and also the metabolic stability *in vivo* pharmacokinetics, and imaging label characterization. The label should remain attached to the ligand so it will not accumulate in normal tissue. The ligand should have high receptor specificity and affinity so that it binds to the desired receptor well and does not bind significantly elsewhere. More importantly, the label must have a half-life that matches with the rate that the ligand binds to the receptor and clears from the background. Antibodies bind very effectively to specific receptors and have long half-life.

One well-known antibody example in binding to a cell receptor is capromab pendetide, which binds specifically to the prostate specific membrane antigen (PSMA) [120]. There are many receptors highlighted, and recent investigations of receptor imaging with other molecular imaging modalities are reviewed. Molecular imaging of tumor receptors has been mainly confined to radionuclide imaging (PET and SPECT), with which it is possible to generate images with micromolar to picomolar concentrations of imaging probes. In addition, using optical imaging based on near-infrared appears promising.

Table 7. Examples of preclinical RIT studies in solid tumors adapted from reference [71]

Target antigen	Targeting moiety	Radionuclide	Model
hK2	Murine Ab	^{177}Lu	Prostate cancer
CD138	mAb	^{213}Bi	Ovarian carcinoma
EGFR	mAb	^{177}Lu	OSCC
TROP-2	mAb	^{177}Lu	Prostate cancer
GPA33	mAb	^{177}Lu/^{86}Y	Colorectal cancer
NaPi2b	F(ab')2	^{211}At	Ovarian cancer
PSMA	mAb	^{177}Lu	Prostate cancer
HER2	mAb	$^{212/213}$Bi	Colon adenocarcinoma
HER2	Affibody	^{177}Lu	Ovarian carcinoma
HER2	mAb	^{212}Pb	Colon adenocarcinoma
CD138	mAb	^{131}I	Breast carcinoma
HER2	mAb	^{227}Th	Breast carcinoma
FR	F(ab')2	^{131}I	Ovarian cancer
EGFR	mAb	^{177}Lu	Epidermoid carcinoma
MUC1	mAb	^{177}Lu	Breast carcinoma
HER2	mAb	^{177}Lu	Breast carcinoma
PD-L1	mAb	^{111}In	Breast carcinoma
HER2/EGF bsRICs	bsRICs	^{177}Lu/^{111}In	Breast carcinoma
EGFR	mAb	^{213}Bi	Bladder carcinoma
L1CAM	mAb	^{177}Lu	Ovarian cancer
ROBO1	mAb	^{90}Y	Small cell lung cancer
TfR	mAb	^{90}Y	Pancreatic cancer
Lewis Y	mAb	^{177}Lu	Colon carcinoma

In this project SAS1B receptor was the image target using radiolabeled anti-SAS1B as will be discribed in more details in following chapters.

CHAPTER 4: APPROACH AND METHODS

4.1 Introduction.

A number of monoclonal antibodies (Anti-SAS1B) have been produced including SB2, SB3, SB4, and SB5 and according to UVA studies, most of these antibodies were identical [121]. Therefore, SB2 and SB5 were selected for labeling with radioisotopes and near infrared dye and then investigated *in vitro* and *in vivo* studies. Among a number of radioisotopes and based on their physical and chemical properties, ^{89}Zr and ^{67}Cu were selected to radiolabel anti-SAS1B antibodies for *in vivo* imaging and *ex vivo* biodistribution studies.^{89}Zr possess favorable characteristics antibody-based for PET imaging [122], [123]. In addition, the production of ^{89}Zr was carried out in-house at VCU. ^{67}Cu emits gamma radiation which can be used for Single-Photon Emission Computed Tomography (SPECT) [124]. Also,^{67}Cu it is one of the best suited isotopes for radioimmunotherapy because its half-life is long enough to allow good biodistribution within the tumor [125]. These radionuclides require bifunctional chelators to obtain the best labeling with antibodies [126]. Bifunctional chelators are capable of coordinating a metal ion and can also be attached to the antibody [127] . Each radionuclide has its favorable chelators which can form a complex and reduce detachment of radioisotope [128]. Labeling anti-SAS1B antibodies done indirectly through two steps including optimization of antibody to the chelator conjugation and labeling with radionuclide to form a complex with the chelator. Labeling antibodies is challenging because there are many factors that need to be addressed during conjugation and labeling including the optimal ratio between chelator and antibody, reaction solution, pH, temperature and time of the reaction [90].

The other imaging agent used for an optical imaging was near infra-red dye (IR800CW). IR800CW dye is one of the main dyes used for fluorescence imaging [129]. Near infra-red dyes provide deep-tissue and real-time fluorescence imaging [130]. IR800CW linked to NHS-ester group which bind to antibody directly through amid group and the excess of dye could be removed using size exclusion column. Optimizing the molar ratio of dye-to-antibody is important to determine the best ratio of anti-SASB1 to dye and used for *in vitro* and *in vivo* experiments. Among anti-SAS1B antibodies, (SB5) was selected for radiolabeling with ^{89}Zr and (SB2) was labeled with ^{67}Cu and NIRdye 800CW as described below.

4.2 Synthesis of Non-radiolabeled and ^{89}Zr Radiolabeled anti-SAS1B (SB5).

Anti-SAS1B (SB5) was labeled with ^{89}Zr indirectly through DFO-NCS linker (Chelator) through two steps. First, SB5-DFO cold conjugation was optimized and then labeled with ^{89}Zr. ^{89}Zr readily available from our in- house cyclotron. ^{89}Zr exists as large ion and +4 cation in aqueous solution, and can be classified as a hard cation [131], so it exhibits a preference for ligands bearing up to six hard, anionic oxygen donors with chelators such as Desferrioxamine B (DFO) [132]. Desferrioxamine B was selected for this study because it is currently the best available ligand for Zirconium chelation and its use has been demonstrated in a number of preclinical and clinical studies [133]. DFO is a bacterial siderophore bearing 3 oxime groups. Computational studies strongly suggest that DFO forms a hexacoordinate complex with Zr4+ in which the metal center is coordinated to the three neutral and three anionic oxygen donors of the ligand as well as two exogenous water ligands as shown in Figure 12.

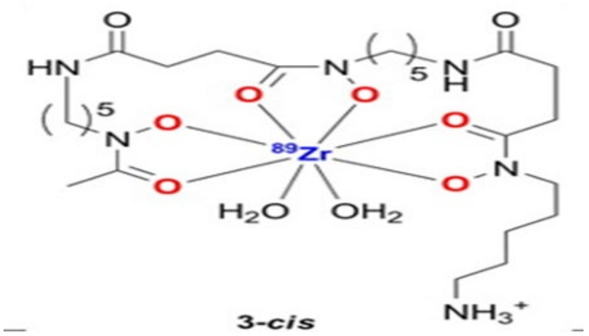

Figure 12.Coordination complex of [^{89}Zr]- DFO chelation. Adapted from ref [134].

4.2.1 SB5 Conjugation

The conjugation reaction schematic is depicted in scheme 5. Fifty µg of SB5 was added to 500µl of PBS (phosphate buffered saline solution) and the pH was adjusted to 8.8-9.0 using 0.1M sodium bicarbonate. DFO solution was prepared by weighting 0.2 mg added to 150 µl of DMSO to make 1.5 mg/ml solution. From DFO solution, 20µL was taken and added to SB5 mAb solution. The mixture was incubated at 37°C and mixed a rotating speed of 300 rpm for 60 minutes.

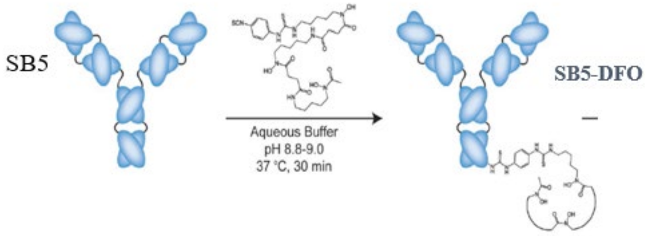

Scheme 5 Reaction Schematic of DFO to SB5 Conjugation.

4.2.1.2 SB5-DFO Characterization.

The conjugation yield of SB5-DFO was monitored using HPLC-UV (High-performance liquid chromatography and ultraviolet detector) with size exclusion column (SEC) (Superdex 200 10/300 column GE Healthcare, Piscataway, NJ USA) at room temperature. 0.01 M phosphate buffer and 0.14 M NaCl, pH 7.4 were used as mobile phase at flow rate of 0.5 mL min. UV detection was accomplished at 280 nm using a Waters 2489 UV (10-mm, 11-µL analytical flow cell).

4.2.2 Radiolabeling SB5 with ^{89}Zr.

Zirconium-89 was produced in the cyclotron using the ^{89}Y (p, n) ^{89}Zr reaction using 13 MeV incident proton energy. Following radiochemical processing, ^{89}Zr was obtained in the form of Zirconium-oxalate solution. [^{89}Zr]-oxalate (4.2 mCi/500uL) solution was neutralized with 200uL of 2M Na2CO3. 15uL of [^{89}Zr] - oxalate solution was added to SB5-DFO conjugation solution and incubated for 30 minutes. Radiolabeling reaction schematic is shown in scheme 6.

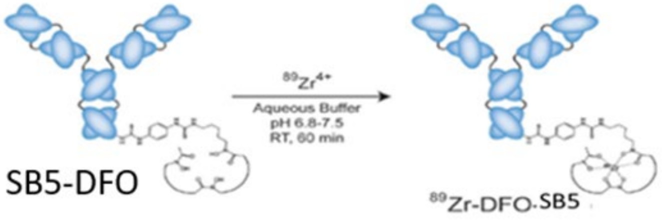

Scheme 6 Reaction Schematic of radiolabeling of SB5-DFO with ^{89}Zr ([^{89}Zr]-DFO-SB5).

4.2.2.1 ^{89}Zr-DFO-SB5 Characterization

The reaction yield was monitored by radio-HPLC. Radio detector was connected to UV-HPLC to detect the radio activity signal of labeled antibody. This one of the methods used to determine the radiochemical purity of radiolabeled antibodies. Radiochemical species can be separated according to the molecular size and weight, and the peak of radiolabeled antibody will correspond to the peak in UV-HPLC. The [^{89}Zr]-DFO-SB5 solution (20ul) was loaded on Radio-HPLC from waters using size exclusion column (SEC) (Superdex 200 10/300 column GE Healthcare, Piscataway, NJ USA) and the radio detector was connected to the HPLC is Bioscan, INC, model BFC-3300.The mobile phase was 0.1 M phosphate buffer and 0.14 M $NaCl_2$, pH 7.4, at a flow rate of 0.5 mL min.

4.2.2.1.2 Radio-TLC. Thin-layer Chromatography

The radiolabeled SB5 [^{89}Zr]-DFO-SB5 was also monitored by radio-TLC. Thin-layer chromatography was performed on TLC plates (silica gel plates [Sigma-Aldrich,St. Louis, MO]). TLC plates at heights 10cm approximately 1*u*l of the final solution were spotted at the center of the 2 cm mark from the bottom. The spot was allowed to dry for 5 to 10 minutes. The plates were then placed into a TLC jar filled to about 1cm from the bottom with 10% ammonium acetate and methanol (1:1) as a mobile phase, and allowed to develop to the 7 cm line from the bottom (about 15 minutes). In this system radiolabeled antibody remains at the origin, while free [^{89}Zr] migrate to the solvent front. Also, Size exclusion column PD10 was used to purify [^{89}Zr]-DFO-SB5. Using this column allowed to sort out all labeled antibody from other radioactive components by collecting small fractions of the reaction solution and determine the radioactivity using TLC.

4.2.3 *In vitro* study of [^{89}Zr]-DFO-SB5

4.2.3.1 Cell lines and Cell Culture.

SNU539 (Seoul National University) cell lines have been cultured to use them as expressed target for *in vitro* and *in vivo* study. SNU539 cell lines were established from Korean cancer patients since 1982 and reported in many SNU cancer cell lines, SNU539 was characterized and reported in uterine tumor tissue (56). SNU539 Cell lines were grown and maintained in RPMI1640 supplemented with 10% heat inactivated fetal bovine serum (Hyclone,Logan,UT), 2mM L-glutamine (2mmol/L), 100 ug/ml streptomycin (Sigma, St. Louis MO). 10 mM HEPES in a humidified, 5% CO2 incubator at 37°C. Every other day cells were checked and medium replaced. When cells growth covers about 70% of the flask, cells detached using accuatase enzyme. Then, cells were collected, counted and regrow again. When the number of cells reached the required number for experiments, all cells were harvested.

4.2.3.2 Cell Uptake

SNU539 cells were cultured and different concentrations prepared 4x10^6, 2x10^6 and 0.5x10^6 for cell uptake of [^{89}Zr]-DFO-SB5. Cells were incubated at 37°C for 2 hours with the same amount of radioactivity [^{89}Zr]-DFO-SB5. After 2 hours, all cells were washed using PBS and spun for 5 minutes at 1000 rpm. After spun all tubes, supernatant was removed and replaced with PBS. The radioactivity of participation cell pellets and supernatants were measured using gamma counter. The uptake of cell was calculated and presence of radioactivity of cells reflects the binding of radiolabeled SB5 to SAS1B antigens on cell surface.

4.2.4 *In vivo* imaging of SAS1 Targeting by [^{89}Zr]-DFO-SB5.

4.2.4.1 Animals

Animal experiments were performed according to the policies and guidelines of the Animal Care and Use Committee (IACUC) at Virginia Commonwealth University. Female nude mice 3 weeks old, obtained from the National Cancer Institute in Bethesda, MD, were caged in groups of five or fewer, and provided with food and water ad libitum. All animal experiments were performed for this study in accordance with Institutional Animal Care and Use Committee (IACUC) guidelines and approved protocol at Virginia Commonwealth University.

4.2.4.2 Mouse Tumor Model

SNU539 cells were inoculated subcutaneously into mice flanks to implant xenograft tumors. About (5 × 10^6) of SNU cells in 130ul of phosphate buffer mixed with 30% matrix gel was injected in each mouse. The tumor growth was monitored using a caliper. When the tumor size reached about 1mm in diameter and the volume less than 2000mm^3 (Tumor volume calculated using this formula V= W*2*L/2 [135]) animal were used for *in vivo* imaging and biodistribution study.

4.2.4.3 PET/CT Imaging

[^{89}Zr]-immuno-PET is a quantitative technique to measure the uptake of radiolabeled antibody in tumor-associated antigens and the distribution in other organs. A female nude mouse was injected via tail vain with 247µCi of [^{89}Zr]-DFO-SB5. After intervals of 2 hours, 24 hours, and 72 hours, the mouse was anesthetized by 1% to 2% isoflurane inhalation anesthesia, then positioned in PET/CT system and images were obtained. The region-of-interest (ROI) was analyzed with the percent injected dose/gram of tissue (%ID/g). The animal was imaged by both PET and CT. CT image provided anatomical background for distribution of the radioactivity. Figure 13 shows *in vivo* experiments flow work.

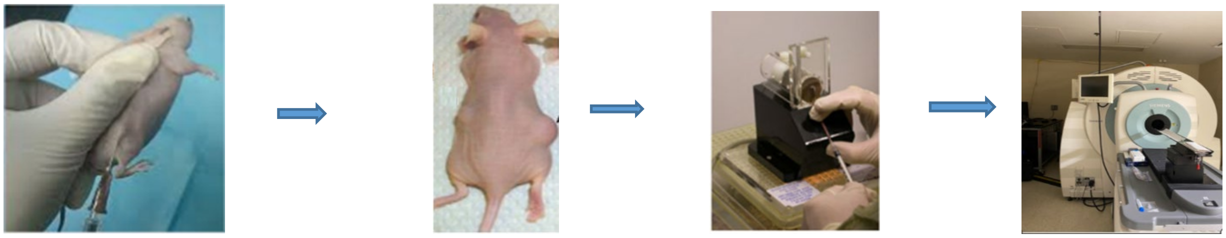

Inoculating cancer cells   Xenograft tumor mouse model   Injecting Radiolabeled mAb   PET at 2, 24 and 72

Figure 13. *In vivo* flow work.

4.2.4.4 *Ex Vivo* Biodistribution

The biodistribution of [^{89}Zr]-DFO-SB5 in animals was determined by organ following injection and animal sacrifice. Five nude mice bearing SNU539 tumor xenografts were divided in two groups. The first group of 3 mice were injected with a solution of [^{89}Zr]-DFO-SB5. The other groups of 3 mice were injected with the non-specific labeled antibody [^{89}Zr]-DFO-3A4 (as negative control) via the tail vein. After 24 hours, one of the mice died. All other mice were sacrificed, blood and tissues were collected from each animal and weighed, and radioactivity of ^{89}Zr in each sample was determined by gamma-counting on a Perkin Elmer Wallac Wizard 1470. The radioactivity percent of injected dose per gram %ID/g of each organ was calculated using all data, including activity of injected solution (Standard), organs weighed and measured activity of each organ.

The collected organs were blood, heart, lung, liver, gallbladder, spleen, kidney, tumor, femur, and muscle.

4.3 Radiolabeling SB2 with Copper-67 (^{67}Cu)

In addition to Zirconium-89 (^{89}Zr), radiolabeling of SB2 was also investigated using another radionuclide, Copper-67 (^{67}Cu). ^{67}Cu is an attractive theranostic radionuclide because its decay results in the emission of both therapeutic (beta particles) and imaging (gamma-rays) radiation. It emits beta particles with a mean energy of 141 keV and three gamma rays (91, 93 and 182 keV) suitable for SPECT imaging [124]. Additionally, the half-life of ^{67}Cu is 62 h is well suited to the bio kinetics of antibodies [136]. Additional advantages to these favorable physical characteristics of ^{67}Cu are the availability of copper chelators with high *in vivo* stability [136]˒ [137]. In this study the chelator p-SCN-Bn- DOTA (S-2-(4-Isothiocyanatobenzyl)-1, 4, 7, 10-tetraazacyclododecane tetra acetic acid) was selected to link ^{67}Cu to SB2. It is an attractive candidate for conjugation of radioisotopes to antibodies [138]. In general, macrocycles, like DOTA form complexes that are essentially irreversible under physiological conditions and demonstrate higher thermodynamic stability than linear chelators, such as DTPA [139] (Figure 14).

In order to determine the optimum molar ratio of DOTA: SB2, experiments were carried out to determine best ratio for radio-labeling.

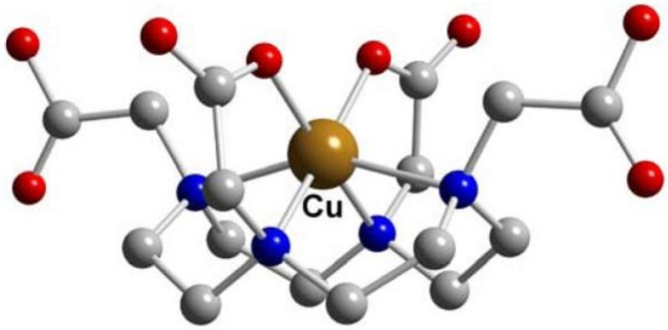

Figure 14. Structure of [^{67}Cu]-DOTA complex adapted from reference [123].

4.3.1 Optimizing SB2-DOTA Conjugation

Determining the molar ratio of chelator binding to antibody is an important factor for optimized radiolabeling. Chelators bind to amino acids on the antibody through the functional group of the chelator. The p-Isothiocyanatobenzyl DOTA is one of the favored bifunctional chelators for labeling antibody with copper radioisotope. It forms hermodynamically very stable complexes with copper through the coordination chemistry[123], [136]. DOTA is water-soluble and reacts easily in slightly basic solutions (pH 8–9) with lysine side chains which is one of the most common residues on antibody surfaces [140].

DOTA-SB2 Conjugation was optimized by preparation of multiple molar ratios of SB2-DOTA conjugation (1:3, 1:5, 1:7 and 1:10) and incubated at 37C for 24 hours. The conjugation yield was determined by UV-HPLC using size exclusion column (Phenomenex Yarra SEC 2000 150x 4.6mm) and mobile phase of 0. 1M Sodium phosphate buffer pH 6.8 with flow rate was 0.35 ml/min with. The conjugation was monitored for one week at different time points (0, 1, 2, 4, 6, 8, 10 and 24 hours) by injecting 20ul from conjugation solution into the HPLC.

4.3.2 Radiolabeling SB2. [^{67}Cu]-DOTA-SB2

Based on the successful optimization of SB2-DOTA conjugation, ^{67}Cu was then used for radiolabeling. Cold conjugation of SB2-DOTA at 1:5 ratio was prepared in solution volume of 200ul of potassium phosphate buffer, and the pH was adjusted between (8 -9) using 0.1M of sodium bicarbonate. 10ul (362uCi) of [^{67}CuCl$_2$], in 0.1M HCl (pH=5.0-5.5) was added to SB2-DOTA (pH= 8-9) solution and the pH was adjusted to about 6- 6.5, using 0.1M HCL. The reaction was incubated 37°C for 30 minutes. Radiolabeling efficiency and radiochemical purity of [^{67}Cu] -DOTA- SB2 was determined by radio-TLC using 10% (w/v) ammonium acetate: methanol (1:1) as the mobile phase. In this system, radiometal-labeled antibody [^{67}Cu] -DOTA- SB2 remains at the origin, while DOTA-[^{67}Cu] or free ^{67}Cu will migrate to the solvent front on ITLC plates.

4.3.2.1 Purification with PD10

ITLC showed high labeling yield of SB2 antibody [^{67}Cu] -SB2-DOTA and some of [^{67}Cu]-DOTA-or ^{67}Cu. In this case, Size exclusion column PD10 was used to purify labeled antibody from other species.

4.3.3 *In Vitro* Evaluation

4.3.3.1 Cell Uptake

SNU539 uterine cancer cell line and SK-OV3 human ovarian cancer cell lines were used for study. Both cell lines were grown at 37°C and were maintained until cell count reached about 50 million. In triplicate, vials with 1 million cells in 1m of growth medium were prepared, and 100µl of [^{67}Cu]-DOTA-SB2 solution was added to each vails. All vials were incubated at 37°C for 4 hours, followed by spinning at 1000 rpm for 5 minutes. Then, supernatant was collected, and the cell pellets were washed three times with PBS. The radioactivity of all samples, cell pellets, supernatant, and wash tubes were measured by gamma counter and the uptake for both cell lines was calculated.

4.3.4 *Ex Vivo* Evaluation

Animal experiments were performed according to the policies and guidelines of the Animal Care and Use Committee (IACUC) at Virginia Commonwealth University. Biodistribution studies of both $^{67}CuCl_2$ and [^{67}Cu] - DOTA were performed ex vivo on 12 female nude mice. After these mice were divided into two groups, one group was injected with ^{67}Cu and the other group injected with [^{67}Cu] - DOTA. The biodistribution for these two compounds were measured after 1 and 6 hours as described below.

4.3.4.1 DOTA-[^{67}Cu] Biodistribution

Six mice were injected via tail with 200ul of [^{67}Cu]-DOTA (2μCi) solution and divided into two groups. Biodistribution was determined in the first group after 1 hour and the other group after 6 hours (n=3). Therefore, the first group of mice was dissected after 1 hour (n=3), and the second group was dissected after 6 hours (n=3). All organs were collected to measure the radioactivity of [^{67}Cu]-DOTA in each tissue by gamma counter. Data showed rapid clearance of [^{67}Cu]-DOTA from the kidney after 6 hours while slow in blood, liver, and spleen, (Figure 20). Also, there was no uptake of [^{67}Cu]-DOTA by the brain and less uptake in bones and muscles.

4.3.4.2 $^{67}CuCl_2$ Biodistribution

Similarly, ^{67}Cu (4uCi) 200ul volume was injected via tail in triplicate mice. The first group of mice was dissected after 1 hour and the other group dissected after 6 hours. All organs were collected, and ^{67}Cu activity in all organs was determined by gamma counter.

4.4 Labeling SB2 with NIRdye800CW

NIR dye 800CW is one of the most used dyes for fluorescence image-guided surgery [141]. It has less interaction with serum proteins and, when injected intravenously, cleared through the kidney with some uptake in the liver [142]. The most commonly applied strategy for labeling antibodies by using the activated group N-hydroxysuccinimide (NHS)-ester to form covalent bond between primary amines of the antibody and carboxylic acid of (NHS)-ester [143] (Figure 15). This conjugate to N-terminus of lysine residues which is the most abundancy and accessible amino acids in antibodies. As a result, having this could lead to many fluorophores per targeting antibody and cause self-quenching, which will reduce brightness and also, when the fluorophores are conjugated in or close to the antigen-binding region, could impact the binding capacity [144]. Therefore, optimizing the conjugation of antibody with NIR dye 800CW is important to determine the degree of labeling that can give high fluorescence signal *in vivo* with less background.

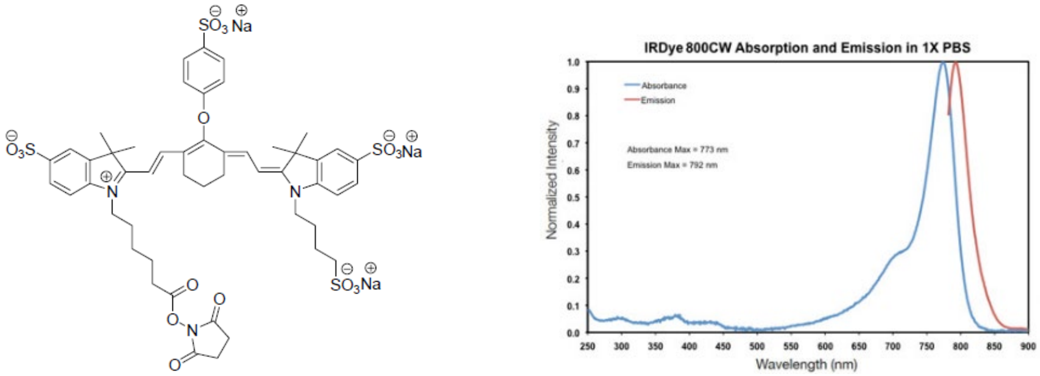

Figure 15. NIR dye 800CW NHS-ester structure and absorption and emission spectra.

4.4.1 Optimizing the Conjugation of Monoclonal Antibody to IRdye800CW

Conjugation of monoclonal antibody SB2 (155 kDa) with NHS-IRDye800CW from LI-COR Biosciences (absorption/Emission: 774/789nm) was optimized by following LI-COR conjugation protocol. The stock solution was prepared by dissolving 0.1mg dye with 25ul of ultra-pure water and mixed thoroughly. The antibody solution was prepared by adding 50ug (0.33nmol) of SB2 to 125ul of phosphate buffer. The antibody was combined with reconstituted reactive dye at different molar ratio 1:1, 1:2, 1:3 and analyzed to determine the optimal conjugation ratio. IR800CW dye was added to SB2 solution and the pH was adjusted between 8.3 - 8.5 using 1M of potassium phosphate buffer K_2HPO_4 , pH 9. The reaction solution was incubated at 20°C -25°C for 2 hours. The excess amount of free dye was removed using Zeba desalting column (Thermo Fisher Scientific) after equilibrated with 50mM phosphate buffer, pH 8.5. The conjugation yield was determined using UV/Vis systems.

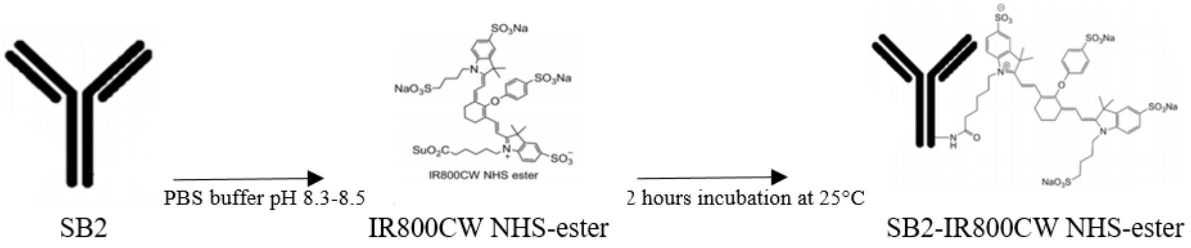

Scheme 7 Labeling SB2 with IR800CW.

4.4.2 *In Vitro* Evaluation

4.4.2.1 Cell Culture

SNU539 Cell lines grown in RPMI1640 were supplemented with 10% fetal bovine serum, glutamine (2 mmol/L), penicillin (100 unit/ml), HEPES and maintained in a humidified, 5% CO_2 incubator at 37°C. When cells reach about 70% of growth in the flask, cells detached using accutase enzyme and collected. Then cells viability checked using trypan blue and counted. All cells harvested when reach the number needed for *in vitro* experiments.

4.2.2 Cell Binding

Both SNU539 and SK-OV3 express SAS1B, but A549, a lung cancer cell line does not express SAS1B. About 0.1x106 of each cell line were grown in 6 plate wells for 24 hours at 37°C. After 24 hours cell growth, the media was discarded and cells incubated with SB2 labeled with NIR dye 800CW solution at 37°C for 1 hour. Another 6 well plate with the same cells was incubated with IgG labeled with NIRdye800CW for 1hour. All cells were washed using phosphate buffer and examined by fluoresce microscope.

4.5 Statistical Analysis

The significant differences in the *ex vivo* and *in vivo* studies were determined using the equal variance analysis (ANOVA) (JMP software), or Student's t-test. P value of <0.05 was considered as statistically significant difference. The data shown in graphs are mean SEM.

CHAPTER 5: RESULTS

5.1 Radiolabeling SB5 with ^{89}Zr

5.1.2 SB5 Conjugation

High-performance liquid chromatography (HPLC) results showed high reaction yield of DFO–SB5 cold conjugation (Figure 16). The peak of SB5 was at 24 minutes retention time. The small peak at retention time 37.12 represent DFO. The area under the peak represents the conjugation yield of DFO to SB5. As the HPLC chromatograph show, about 92% of DFO was conjugated to SB5.

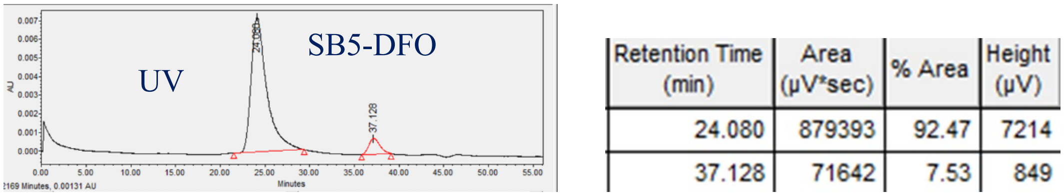

Retention Time (min)	Area (µV*sec)	% Area	Height (µV)
24.080	879393	92.47	7214
37.128	71642	7.53	849

Figure 16. Conjugation of anti-SAS1B (SB5) to DFO (SB5-DFO), 20ul of conjugation reaction was injected into HPLC. The chromatogram shows 92% conjugation yield. The retention time of (SB5) mAb was 24.1 minutes and DFO retention time was 37.2 minutes.

5.1.3 SB5 Radiolabeling

5.1.3.1 Radio-HPLC Chromatography

Radio-HPLC was used to determine the radiolabeling yield of SB5 and the radioactive signal should match the UV-HPLC SB5 signal if the ^{87}Zr label SB5. The radio-HPLC chromatograph showed that the majority 66.96% of radioactive signal matches the UV signal of SB2. There were also multiple small peaks which could be SB5 fragments (Figure 17).

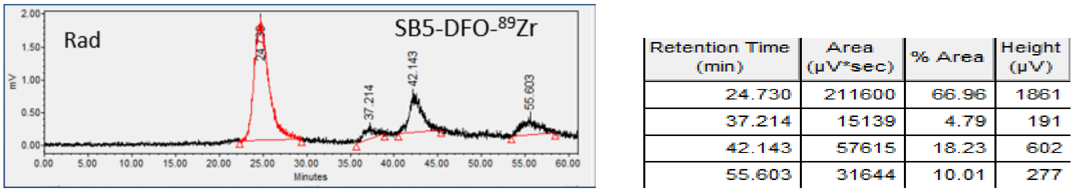

Retention Time (min)	Area (µV*sec)	% Area	Height (µV)
24.730	211600	66.96	1861
37.214	15139	4.79	191
42.143	57615	18.23	602
55.603	31644	10.01	277

Figure 17. Radio HPLC shows radiolabeled SB5 ([^{89}Z]-DFO-SB5). Also, it shows also small peaks which could be radiolabeled SB5 fragments.

5.1.3.2 Radioactive Instant Thin-layer Chromatography. (Radio-ITLC of [^{89}Zr-DFO-SB5]

The radio-instant thin layer of chromatography showed high radioactive signal of labeled SB5 with very small signal representing free ^{89}Zr or [^{89}Zr]-DFO (Figure 18).

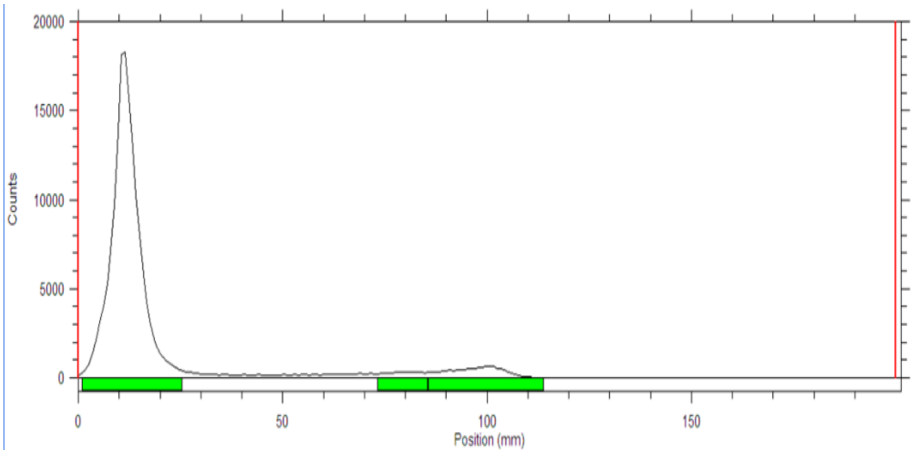

Figure 18. Radio-TLC of [^{89}Zr] - DFO-SB5 showing quantitative radiolabeling yield.

5.1.4 *In Vitro* Study Results

5.1.4.1 Cell Uptake

The radioactivity of participation cell pellet was measured using gamma counter. The presence of radioactivity of cells reflects the binding of radiolabeled SB5 to SAS1B antigens on cell surface. Results showed the radioactivity decreased by decreasing the cell concentration (Figure 19).

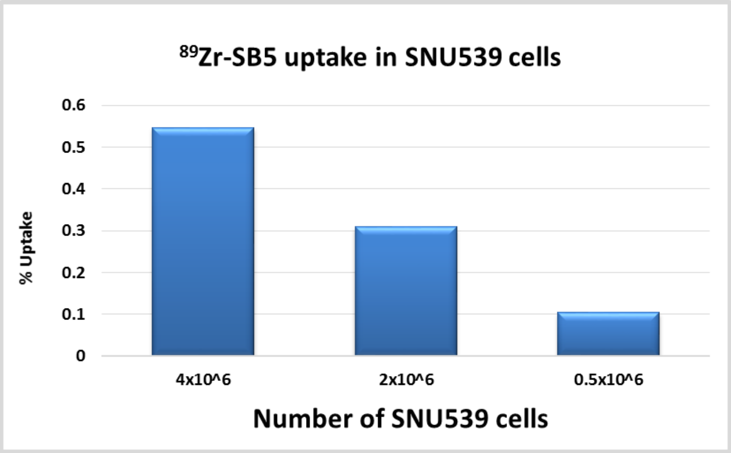

Figure 19. Radioactivity of different SNU539 cell concentrations after incubated for 2 hours at 37°C with Same amount of [^{89}Zr]-DFO-SB5 radioactivity.

5.1.5 *In Vivo* Imaging of SAS1B Targeting

5.1.5.1 Tumor Growth Monitoring

After injecting 5x10^6 of SNU539 cells subcutaneous into mice flank to implement the xenograft tumor, the mice were monitored for tumor growth. At week 4, the tumors started appearing and a clipper was used to take measurements of the length and width of the tumors. In most of the mice, tumor size took about 6-8 weeks to reach 1mm in diameter (Figure 20).

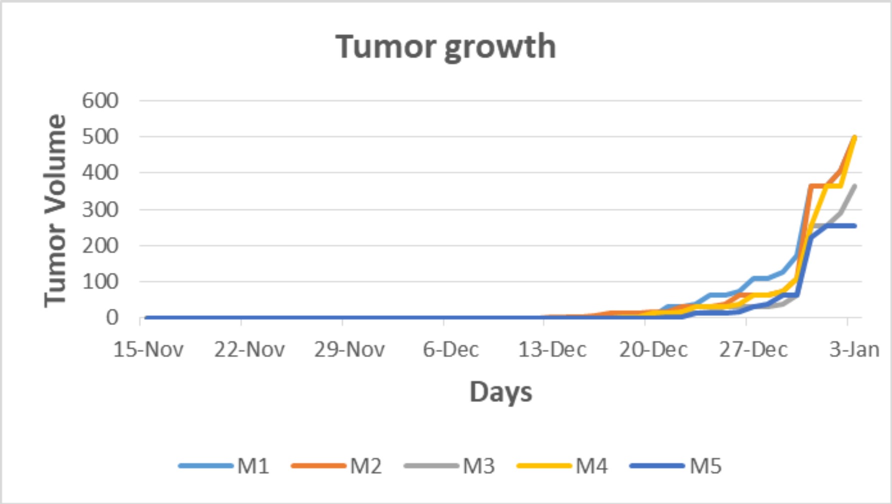

Figure 20. Monitoring Tumor growth.

5.5.2 PET/CT Imaging

The animal was imaged by both PET and CT. The CT image provided anatomical background for distribution of the radioactivity (Figures 21 and 22). As the image showed, the vast majority of radioactivity is following clearing from the blood, spleen, and liver, as well as other organs. The second observation is the right flank of the tumor showing uptake, while the left flank did not show any uptake. This uptake is because of SAS1B binding Labeled SB5. Also, more activity was noticed in the bone and this is more likely due to the detachment of ^{89}Zr from DFO and uptake by the bone.

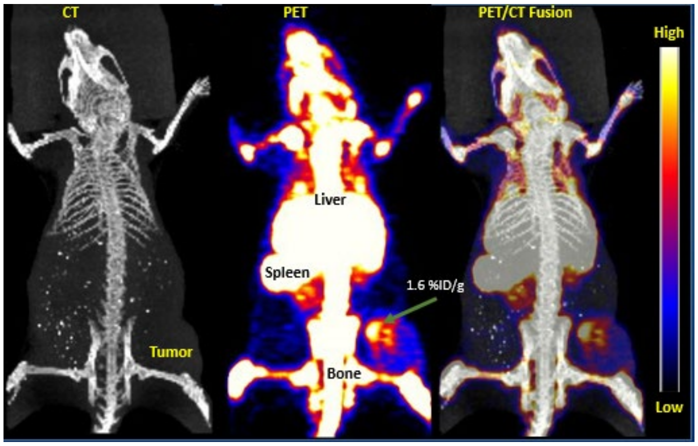

Figure 21. Whole female nude mouse bearing xenograft tumor injected with [^{89}Zr]-DFO-SB5 and imaged via PET/CT show the Maximum Intensity Projection 72 hours post injection. Low accumulation of [^{89}Zr]-DFO-SB5 in the tumor while high uptake in bone, liver, and spleen.

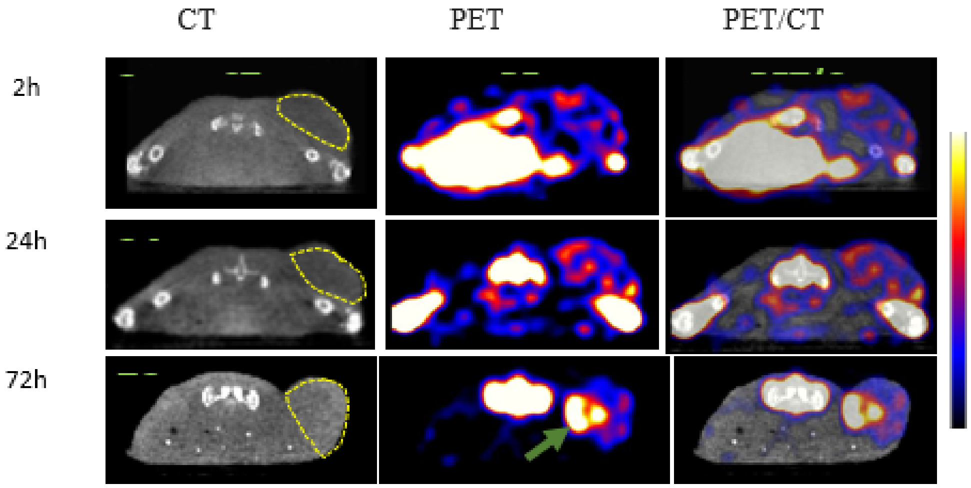

Figure 22. PET /CT coronal and sagittal images, across tumor area, taken at 2 hours, 24 hours, and 72 hours post inj. Region of interest (ROI) results showed average of less than 1% of activity shown in the tumor while more uptake in bone, spleen, and liver.

5.1.5.3 *Ex Vivo* Biodistribution

After 24 hours, biodistribution results showed that about 6% of radioactivity is in the blood and the major distribution is in the liver, spleen, and kidney (Figure 25). Also, an interesting observation is the non-specific antibody 3A4 (negative control antibody) is showing significantly lower uptake, although the specific antibody SB5 did not show significant tumor uptake (less 1%). Even though both antibodies were chelated by DFO, results showed more ^{89}Zr detachment from SB5 than 3A4 by looking to uptake of the most organs (Figure 23).

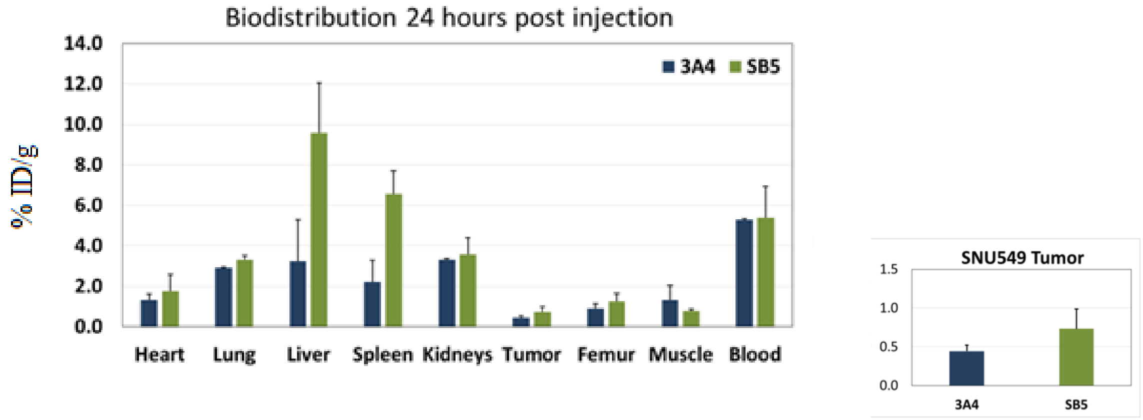

Figure 23. *Ex vivo* results of [^{89}Zr]-DFO-SB5 and [^{89}Zr]-DFO-3A4 biodistribution in two groups of mice after 24 hours. Data shows an average of less than 1% tumor uptake in mice injected with [^{89}Zr]-DFO-SB5 (Green) while high uptake in blood, liver, and spleen compared to kidney. Nonspecific labeled antibody [^{89}Zr]-DFO-3A4 (blue) showed very less uptake by tumor, and similar or less uptake in heart, lungs, kidneys, and blood.

5.1.6 Discussion

Cold conjugation of anti-SAS1B (SB5) with the chelator DFO was performed before labeling with ^{89}Zr according to published protocol [145]. The results showed greater than 90% of conjugation yield in most of SB5 and DFO conjugation. HPLC with size exclusion column was used to evaluate the cold conjugation yield [146] [147]. Firstly, anti-SAS1B and the chelator separately were injected into the HPLC to identify the retention time of each one, based on their molecular weight. Since antibody has higher molecular weight than the chelator, antibody retention time was 24 minutes, which is less than the retention time of the chelator DFO was at 37 minutes as shown in Figure 7. When the cold conjugation injected, the HPLC chromatograph showed two peaks. The area under the peaks represents the amount of antibody and the chelator in the conjugation reaction. Therefore, HPLC was used for quantitatively monitor the conjugation yield. If complete conjugation is achieved, we will see only one peak at the retention time of antibody. However, when both the antibody and chelate peaks are detected in the chromatogram, this indicates that the conjugation reaction did not go to completion and the area under the peaks reflects the degree of conjugation efficiency.

Once reaction parameters are optimized and validated by radio-HPLC, a second chromatographic method was used, namely radio-TLC. This offers a simple and quick method based on the migration of radiolabeled antibody versus the migration of non-antibody radioactivity on the TLC plate. This method was adopted for rapid evaluation once being validated by radio-HPLC. On the radio-TLC plate, the radiolabeled antibody will stay at the origin while non-antibody radioactive species will migrate to solvent front. This is done by scanning the entire plate using a faster radiation detection. Labeled SB5 [^{89}Zr] –DFO-SB5 was evaluated using thin layer chromatograph TLC and the chromatograph showed about 80% of SB5 was labeled with ^{89}Zr. Following the successful radiolabeling of SB5 and SB2 with different yields, the radiolabeled antibody needs to be purified from any non-antibody radioactivity. This has been accomplished by using PD10 desalting columns containing sephadex G-25 resin for rapid buffer exchange, desalting, and removal of small contaminants, including salts and radioactive labels. In this system, radiolabeled antibodies elute in the first few eluted fractions, while non-antibody radioactivity elutes in later fractions. Collected fractions are re-analyzed to confirm purity.

Purified [^{89}Zr]-DFO-SB5 was used for *in vitro* and *in vivo* experiments. Cell uptake study using radiolabeled [^{89}Zr]-DFO-SB5 and SNU539 cells showed that the amount of radiolabeled antibody taken up by the cells increases with increasing cell concentration. The level of radioactivity used ranged from micro curies for *in vitro* experiments to mille-curie levels for *ex vivo* and *in vivo* work [148]. For example, longitudinal imaging of the same animal and prolonged biodistribution studies usually require larger amounts of radioactivity to be injected in order to detect it days and weeks later, depending on the half-life of the radionuclides[149]. Moreover, one also needs to account for some radioactivity that may be lost due to retention in syringes, vials, and other materials encountered by the radioactivity [150]. In addition, the amount of radioactivity used need not be so high as to cause an effect on the antibody itself [151]. This is why the immunoreactive fraction of the antibody needs to be determined at different levels of radioactivity. Retention of immunoreactivity is also desirable following radiolabeling, as a low immunoreactive fraction could compromise binding of the antibody to its target protein SAS1B.

PET/CT images of [^{89}Zr]-DFO-SB5 uptake in general reflect the biodistribution profile, including some uptake in tumor (Figures 21 and 22). The bone uptake is indicative of ^{89}Zr detaching from the radio-conjugate and accumulating in bone. This observation has been reported in other studies [152] [153] [154]. The overall biodistribution of [^{89}Zr]-DFO-SB5 (specific for SAS1B) and [^{89}Zr]-DFO-3A4 (presumed to be non-specific for SAS1B) is similar across a number of tissues including blood. The SNU tumor uptake was slightly higher for [^{89}Zr]-DFO-SB5 than that for [^{89}Zr]-DFO-3A4, although the significance of this difference was not determined. It has been shown by western blot that SNU cells express more SAS1B antigen on their surface compared to 3A4 SAS1B expression level [155]. It is also worth noting that the uptake of [^{89}Zr]-DFO-3A4 is 2-3 times higher than that of [^{89}Zr]-DFO-SB5 in both liver and spleen at 24 hours post injection.

5.2 Radiolabeling SB2 with Copper-67 (^{67}Cu)

5.2.1 Optimizing SB2 & DOTA Conjugation

The choreographs of HPLC for the different ratios SB2-DOTA conjugation showed the highest yield of conjugation for both ratios 1:3 and 1:5, which were >95%% after 24 hours (Figure 24). HPLC chromatograph (Figure 25) shows SB2-DOTA peaks at the beginning of the reaction (Figure 25A) and after 24 hours (Figure 25B). Chromatograph shows the peak of DOTA is completely disappeared and the area under the peak of SB2 was increased, illustrating the complete conjugation of DOTA to SB2.

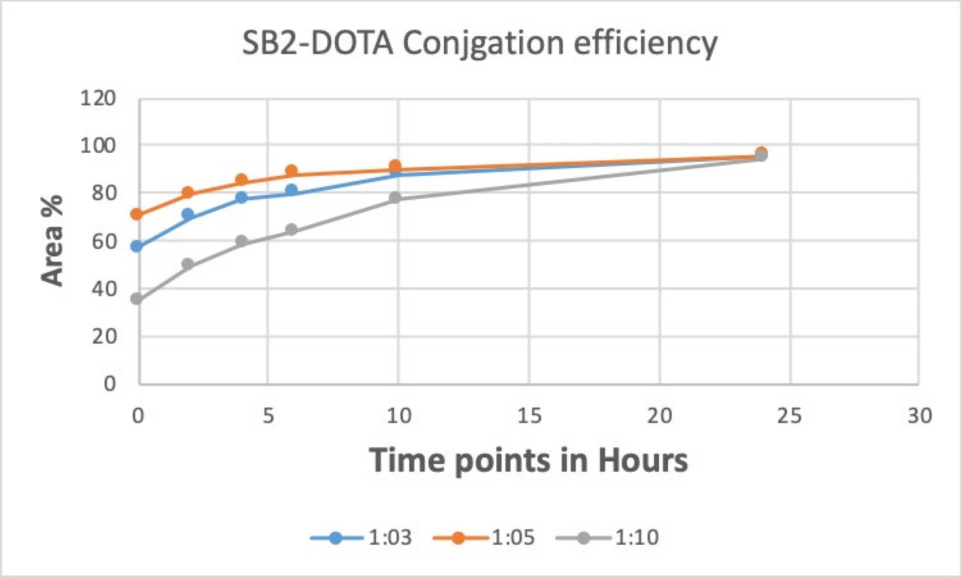

Figure 24. Optimizing SB2& DOTA conjugation, different ratio SB2 & DOTA (1:3, 1:5, 1:10) Conjugation yield was measured at 0,2,4,6,8,10 and 12 hour time points during 24 hours by 20ul from conjugation solution into HPLC.

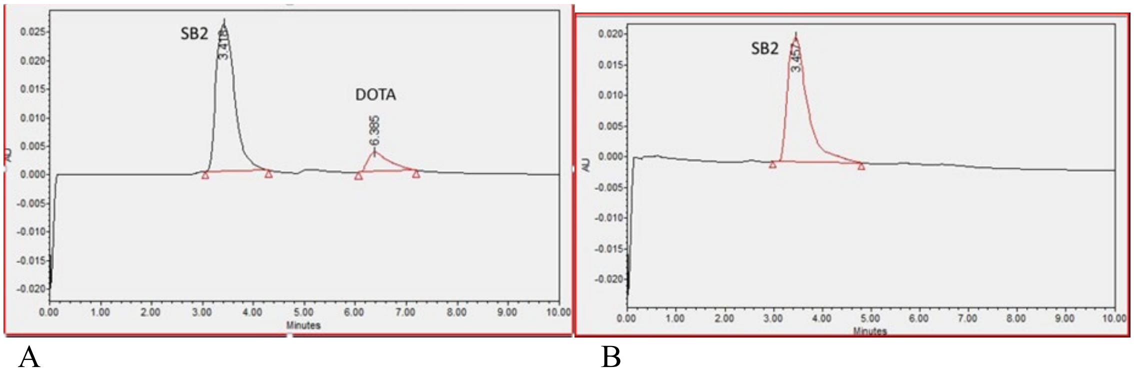

Figure 25.HPLC profile of SB2-DOTA conjugation ratio 1:5. 20ul of SB2-DOTA conjugation solution was injected into HPLC. (A) HPLC profile after 30 minutes of reaction. (B) HPLC profile after 24 hours of reaction. Almost 100 % of DOTA was conjugated to SB2 monoclonal antibody after 24 hours of reaction at 37°C.

SB2-DOTA Stability

Conjugation of SB2 with DOTA was stored at 4°C and monitored for one week. The results showed that SB2-DOTA conjugation was stable and the conjugation yield was above 90% (Figure 26).

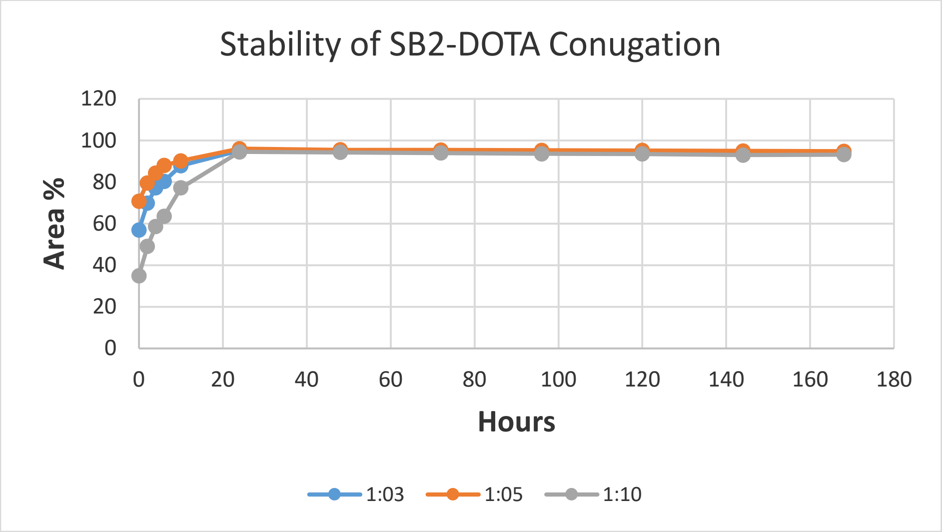

Figure 26 .Stability of SB2-DOTA was monitored for one week using HPLC. At each time point 20ul of SB2-DOTA solution was injected into the HPLC. The HPLC chromatogram showed SB2-DOTA conjugation remains stable for one week at 4°C.

5.2.2 Radiolabeling

Radio-TLC results showed >85% radiolabeling efficiency (Figure 27). Also, there is a small peak which represents free ^{67}Cu or DOTA-[^{67}Cu] or both together. Therefore, this is required purification.

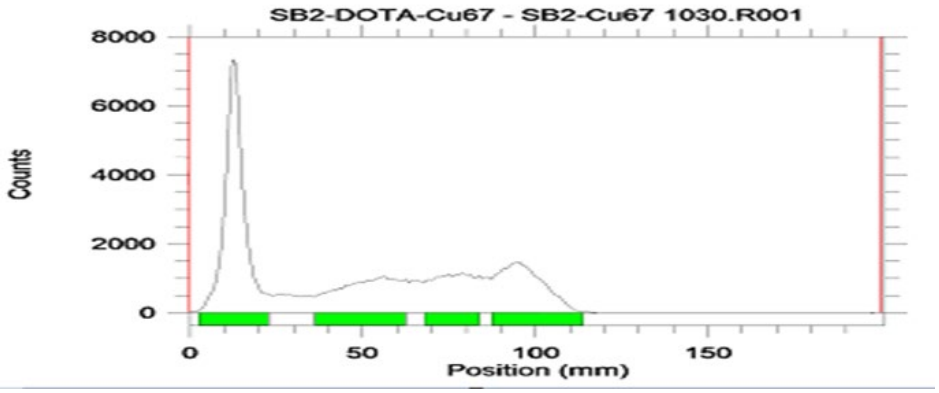

Figure 27. TLC result of [^{67}Cu] –DOTA-SB2. 1µl of [^{67}Cu] –DOTA-SB2 solution was spotted in TLC plates and scanned by gamma counter with the appropriate energy window to detect the labeling yield, which was > 85% of labeled SB2 ([^{67}Cu] -DOTA- SB2).

5.2.2.1 Purification with PD10.

PD10 was used to purify labeled antibody from other species. Figure 28 shows the purification result which was greater than 95% of [^{67}Cu] -DOTA-SSB2.

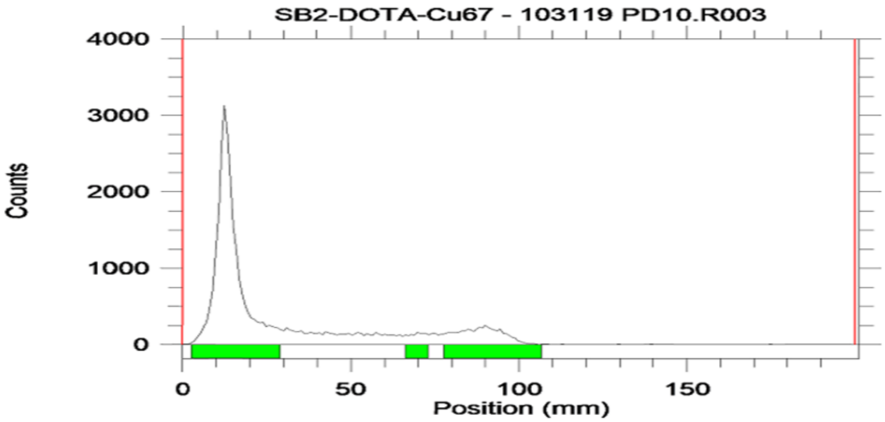

Figure 28. TLC results of purified [^{67}Cu] -DOTA- SB2 by PD10 column.

5.2.3 *In vitro* Evaluation

5.2.3.1 Cell Uptake

Results showed significant uptake of [^{67}Cu]-DOTA-SB2 by both SNU539 and SK-OV3 cell lines $p < 0.05$, while low uptake of [^{67}Cu]-DOTA and free ^{67}Cu (without antibody). The same radioactivity was used (4uCi) and all cell were washed very well using PBS. The result of radioactivity level associated with the cells confirmed specific binding of labeled SB2 to SAS1B surface antigen. (Figure 29).

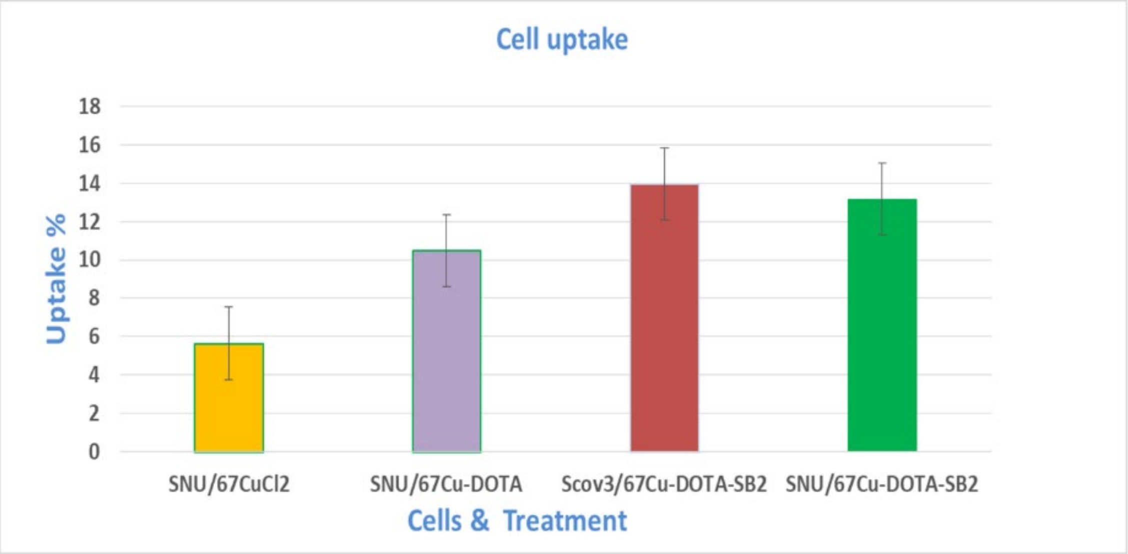

Figure 29. Results showed that labeled antiSAS1B (SB2) significantly targeted uterine cell lines SNU539 and ovarian cell lines SK-OV3 compared with [^{67}Cu]-DOTA or free [^{67}Cu]. SK-OV3 ovarian cell lines also express SAS1B antigens (24). Further experimentation is required to compare the uptake of SNU539 with different cell lines that do not express SAS1B.

5.2.3.1 DOTA-[^{67}Cu] Biodistribution

Biodistribution of radioactivity data in each organ was collected with high radioactivity after one hour in kidney, spleen, liver, and lung. It also showed rapid clearance of [^{67}Cu]-DOTA from kidney after 6 hours while slow in blood, liver, and spleen (Figure 30). There was no uptake of [^{67}Cu]-DOTA by the brain and less uptake in bones and muscles.

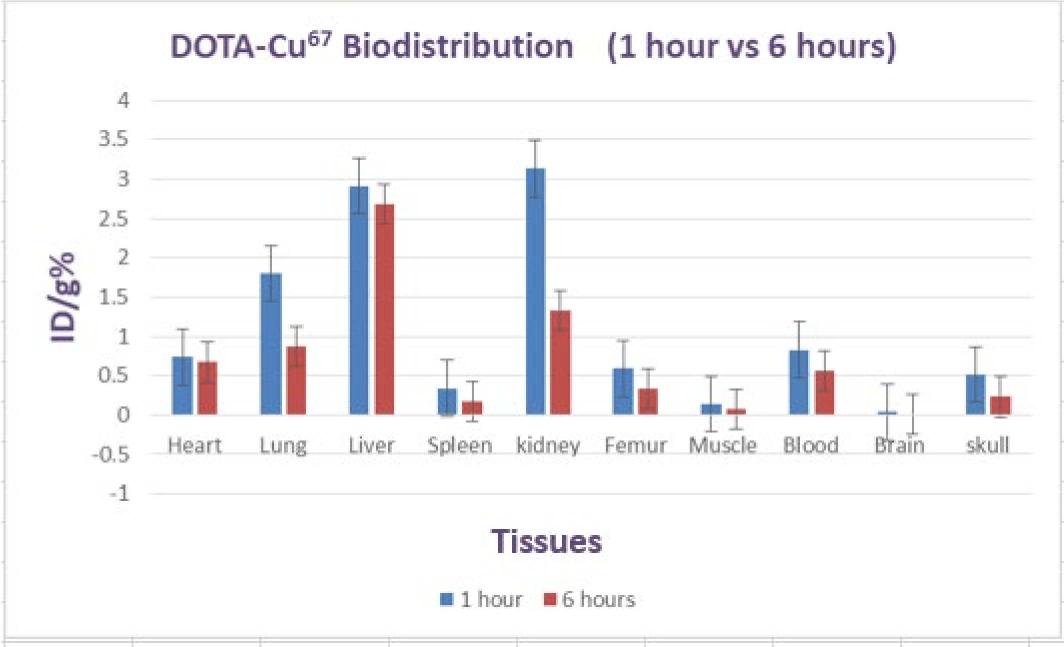

Figure 30. Gamma counter results show the uptake of [^{67}Cu]-DOTA in different body organs after 1 hour and 6 hours.

5.2.3.2 Copper 67 (^{67}CuCl$_2$) Biodistribution

As seen in results of ^{67}CuCl$_2$ Biodistribution shown in Figure 31, most of the ^{67}Cu activity was cleared by kidney after 6 hours and the activity in urine sample supports that too. Also, almost no uptake by the brain and less uptake in the bone. Liver, heart, and blood still showing activity after 6 hours. This indicates that some of the ^{67}Cu might bind to some of blood proteins and is still circulating in the blood.

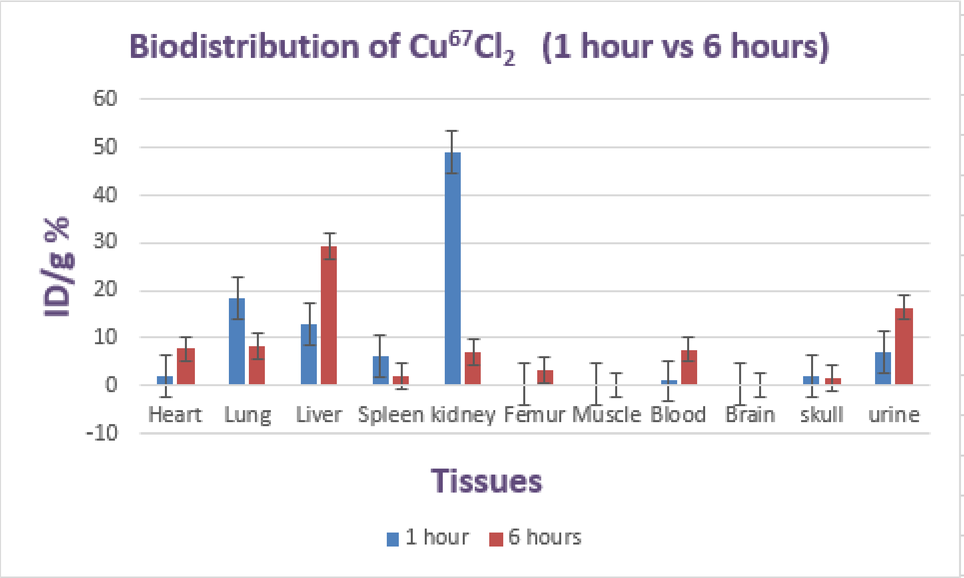

Figure 31. *In vivo* Copper67 ($^{67}CuCl_2$) Biodistribution. Results showed rapid clearance of $^{67}CuCl_2$ from kidney, lung, spleen and urine after 6 hours, while still more uptake in blood, heart and liver after 6 hours compared to 1hour uptake.

5.2.4 Discussion

Optimization of antibody to chelator was performed first for SB2 with DOTA to maximize conjugation yield and radiolabeling to obtain high radiochemical yield [156] [157]. For SB2-DOTA conjugation, two parameters were studied, the molar ratio of mAb to chelator/linker and the time of conjugation reaction. Three different ratios, 1:3, 1:5, and 1:10, were investigated for conjugation yield using HPLC at different times of conjugation reaction. The molar ratios (antibody: Chelator) of 1:3 and 1:5 were found to yield optimum conjugations after reacting the chelate and antibody for 24 hours at 37°C.

The molar ratios of 1:3 and 1:5 were adopted for subsequent radiolabeling experiments. Anti-SAS1B antibody SB2 was radiolabeled with different levels radioactivity of ^{67}Cu radionuclide. There was less uptake of [^{67}Cu]-DOTA and free $^{67}CuCl_2$ in SNU539 cells than that of the radiolabeled antibody SB2-DOTA-[^{67}Cu] t-test =0.0108 and 0.0039, indicating that at least part of the higher uptake of the radiolabeled SB2 is due to binding of SB2 antibody to its SAS1B target. Correlation between radiolabeled uptake and SAS1B expression would be useful to show binding specificity.

The biodistribution of both [^{67}Cu]-DOTA and free [^{67}Cu]-Cl_2 were also determined. Compared to antibody, these are small molecules and are cleared rapidly from the blood with subsequent clearance by kidney and, to some extent, by hepatobiliary excretion. This could be due to the slow [^{67}Cu]-DOTA metabolism in liver [158].

Free ^{67}Cu biodistribution also showed fast clearance by the kidneys after 6 hours, which is matched by corresponding activity in the urine. Activity in the liver is indicative of copper metabolism in the liver and also binding to cerepruplasmin, a copper binding protein [159]. Further experiments with different cells lines do not express SAS1B surface antigen is required to investigate the significance of radiolabeled SB2 targeting SNU539 cells. As mentioned before, there are many factors contributing to cell uptake and competeting the binding of antibody to target antigen. These include, linking the chelator to antibody and the effect of radiation on the nature of the antibody when it’s labeled with radionuclides.

Ex vivo preliminary experiments were done before *in vivo* imaging to reveal organ-based uptake. These also help to guide the *in vivo* experiments.

5.3 Labeling SB2 with NIRdye800CW

Near infra-red dye800CW was used to label antiSAS1B SB2 or *in vitro* experiments. Therefore, optimizing of antibody to dye (SB2-IR800CW) conjugation was done first to determine the optimal ratio of conjugation. Then, the optimal conjugation ratio of SB2-to-IR800CW was used for in vitro work.

5.3.1 SB2-IRdye800CW Conjugation.

Anti-SAS1B (SB2) was conjugated to IR800CW in different molar ratios 1:1, 1:2 and 1:3 and analyzed using UV/Vis systems. Absorptions and emissions of SB2-IR800CW were determined (Figure 32A). The absorption and emission spectra of SB2-IRD800CW matches the absorption and emission spectra of IR800CW dye from Licor (Figure32B). Figure 33 shows the absorption of SB2-IR800CW ratio 1:3. The absorption of SB2-IR800CW increases about two-fold from ratio 1:1 to 1:2, whereas, the molar ratio 1:3 of SB2-IR800CW increased to one-fold from ratio 1:2 (Figure 34).

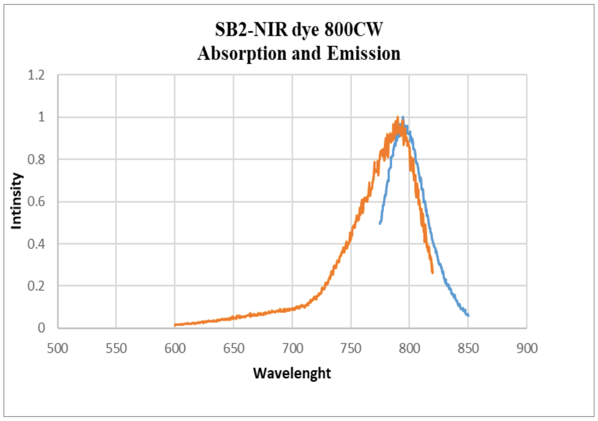

Figure 32-A. Absorption
and emission spectra of SB2 labeled
with NIRDye800CW

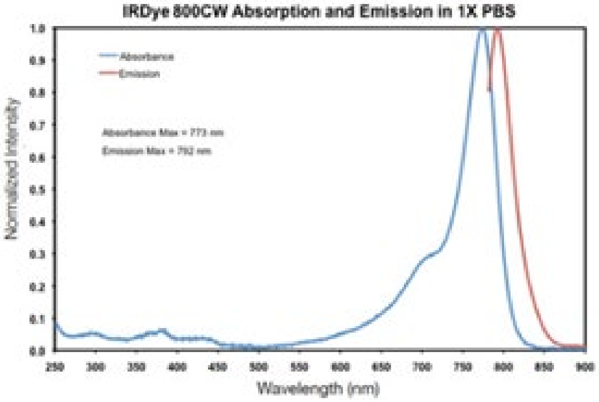

Figure 32 B-. Spectra of NIRDye 800C
provided by LICOR

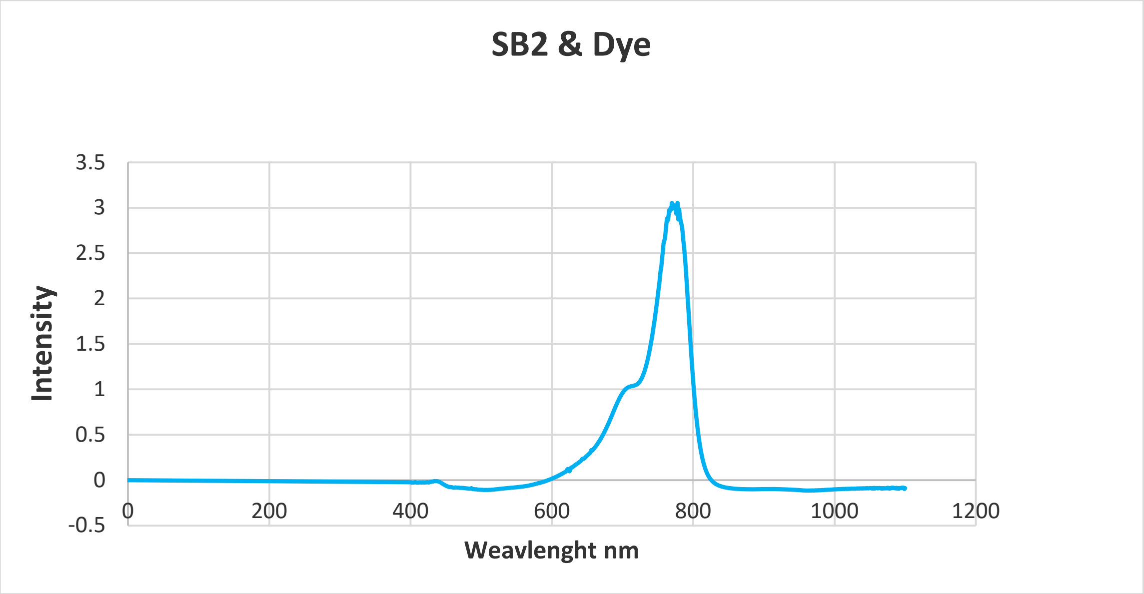

Figure 33. SB2&IR800CW 1:3 ratio absorption measured usung UV/Vis system.

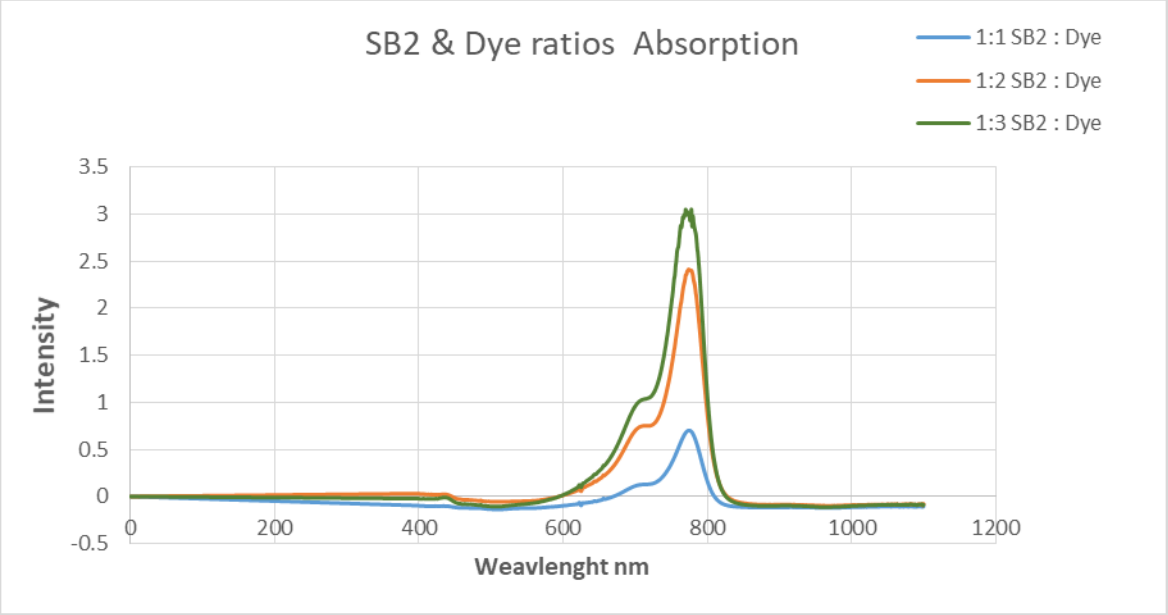

Figure 34. UV/Vis results of different SB2 & Dye ratios.

5.3.2 Conjugation Stability

Stabilty of SB2 &IRDye 800CW conjugations in different ratios and the unconjugated dye IRdye800CW were monitored for a period of 5 days using UV/Vis spectrophotometer. There was steady slight dercreasing of fluorescent signal over time for both SB2&dye and the unconjugated dye (Figure 35) . The conjugated SB2 was stored at 4°C with protection from the light during this time.

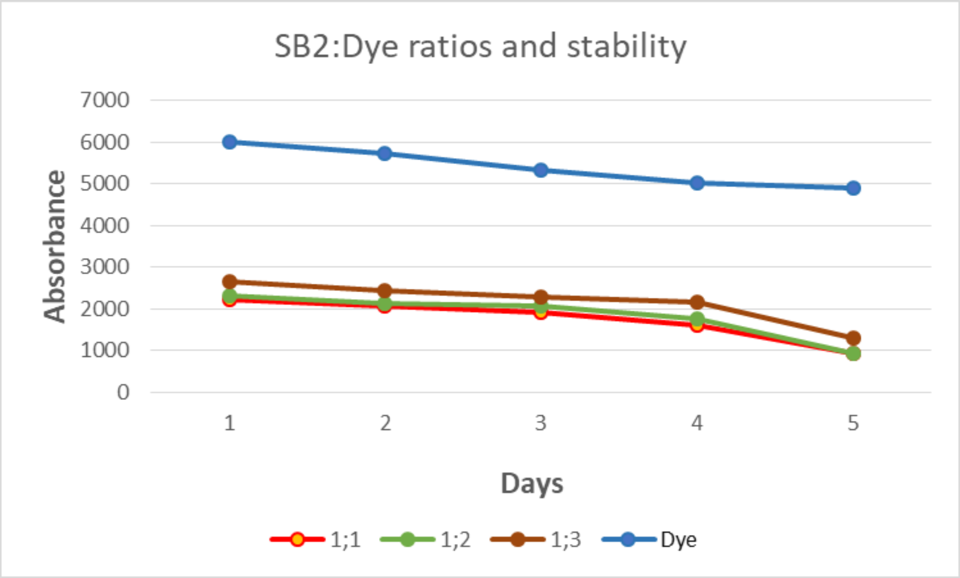

Figure 35. Antibody SB2 -IR800CW stabilty. Absorbances of three ratios of SB2-IR800CW (1:1, 1:2 : 1:3) and unconjugated dye 800CW for 5 days.

5.3.3 Cell Binding

Three different cell lines were grown in two 6-well culture plates. Two of these cell lines were SNU539 and SKOV3 which express SAS1B surface antigen and the other one is A549 cell lines (lung cell lines) which does not express SAS1B. These cells were incubated with SB2 labeled with IR800CW in one 6-well plates for one hour at 37°C and the same type of cells in another 6-well plates were incubated with nonspesfic antibody IgG labeled with IR800CWfor one as negative control. This followed by washing the cells with saline to remove any unbinded labeled SB2, IgG or dye.These cells were examined using fluoresence microscpe (Figure 36).

Near infra-red dye signals were seen in SNU539 and SKOV3 cell lines which incubated with SB2-IR800CW while no signal was seen from A549 cells. Also, there were no fluorsence signals when the cells incubated with IgG-IR800CW. This illistrated that there was binding of SB2-IR800CW with SAS1B surface antgen expresed by SNU539 and SK-OV3.

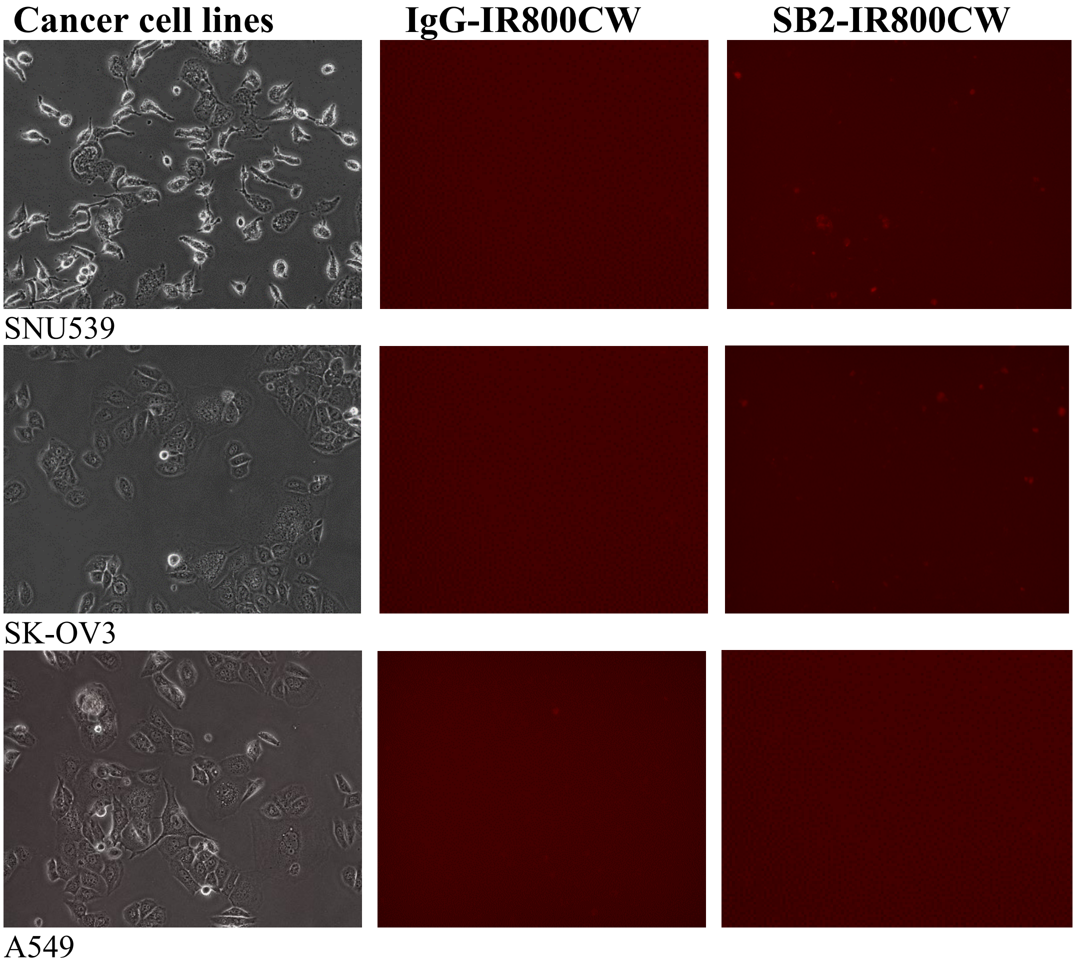

Figure 36.Three different cells, SNU539 uterine cancer cells, SK-OV3 ovarian cancer cell, and A549 lung cancer cell. These cells were treated with SB2 labeled with IR800CW and IgG labeled with IR800CW. Both SNU539 and SK-OV are expressing SAS1B but A549 does not express SAS1B. Therefore, there is uptake of SB2-IR00CW for both SNU539 and SK-OV cell lines,

5.3.4 Discussion

Near-infrared dye was chosen as an alternative to radioactive agents to labeled anti-SAS1B (SB2) as an image guide for tumor localization and Biodistribution study. Near infra-red dye 800CW-NHS ester was prepared according to good manufacturing guidelines [160]. Optimization of antiSAS1B SB2 with IRDye800CW-NHS ester conjugation was performed to obtain the optimal ratio that could be used *in vitro* and *in vivo* and determine high fluoresce signal less background noise, decrease the effect of antibody-antigen binding, and reduce dye toxicity due to the excess of dye [161]. Optimization of SB2-IR800CW was done by reacting different molar ratios (antibody: Dye) 1:1, 1:2 and 1:3 in phosphate –buffered saline (PBS, pH 8.3) solution. The results of UV/Vis analyzer showed the ratio 1:2 of SB2 to dye conjugation represent a good signal with less detachment of dye to antibody because when the ratio was increased to 1:3, the intensity increased just to one-fold by comparing the intensities of 1:1 and 1:2 ratios. The ratio 1:2 of conjugation was used for *in vitro* and *in vivo* studies.

In vitro study was done by determining the fluorescence signals which were produced after incubating SB2-IR800CW with SNU539 and SK-OV3 cell lines which are expressing SAS1B and compared to fluorescence signals produced when incubating the same cell lines with nonspecific antibody IgG labeled with IR800CW. Additionally, different cell lines A549 (cancer cell lines) were incubated with SB2-IR800CW and IgG-IR800CW. Fluorescence signals were determined using fluorescence microscope and the results showed some signals were produced from SNU539 and SK-OV3 cells that were incubated with SB2-IR800CW. There were no signals from the same types of cells incubated with IgG-IR800CW. Moreover, there was no fluorescence signal produced by A549 cell lines. This confirms that there was specific binding of SB2-IR800CW to SAS1B surface antigen on SNU539 and SK-OV3 cell lines.

CHAPTER 6: OVERALL DISSCUSSION

6.1 Radiolabeling of SB2/5 with ^{89}Zr

In this work, two of anti-SAS1B (SB5 and SB2) were radiolabeled with ^{89}Zr and ^{67}Cu respectfully. Anti-SAS1B SB2 was also labeled with near-infrared dye 800CW. The labeling of SB5 and SB2 was performed to investigate the *in vitro* and *in vivo* binding of both anti-SAS1B to uterine cancer surface antigen SAS1B. The over-expression of SAS1B in several types of cancer cells, including uterine was a novel discovery by the University of Virginia and is an opportunity for tumor receptor imaging which could guide and improve cancer detection and treatment. Labeling with ^{89}Zr was preformed based on a substantial number of studies showing promising PET imaging with ^{89}Zr labeling [162], in addition to ^{89}Zr was available at VCU hospital. ^{89}Zr physical and chemical properties are attractive, such as 78.8 hours of half-life which matches antibodies' half-lives. Also, ^{89}Zr was classified as a hard cation that binds strongly to the chelator through six hard, anionic oxygen donors of Desferrioxamine (DFO) [83]. DFO chelator was chosen as a linker between SB5 and ^{89}Zr because it is the preferred chelator for ^{89}Zr labeling and it binds to antibodies through the lysine amino acid residues which are available with about 80% on antibodies.

6.2 SB5-DFO Conjugation

In order to label SB5 with ^{89}Zr, firstly SB5-DFO conjugate was optimized through many reactions with different reaction variables. The optimized conjugation was described in the Methods chapter. The conjugation yield of optimized reaction was more than 85%. Conjugation of SB5 with DFO was evaluated using HPLC through a size exclusion column where the qualitative and quantitative yields of conjugation can be determined. This conjugation yield was encouraging compared with other studies for ^{89}Zr labeling antibodies. Optimization of antibody conjugation with chelators takes time because of a number of factors affecting reaction yield and stability. Therefore, radioactive isotope could not be ordered unless good optimization was performed because of the decay of radioactive isotope and it is also expense.

6.3 ^{89}Zr-DFO-SB5

Once the conjugations of SB5 with DFO were optimized, ^{89}Zr was ordered for labeling SB5-DFO. Different labeling reactions were performed and the optimized procedures resulted in an average yield of 67±8%. Other studies with ^{89}Zr-DFO antibody labeling reported similar yield after purifications [163] . The results of HPLC chromatograph showed some fragmentation of SB2. This might be the effect of radioactivity of ^{89}Zr, and needs to be investigated. In order to remove all unwanted labeling, the reaction was purified using a size exclusion column PD10. The purified fractions were analyzed using radio-TLC, and the highest yield of labeling was used for *in vitro* and in *vivo* work.

6.4 SB2 DOTA Conjugation and [^{67}Cu]-DOTA-SB2

Optimizing the conjugation of SB2 with DOTA was performed first. Different ratios of SB2-DOTA were investigated in different conditions of incubation temperature, speed of shaking, and reaction time. The ratios 1:3 and 1:5 showed about 100% of conjugation yield using an HPLC-size exclusion column. This reaction was incubated at 37C for 24 hours. This conjugation of SB2-DOTA was monitored for one week and was stable at 4C. The conjugated SB2-DOTA with 1:5 molar ratio was labeled with ^{67}Cu, in chloride form buffered solution (pH=4-5). Radiolabeling yield reached 85% and following PD10 purification, a radiochemical purity of more than 95% was achieved. This is comparable to other ^{67}Cu DOTA-Mab studies (refs).

6.5 Evaluation of radiolabeled SB2 and SB5 in cells expressing SAS1B

All *in vitro* experiments were done to investigate the binding of SB5-DFO-[^{89}Zr], SB2-DOTA- [^{67}Cu] and labeled SB2 with NIR dye 800CW to SAS1B uterine cancer cell surface antigen. All results showed the specific binding of labeled anti-SAS1B antibodies to its target SAS1B. SNU539 cells in different numbers were incubated with labeling SB5with ^{89}Zr for 2 hours and then washed to remove any unbinding species. The radioactivity associated with cells was measured and the results show the radioactivity increased when the cell number of SNU539 was increased. This indicates the binding of radiolabeled SB5 to expressed SAS1B on SNU539 cells.

While the in vitro work of radiolabeled SB2 with ^{67}Cu, SB2 was labeled with 4uCi of ^{67}Cu and incubated with SNU539 and SK-OV3 and similar radioactivity of ^{67}Cucl$_2$ and DOTA-[^{67}Cu] were also incubated with SNU539 cell line. After washing all cells, the radioactivity measures showed high uptake of SB2-DOTA-[^{67}Cu] for both SNU539 and SK-OV3 cells compared to the uptake of ^{67}Cu and DOTA-[^{67}Cu] ***p* value <0.05**. Both SNU539 and Sk-OV3 cell line express SAS1B which indicate the specific binding of radiolabeled SB2 to SAS1B.

6.7 *In Vivo* imaging and Biodistribution.

After confirming the specific binding of labeled anti-SAS1B antibodies to its target SAS1B, *in vivo* and *ex vivo* work were done to determine tumor uptake and biodistribution. The *in vivo* experiments include culturing cell lines, monitoring cell growth, assessing cell viability, and the cell were harvested and inoculated subcutaneously into the mice flanks to implement a tumor. All these steps took about 3 months because of the slow growth of SNU539 cell line. When tumor animal model was prepared for [^{89}Zr]-DFO-SB5 experiments, [^{89}Zr]-DFO-SB5 was injected in a female mouse bearing tumor and the PET images of the mouse were taken at different periods of time. The results showed different levels of [^{89}Zr]-DFO-SB5 radioactivity accumulated in different body organs. More uptake was shown in bone, liver, and spleen after 72 hours while less uptake by the tumor. Also, more bone uptake of ^{89}Zr was reported in a number of studies [153]. In addition, high radioactivity can affect the immunoreactivity. The HPLC chromatogram results also showed small peaks which might be SB5 fragments due to the effects of radioactivity of ^{89}Zr. The *ex vivo* results illustrated the biodistribution of radioactivity in each organ. The *ex vivo* results were similar the PET scan results, less uptake by the tumor compared to other organs. In addition, high levels of radioactivity were determined in the bone, spleen, and liver. Radioactivity of [^{89}Zr]-DFO-SB5 toward SAS1B expressed by uterine tumor was noticeable compared with the uptake of nonspecific antibody [^{89}Zr]-DFO-3A4.

It is important to know the accumulation profile of radiolabeled components that make up the radio-conjugate, such as $^{67}CuCl_2$ and [^{67}Cu]-DOTA. In this regard, ex vivo experiments using ^{67}Cu were performed to study the biodistribution of $^{67}CuCl_2$ and [^{67}Cu]-DOTA in animals. In this experiment, two groups of mice were used.One group was injected with ^{67}Cu only and the other group was injected with [^{67}Cu]-DOTA. In triplicate mice were sacrificed at different time points and organs were collected. The radioactivity of each organ was determined after normalizing all date. Biodistribution results showed rapid clearing of both ^{67}Cu and [^{67}Cu]-DOTA after 6 hours, except in the liver which slowed accumulation and slow clearance of ^{67}Cu and [^{67}Cu]-DOTA. This could be due to cooper interaction and metabolism in the liver.

6.8 Fluorescence microscopy of SB2 labeled with near-infrared dye 800CW

Near-infrared dye was used as alternative to radiolabeling. In this work, SB2 was labeled with the dye in different ratio (1:1, 1:2 and 1:3). This was done to determine the labeling yield of different molar ratios. Results showed the increases for fluorescent signal to about 2 folds from ratio 1:1 to 1:2.and and 1 fold from ratio 1:2 to 1:3. This could be related to the saturation of binding of dye to lysine residues on the antibody[164]. The stability of all ratios of labeled SB2 to dye was monitored using UV/Vis analyzer for 5 days and compared to the stability of the dye only. The results showed that the fluorescent signals are decreasing slowly with the time. The molar ratio 1:3 of SB2 to dye was used for *in vitro* work to determine the binding of non-radioactive labeled SB2 to SAS1B. Different cell lines SNU539, SK-OV3 and A549 were grown and incubated with SB2-INRdye 800CW. Fluorescent signals were determined on SNU539 and SK-OV3 cells while no signals on A549. These fluorescent signals indicate the binding of SB2 to SAS1B on SNU539 and SK-OV3 due to the overexpression of SAS1B on these cell as reported in the UVA studies. The lung cells A549 were used as negative control and there were no fluorescent signals determined on these cells. Near-infrared labeling of SB2 confirms the specific binding of SB2 to its target SAS1B and the results are encouraging for *in vivo* study of imaging uterine tumor and biodistribution in mouse model. With this fluorescence labeling version of monoclonal, it is a useful additional complementary tool to radiotracer analysis.

CHAPTER 7: CONCLUSION AND FUTURE WORK

7.1 Summary

Radiolabeling anti-SAS1B antibodies with ^{89}Zr, ^{67}Cu and near-infrared dye 800CW have been synthesized to enable molecular imaging of the radiolabeled conjugates in uterine cancer xenografts expressing the cell surface antigen SAS1B.

Optimizing the conjugation of the chelators of radioactive isotopes with anti-SAS1B (SB2 and SB5) and SB2 with near-infrared was performed using low scale of activity. HPLC with size exclusion chromatography was used to determine the conjugation yield and radiochemical purity. Radiolabeled yields of SB5 and SB2 were determined using radio-TLC analysis and then purified using size exclusion column PD10. Labeling SB2 with near-infrared dye was determined by UV/VIS fluorescence microscopy. *In vitro* study confirmed the specific binding of SB2 and SB5 to SAS1B receptor on uterine cancer cell lines SNU539.

In vivo PET imaging of ^{89}Zr-radiolabeled SB5, in tumor-bearing nude mice, showed some radioactivity in the tumor, indicative of preferential accumulation, presumably due to affinity of radiolabeled SB5 toSAS1B present on surface of tumor cells. However, conformation of binding specificity needs to be assessed by relating radiolabeled SB5 uptake to level of SAS1B present on the same tumor. Significant uptake was also observed in bone, a phenomenon that has been reported in the literature of ^{89}Zr-immunoPET imaging [165]. The explanation for bone accumulation is probably due to detachment of the radioisotope from its DFO cage and as zirconium has affinity for the phosphonate lattice, it accumulates in bone. Chelators other than DFO are being developed in an attempt to reduce *in vivo* instability, for example the linker HOPO [166].

Preliminary *in vitro* experiments of radiolabeled SB2 with ^{67}Cu demonstrated the specific uptake of both the uterine cancer cell line SNU539 and ovarian cancer cell line SK-OV3 because both cell lines express SAS1B. The use of [^{67}Cu]-DOTA SB2 for future in vivo studies may provide a better pharmacokinetic profile than that of [^{89}Zr]-radiolabeled antibody. Successfully labeled SB2 with the NIR dye 800CW could also be used in validation experiments as it was established that this optical probe showed uptake of both cells SNU539 and SK-OV3 which express SAS1B compared to a negative control, the lung cancer cell line A549 which does express SAS1B.

7.2 Future work

Future work should build on the progress made in the development of radio-immuno-conjugates and pursue three future aims:

1. Further optimize $[^{64/67}Cu]$-SB2/5 conjugation and investigate its stability, particularly in vivo, by performing radio-HPLC analysis on homogenized tissues, including tumors.
2. Determine the amount of SAS1B in tumor sections by protein assay, and assess how this protein level is related to uptake of radiolabeled antibody in the same tumor slice.

APPENDIX

Presentations and Manuscripts

Nouri Elmekharam, Sundaresan Gobalakrishnan, Huseyin.Cicek, Ali Gawi, Li Wang, Celina Thadigiri , Jamal Zweit,“**Radioimmunoconjugate for cancer molecular imaging**”
(In preparation).

Nouri Elmekharam, Sundaresan Gobalakrishnan, Ali Gawi, Jamal Zweit,
“**Copper-67 labeled anti-SAS1B for binding to uterine cancer cell surface antigen**”
(In preparation)

Nouri Elmekharam, Sundaresan Gobalakrishnan, Minghao Sun, Celina Thadigiri, Li Wang, Nicholas P. Farrell, Jamal Zweit, “**Image-Guided Radioimmuno-Therapy of Cancer**”
2016, 2018and 2019**,** posters presentation. Department of chemistry, Chemical biology, Center for Molecular Imaging, Department of Radiology, Virginia Commonwealth University, Richmond, VA

Nouri Elmekharam, “**Image-Guided Cancer immunotherapy**” literature presentation, 2017, Department of chemistry. Chemical biology, Center for Molecular Imaging, Department of Radiology, Virginia Commonwealth University, Richmond, VA

Nouri Elmekharam, Sundaresan Gobalakrishnan, Huseyin.Cicek, Ali Gawi, Li Wang , Celina Thadigiri, Jamal Zweit,“**Image Guided-Radioimmunotherapy**” oral presentation at International Conference on Advancements in Cancer Detection and Radiology **ICACDR, March 11-12, 2021**.

References

[1] S. J. H. Waaijer *et al.*, “Molecular Imaging in Cancer Drug Development,” vol. 59, no. 5, pp. 726–732, 2018, doi: 10.2967/jnumed.116.188045.

[2] R. L. Siegel, K. D. Miller, H. E. Fuchs, and A. Jemal, “Cancer Statistics , 2021,” doi: 10.3322/caac.21654.

[3] G. Lyratzopoulos, P. Vedsted, and H. Singh, “Understanding missed opportunities for more timely diagnosis of cancer in symptomatic patients after presentation,” vol. 112, no. s1, pp. S84–S91, 2015, doi: 10.1038/bjc.2015.47.

[4] S. Elmore, “Apoptosis: A Review of Programmed Cell Death,” *Toxicol Pathol*, vol. 35, no. 4, pp. 495–516, 2007.

[5] M. R. Stratton, P. J. Campbell, and P. A. Futreal, “Europe PMC Funders Group,” vol. 458, no. 7239, pp. 719–724, 2010, doi: 10.1038/nature07943.

[6] M. J. Markham *et al.*, “Clinical Cancer Advances 2020: Annual report on progress against cancer from the American Society of Clinical oncology,” *J. Clin. Oncol.*, vol. 38, no. 10, pp. 1081–1101, 2020, doi: 10.1200/JCO.19.03141.

[7] L. Fass, “Imaging and cancer : A review,” vol. 2, pp. 115–152, 2008, doi: 10.1016/j.molonc.2008.04.001.

[8] J. T. Loud and J. Murphy, “Cancer Screening and Early Detection in the 21st Century,” *Semin. Oncol. Nurs.*, vol. 33, no. 2, pp. 121–128, 2017, doi: 10.1016/j.soncn.2017.02.002.

[9] T. Porta Siegel, G. Hamm, J. Bunch, J. Cappell, J. S. Fletcher, and K. Schwamborn, “Mass Spectrometry Imaging and Integration with Other Imaging Modalities for Greater Molecular Understanding of Biological Tissues,” *Mol. Imaging Biol.*, vol. 20, no. 6, pp. 888–901, 2018, doi: 10.1007/s11307-018-1267-y.

[10] A. Gallamini, C. Zwarthoed, and A. Borra, “Positron Emission Tomography (PET) in Oncology,” pp. 1821–1889, 2014, doi: 10.3390/cancers6041821.

[11] R. Fusco, V. Granata, and A. Petrillo, “Introduction to special issue of radiology and imaging of cancer,” *Cancers (Basel).*, vol. 12, no. 9, pp. 1–4, 2020, doi: 10.3390/cancers12092665.

[12] S. U. Dalm, J. F. Verzijlbergen, and M. De Jong, “Review: Receptor targeted nuclear imaging of breast cancer,” *Int. J. Mol. Sci.*, vol. 18, no. 2, 2017, doi: 10.3390/ijms18020260.

[13] C. Pucci, “Innovative approaches for cancer treatment : current perspectives and new challenges,” pp. 1–26, 2019.

[14] Q. Shi *et al.*, “Survival analysis of patients with advanced non-small cell lung cancer receiving tyrosine kinase inhibitor (TKI) treatment: A multi-center retrospective study,” *Thorac. Cancer*, vol. 9, no. 2, pp. 278–283, 2018, doi: 10.1111/1759-7714.12577.

[15] H. H. W. Chen and M. T. Kuo, “Improving radiotherapy in cancer treatment: Promises and challenges,” *Oncotarget*, vol. 8, no. 37, pp. 62742–62758, 2017, doi: 10.18632/oncotarget.18409.

[16] E. Numbers and C. Survivors, “Cancer Treatment & Survivorship,” 2021.

[17] R. B. Mokhtari *et al.*, “Combination therapy in combating cancer SYSTEMATIC REVIEW: COMBINATION THERAPY IN COMBATING CANCER BACKGROUND,” *Oncotarget*, vol. 8, no. 23, pp. 38022–38043, 2017.

[18] K. Nawab, D. Bhere, A. Bommarito, M. Mufti, and A. Naeem, “Stem Cell Therapies: A Way to Promising Cures,” *Cureus*, vol. 11, no. 9, 2019, doi: 10.7759/cureus.5712.

[19] D. Cross and J. K. Burmester, “Gene therapy for cancer treatment: Past, present and future,” *Clin. Med. Res.*, vol. 4, no. 3, pp. 218–227, 2006, doi: 10.3121/cmr.4.3.218.

[20] S. Farkona, E. P. Diamandis, and I. M. Blasutig, “Cancer immunotherapy: The beginning of the end of cancer?,” *BMC Med.*, vol. 14, no. 1, pp. 1–18, 2016, doi: 10.1186/s12916-016-0623-5.

[21] M. Arruebo, N. Vilaboa, B. Sáez-gutierrez, and J. Lambea, “Assessment of the Evolution of Cancer Treatment Therapies,” pp. 3279–3330, 2011, doi: 10.3390/cancers3033279.

[22] P. E. Young *et al.*, “Early detection of colorectal cancer recurrence in patients undergoing surgery with curative intent: Current status and challenges,” *J. Cancer*, vol. 5, no. 4, pp. 262–271, 2014, doi: 10.7150/jca.7988.

[23] I. Jatoi *et al.*, “The role of surgery in cancer prevention,” *Curr. Probl. Surg.*, vol. 47, no. 10, pp. 750–830, 2010, doi: 10.1067/j.cpsurg.2010.06.002.

[24] R. Alaofi, M. Nassif, and M. Al-Hajeili, “Prophylactic mastectomy for the prevention of breast cancer: Review of the literature,” *Avicenna J. Med.*, vol. 8, no. 3, p. 67, 2018, doi: 10.4103/ajm.ajm_21_18.

[25] M. Adham and J. Perinel, “Palliative therapy in pancreatic cancer—palliative surgery,” *Transl. Gastroenterol. Hepatol.*, vol. 4, no. May, pp. 1–8, 2019, doi: 10.21037/tgh.2019.04.03.

[26] V. T. DeVita and E. Chu, “A history of cancer chemotherapy,” *Cancer Res.*, vol. 68, no. 21, pp. 8643–8653, 2008, doi: 10.1158/0008-5472.CAN-07-6611.

[27] A. Alam, “Chemotherapy Treatment and Strategy Schemes: A Review,” *Open Access J. Toxicol.*, vol. 2, no. 5, 2018, doi: 10.19080/oajt.2018.02.555600.

[28] R. Ralhan and J. Kaur, “Alkylating agents and cancer therapy,” *Expert Opin. Ther. Pat.*, vol. 17, no. 9, pp. 1061–1075, 2007, doi: 10.1517/13543776.17.9.1061.

[29] L. H. Swift and R. M. Golsteyn, “Genotoxic anti-cancer agents and their relationship to DNA damage, mitosis, and checkpoint adaptation in proliferating cancer cells,” *Int. J. Mol. Sci.*, vol. 15, no. 3, pp. 3403–3431, 2014, doi: 10.3390/ijms15033403.

[30] M. Mehrmohamadi, S. H. Jeong, and J. W. Locasale, “Molecular features that predict the response to antimetabolite chemotherapies,” *Cancer Metab.*, vol. 5, no. 1, pp. 1–13, 2017, doi: 10.1186/s40170-017-0170-3.

[31] A. Desai *et al.*, “Medicinal Plants and Cancer Chemoprevention,” *Curr. Drug Metab.*, vol. 9, no. 7, pp. 581–591, 2008, doi: 10.2174/138920008785821657.

[32] U. Galm, M. H. Hager, S. G. Van Lanen, J. Ju, J. S. Thorson, and B. Shen, “Antitumor antibiotics: Bleomycin, enediynes, and mitomycin,” *Chem. Rev.*, vol. 105, no. 2, pp. 739–758, 2005, doi: 10.1021/cr030117g.

[33] R. M. McQuade, V. Stojanovska, R. Abalo, J. C. Bornstein, and K. Nurgali, “Chemotherapy-induced constipation and diarrhea: Pathophysiology, current and emerging treatments,” *Front. Pharmacol.*, vol. 7, no. NOV, pp. 1–14, 2016, doi: 10.3389/fphar.2016.00414.

[34] Y. Wang, V. Probin, and D. Zhou, “Cancer Therapy-Induced Residual Bone Marrow Injury: Mechanisms of Induction and Implication for Therapy,” *Curr. Cancer Ther. Rev.*, vol. 2, no. 3, pp. 271–279, 2006, doi: 10.2174/157339406777934717.

[35] R. B. Rome, H. H. Luminais, D. A. Bourgeois, and C. M. Blais, “The Role of Palliative Care at the End of Life,” pp. 348–352, 2011.

[36] R. Baskar, K. A. Lee, R. Yeo, and K. Yeoh, “Cancer and Radiation Therapy : Current Advances and Future Directions,” 2012, doi: 10.7150/ijms.3635.

[37] R. Baskar, J. Dai, N. Wenlong, R. Yeo, K. Yeoh, and B. Rogers, “Biological response of cancer cells to radiation treatment,” vol. 1, no. November, pp. 1–9, 2014, doi: 10.3389/fmolb.2014.00024.

[38] A. I. Kassis and S. J. Adelstein, “Radiobiologic Principles in Radionuclide Therapy,” vol. 46, no. 1, pp. 4–12, 2005.

[39] K. Sano, Y. Kanada, K. Kanazaki, N. Ding, M. Ono, and H. Saji, “B 1380,” vol. 58, no. 9, pp. 1380–1385, 2017, doi: 10.2967/jnumed.117.189993.

[40] S. Heskamp *et al.*, “a - Versus b -Emitting Radionuclides for Pretargeted Radioimmunotherapy of Carcinoembryonic Antigen– Expressing Human Colon Cancer Xenografts,” vol. 58, no. 6, pp. 926–933, 2017, doi: 10.2967/jnumed.116.187021.

[41] M. Cristina, N. P. Van Der Meulen, and M. Bene ̌, “Therapeutic Radiometals Beyond 177 Lu and 90 Y: Production and Application of Promising a -Particle, b 2 -Particle, and Auger Electron Emitters,” pp. 91–96, 2017, doi: 10.2967/jnumed.116.186825.

[42] R. Baskar, S. P. Yap, K. Lee, M. Chua, and K. Itahana, “The diverse and complex roles of radiation on cancer treatment : therapeutic target and genome maintenance,” vol. 2, no. 4, pp. 372–382, 2012.

[43] I. F. Tannock, “Conventional cancer therapy: Promise broken or promise delayed?,” *Lancet*, vol. 351, no. SUPPL.2, 1998, doi: 10.1016/S0140-6736(98)90327-0.

[44] E. J. Devlin, L. A. Denson, and H. S. Whitford, “Cancer Treatment Side Effects: A Meta-analysis of the Relationship Between Response Expectancies and Experience,” *J. Pain Symptom Manage.*, vol. 54, no. 2, pp. 245-258.e2, 2017, doi: 10.1016/j.jpainsymman.2017.03.017.

[45] A. Luengo, D. Y. Gui, and M. G. Vander Heiden, “HHS Public Access,” vol. 24, no. 9, pp. 1161–1180, 2018, doi: 10.1016/j.chembiol.2017.08.028.Targeting.

[46] G. M. Wilkes, “Targeted Therapy : Attacking Cancer with Molecular and Immunological Targeted Agents,” pp. 137–155, 2018, doi: 10.4103/apjon.apjon.

[47] T. Art, “Biologic Therapy,” no. 5, pp. 301–313, 2012, doi: 10.1097/NAN.0b013e31826579.

[48] S. Dl, D. Zob, A. Lazescu, R. Bunghez, and R. Anghel, “Development of new immunotherapy treatments in different cancer types,” vol. 9, no. 3, pp. 240–248, 2016.

[49] N. Taefehshokr, B. Baradaran, A. Baghbanzadeh, and S. Taefehshokr, “Promising approaches in cancer immunotherapy,” *Immunobiology*, no. November, p. 151875, 2019, doi: 10.1016/j.imbio.2019.11.010.

[50] A. H. Kverneland *et al.*, “Adoptive cell therapy in combination with checkpoint inhibitors in ovarian cancer,” vol. 11, no. 22, pp. 2092–2105, 2020.

[51] B. Melanoma, “Current Advances in the Treatment of BRAF-Mutant Melanoma,” pp. 15–20, 2020.

[52] H. Kaplon, M. Muralidharan, Z. Schneider, and J. M. Reichert, “Antibodies to watch in 2020,” *MAbs*, vol. 12, no. 1, 2020, doi: 10.1080/19420862.2019.1703531.

[53] M. T. Yilmaz, A. Elmali, and G. Yazici, “Abscopal Effect, From Myth to Reality: From Radiation Oncologists’ Perspective,” *Cureus*, vol. 11, no. 1, pp. 9–13, 2019, doi: 10.7759/cureus.3860.

[54] Y. Liu, Y. Dong, L. Kong, F. Shi, H. Zhu, and J. Yu, “Abscopal effect of radiotherapy combined with immune checkpoint inhibitors,” *J. Hematol. Oncol.*, vol. 11, no. 1, pp. 1–15, 2018, doi: 10.1186/s13045-018-0647-8.

[55] E. Bolli *et al.*, “Stromal-targeting radioimmunotherapy mitigates the progression of therapy-resistant tumors,” *J. Control. Release*, vol. 314, no. January, pp. 1–11, 2019, doi: 10.1016/j.jconrel.2019.10.024.

[56] J. Kang, S. Demaria, and S. Formenti, “Current clinical trials testing the combination of immunotherapy with radiotherapy,” *J. Immunother. Cancer*, 2016, doi: 10.1186/s40425-016-0156-7.

[57] K. Zakeri *et al.*, “Advancing Targeted Radionuclide Therapy through the National Cancer Institute ’ s Small Business Innovation Research Pathway,” pp. 1–22, 2018, doi: 10.2967/jnumed.118.214684.

[58] H. Kawashima, “Radioimmunotherapy : A Specific Treatment Protocol for Cancer by Cytotoxic Radioisotopes Conjugated to Antibodies,” vol. 2014, 2014, doi: 10.1155/2014/492061.

[59] J. A. Reisz, N. Bansal, J. Qian, W. Zhao, and C. M. Furdui, “Effects of Ionizing Radiation on Biological Molecules — Mechanisms of Damage and Emerging Methods of Detection,” vol. 21, no. 2, pp. 260–292, 2014, doi: 10.1089/ars.2013.5489.

[60] A. I. Kassis, “Therapeutic Radionuclides : Biophysical and Radiobiologic Principles,” no. October 2008, 2021, doi: 10.1053/j.semnuclmed.2008.05.002.

[61] J. Mihailović and T. Petrović, “Radioimmunotherapy : a novel treatment of non-Hodgkin lymphoma,” no. July 2010, 2014, doi: 10.2298/AOO1002023M.

[62] H. Desai, S. Borges-Neto, and T. Z. Wong, “Molecular Imaging and Therapy for Neuroendocrine Tumors,” *Curr. Treat. Options Oncol.*, vol. 20, no. 10, 2019, doi: 10.1007/s11864-019-0678-6.

[63] P. A. Erba *et al.*, “Radioimmunotherapy with radretumab in patients with relapsed hematologic malignancies,” *J. Nucl. Med.*, vol. 53, no. 6, pp. 922–927, 2012, doi: 10.2967/jnumed.111.101006.

[64] M. D. Bartholomä, “Radioimmunotherapy of solid tumors: Approaches on the verge of clinical application,” *J. Label. Compd. Radiopharm.*, vol. 61, no. 9, pp. 715–726, 2018, doi: 10.1002/jlcr.3619.

[65] R. Yudistiro, H. Hanaoka, N. Katsumata, A. Yamaguchi, and Y. Tsushima, “Bevacizumab Radioimmunotherapy (RIT) with Accelerated Blood Clearance Using the Avidin Chase,” *Mol. Pharm.*, vol. 15, no. 6, pp. 2165–2173, 2018, doi: 10.1021/acs.molpharmaceut.8b00027.

[66] P. Spang, C. Herrmann, and F. Roesch, “Bifunctional Gallium-68 Chelators: Past, Present, and Future,” *Semin. Nucl. Med.*, vol. 46, no. 5, pp. 373–394, 2016, doi: 10.1053/j.semnuclmed.2016.04.003.

[67] A. Catafau, *PET and SPECT in psychiatry*, vol. 17. 2002.

[68] J. Zweit, “Physics in Medicine & Biology Related content Radionuclides and carrier molecules for therapy Radionuclides and carrier molecules for therapy,” 1996 *Phys. Med. Biol.* **41** 1905.

[69] J. Clark and D. O. Hagan, “Strategies for radiolabelling antibody , antibody fragments and affibodies with fluorine-18 as tracers for positron emission tomography (PET),” *J. Fluor. Chem.*, vol. 203, no. June, pp. 31–46, 2017, doi: 10.1016/j.jfluchem.2017.08.001.

[70] B. M. Bavelaar, B. Q. Lee, M. R. Gill, N. Falzone, and K. A. Vallis, “Subcellular Targeting of Theranostic Radionuclides,” vol. 9, no. September, pp. 1–17, 2018, doi: 10.3389/fphar.2018.00996.

[71] O. O. Peltek, A. R. Muslimov, M. V. Zyuzin, and A. S. Timin, “Current outlook on radionuclide delivery systems: From design consideration to translation into clinics,” *J. Nanobiotechnology*, vol. 17, no. 1, pp. 1–34, 2019, doi: 10.1186/s12951-019-0524-9.

[72] A. I. Kassis, “Therapeutic Radionuclides : Biophysical and Radiobiologic Principles,” pp. 358–366, 2008, doi: 10.1053/j.semnuclmed.2008.05.002.

[73] C. D. Martins, G. Kramer-marek, W. J. G. Oyen, C. Daniel, G. Kramer-marek, and W. J. G. Oyen, “Expert Opinion on Drug Delivery Radioimmunotherapy for delivery of cytotoxic radioisotopes : current status and challenges,” *Expert Opin. Drug Deliv.*, vol. 15, no. 2, pp. 185–196, 2018, doi: 10.1080/17425247.2018.1378180.

[74] S. Aghevlian, A. J. Boyle, and R. M. Reilly, “Radioimmunotherapy of cancer with high linear energy transfer (LET) radiation delivered by radionuclides emitting α -particles or Auger electrons ☆,” *Adv. Drug Deliv. Rev.*, vol. 109, pp. 102–118, 2017, doi: 10.1016/j.addr.2015.12.003.

[75] R. F. Hospital and R. F. Hospital, “Targeted Alpha Particle Therapy for Neuroendocrine Tumours : The Next Generation of Peptide Receptor Radionuclide Therapy,” pp. 256–264, 2019, doi: 10.1159/000494760.

[76] M. J. Welch, “Potential and Pitfalls of Therapy with ⎵ -Particles,” vol. 46, no. 8, pp. 1254–1255, 2005.

[77] R. M. De Kruijff, H. T. Wolterbeek, and A. G. Denkova, “A Critical Review of Alpha Radionuclide Therapy — How to Deal with Recoiling Daughters ?,” pp. 321–336, 2015, doi: 10.3390/ph8020321.

[78] S. Poty, L. C. Francesconi, M. R. Mcdevitt, M. J. Morris, and S. Jason, “Alpha Emitters for Radiotherapy : Basic Radiochemistry to Clinical Studies _ Part 1,” pp. 1–26, 2018, doi: 10.2967/jnumed.116.186338.

[79] M. D’Huyvetter, C. Xavier, V. Caveliers, T. Lahoutte, S. Muyldermans, and N. Devoogdt, “Radiolabeled nanobodies as theranostic tools in targeted radionuclide therapy of cancer,” *Expert Opin. Drug Deliv.*, vol. 11, no. 12, pp. 1939–1954, 2014, doi: 10.1517/17425247.2014.941803.

[80] L. Marcu, E. Bezak, and B. J. Allen, “Critical Reviews in Oncology / Hematology Global comparison of targeted alpha vs targeted beta therapy for cancer : In vitro , in vivo and clinical trials,” *Crit. Rev. Oncol. / Hematol.*, vol. 123, no. November 2017, pp. 7–20, 2018, doi: 10.1016/j.critrevonc.2018.01.001.

[81] S. V Gudkov, N. Y. Shilyagina, V. A. Vodeneev, and A. V Zvyagin, “Targeted Radionuclide Therapy of Human Tumors,” no. September, pp. 1–19, 2015, doi: 10.3390/ijms17010033.

[82] S. R. Cherry and M. Dahlbom, “PET: Physics, Instrumentation, and Scanners,” *Pet*, pp. 1–117, 2006, doi: 10.1007/0-387-34946-4_1.

[83] M. Maučec, R. Dusterhoft, R. Rickman, R. Gibson, and A. Buffler, “Imaging of Fluid Mobility in Fractured Cores Using Time-lapse Positron Emission Tomography SPE 166402-MS Imaging of Fluid Mobility in Fractured Cores Using Time-lapse Positron Emission Tomography,” no. March 2015, 2013, doi: 10.2118/166402.

[84] A. Ku, V. J. Facca, Z. Cai, and R. M. Reilly, “Auger electrons for cancer therapy – a review,” vol. 2, 2019.

[85] A. C. Freise and A. M. Wu, “In vivo imaging with antibodies and engineered fragments,” *Mol. Immunol.*, vol. 67, no. 2, pp. 142–152, 2015, doi: 10.1016/j.molimm.2015.04.001.

[86] L. M. Carter and S. Poty, “Preclinical optimization of antibody - based radiopharmaceuticals for cancer imaging and radionuclide therapy — Model , vector , and radionuclide selection,” no. November 2017, pp. 611–635, 2018, doi: 10.1002/jlcr.3612.

[87] K. Tsuchikama, “Antibody-drug conjugates : recent advances in conjugation and linker chemistries,” *Protein Cell*, vol. 9, no. 1, pp. 33–46, 2018, doi: 10.1007/s13238-016-0323-0.

[88] G. Farahavar and S. Abolmaali, “Biomaterials Science breakthrough therapeutic , diagnostic and,” no. Cdc, pp. 4000–4016, 2019, doi: 10.1039/c9bm00931.

[89] G. Sugiura, H. Kühn, M. Sauter, U. Haberkorn, and W. Mier, “Radiolabeling strategies for tumor-targeting proteinaceous drugs,” *Molecules*, vol. 19, no. 2, pp. 2135–2165, 2014, doi: 10.3390/molecules19022135.

[90] S. Liu and U. School of Health Sciences, Purdue University, West Lafayette, “Bifunctional Coupling Agents for Radiolabeling of Biomolecules and Target-Specific Delivery of Metallic Radionuclides,” *Adv Drug Deliv Rev.*, pp. 2135–2165, 2008, doi: doi:10.1016/j.addr.2008.04.006.

[91] X. Zhang, Y. Zhang, and A. Malhotra, “Radiolabeling in Biology,” pp. 1–10, 2015, doi: 10.1007/s12013-014-0416-4.

[92] P. Dennler, E. Fischer, and R. Schibli, “Antibody Conjugates: From Heterogeneous Populations to Defined Reagents,” pp. 197–224, 2015, doi: 10.3390/antib4030197.

[93] L. M. De León-rodríguez and Z. Kovacs, “The Synthesis and Chelation Chemistry of DOTA - Peptide Conjugates,” vol. 19, no. 2, 2008.

[94] H. Jadvar, H. Jacene, and M. Graham, “Book Reviews Molecular Imaging : An Introduction,” p. 209635, 2018, doi: 10.2967/jnumed.118.209635.

[95] M. Wu, “Multimodal Molecular Imaging : Current Status and Future Directions,” vol. 2018, 2018, doi: 10.1155/2018/1382183.

[96] H. Saji, “In Vivo,” vol. 40, no. 10, pp. 1605–1615, 2017.

[97] G. Pirovano, S. Roberts, S. Kossatz, and T. Reiner, “Optical Imaging Modalities : Principles and Applications in Preclinical Research and Clinical Settings,” pp. 1419–1427, 1852, doi: 10.2967/jnumed.119.238279.

[98] K. Wang *et al.*, “Medical Instrumentation — Review Op tical Molecular Imaging Frontiers in Oncology : The Pursuit of Accuracy and Sensitivity,” vol. 1, no. 3, pp. 309–323, 2015, doi: 10.15302/J-ENG-2015082.

[99] A. Drzezga *et al.*, “First Clinical Experience with Integrated Whole-Body,” pp. 845–855, doi: 10.2967/jnumed.111.098608.

[100] M. E. Mayerhoefer *et al.*, “PET / MRI versus PET / CT in oncology : a prospective single-center study of 330 examinations focusing on implications for patient management and cost considerations,” pp. 51–60, 2020.

[101] J. Li, J. Van Valkenburgh, X. Hong, P. S. Conti, X. Zhang, and K. Chen, “Theranostics Small molecules as theranostic agents in cancer immunology,” vol. 9, no. 25, 2019, doi: 10.7150/thno.37218.

[102] A. Del Guerra, N. Belcari, and M. B. Giuseppina, “Positron Emission Tomography : Its 65 years,” no. April, 2016, doi: 10.1393/ncr/i2016-10122-6.

[103] A. A. M. Van der Veldt, E. F. Smit, and A. A. Lammertsma, “Positron emission tomography as a method for measuring drug delivery to tumors in vivo: The example of [11C]docetaxel,” *Front. Oncol.*, vol. 3 AUG, no. August, pp. 1–7, 2013, doi: 10.3389/fonc.2013.00208.

[104] H. J. Kim, A. Cho, M. Yun, Y. T. Kim, and W. J. Kang, “Comparison of FDG PET/CT and MRI in lymph node staging of endometrial cancer,” *Ann. Nucl. Med.*, vol. 30, no. 2, pp. 104–113, 2016, doi: 10.1007/s12149-015-1037-8.

[105] F.-M. Lu and Z. Yuan, “PET/SPECT molecular imaging in clinical neuroscience: recent advances in the investigation of CNS diseases.,” *Quant. Imaging Med. Surg.*, vol. 5, no. 3, pp. 433–47, 2015, doi: 10.3978/j.issn.2223-4292.2015.03.16.

[106] M. M. Khalil, J. L. Tremoleda, T. B. Bayomy, and W. Gsell, “Molecular SPECT Imaging : An Overview,” vol. 2011, 2011, doi: 10.1155/2011/796025.

[107] J. Maz, M. Allard, P. Fernandez, and W. Mayo, “SPECT Imaging of Cholinergic,” pp. 123–129, doi: 10.2967/jnumed.116.176180.

[108] C. Martelli, A. Lo Dico, C. Diceglie, G. Lucignani, and L. Ottobrini, “Optical imaging probes in oncology,” vol. 7, no. 30.

[109] M. C. Pierce, D. J. Javier, and R. Richards-kortum, “Optical contrast agents and imaging systems for detection and diagnosis of cancer,” *Int J Cancer.*, vol. 123, no. 9, pp. 1979–1990, 2008, doi: 10.1002/ijc.23858.

[110] F. Stuker, J. Ripoll, M. Rudin, and V. Vouton, “Potential for Pharmaceutical Research,” pp. 229–274, 2011, doi: 10.3390/pharmaceutics3020229.

[111] M. C. H. Hekman *et al.*, “Improved Intraoperative Detection of Ovarian Cancer by Folate Receptor Alpha Targeted Dual-Modality Imaging,” *Mol. Pharm.*, vol. 14, no. 10, pp. 3457–3463, 2017, doi: 10.1021/acs.molpharmaceut.7b00464.

[112] K. E. Day, L. Sweeny, B. Kulbersh, K. R. Zinn, and E. L. Rosenthal, “Preclinical comparison of near-infrared-labeled cetuximab and panitumumab for optical imaging of head and neck squamous cell carcinoma,” *Mol. Imaging Biol.*, vol. 15, no. 6, pp. 722–729, 2013, doi: 10.1007/s11307-013-0652-9.

[113] M. J. Whitley *et al.*, “A mouse-human phase 1 co-clinical trial of a protease-activated fluorescent probe for imaging cancer,” *Sci Transl Med*, vol. 8, no. 320, pp. 1–24, 2016, doi: 10.1126/scitranslmed.aad0293.

[114] R. Atreya *et al.*, “In vivo imaging using fluorescent antibodies to tumor necrosis factor predicts therapeutic response in Crohn’s disease Raja,” *Nat Med*, vol. 20, no. 3, pp. 313–318, 2014, doi: 10.1038/nm.3462.

[115] S. Salipalli, P. K. Singh, and J. Borlak, “Recent advances in live cell imaging of hepatoma cells,” pp. 1–16, 2014.

[116] R. M. Levenson, D. T. Lynch, H. Kobayashi, J. M. Backer, and M. V. Backer, “Multiplexing with multispectral imaging: From mice to microscopy,” *ILAR J.*, vol. 53, no. 1, pp. 78–88, 2012.

[117] D. A. Mankoff, J. M. Link, H. M. Linden, L. Sundararajan, and K. A. Krohn, “Tumor Receptor Imaging,” pp. 149–163, doi: 10.2967/jnumed.107.045963.

[118] G. Sgouros, L. Bodei, M. R. McDevitt, and J. R. Nedrow, “Radiopharmaceutical therapy in cancer: clinical advances and challenges,” *Nat. Rev. Drug Discov.*, vol. 19, no. 9, pp. 589–608, 2020, doi: 10.1038/s41573-020-0073-9.

[119] B. Salvatore, M. G. Caprio, B. S. Hill, A. Sarnella, G. N. Roviello, and A. Zannetti, “Recent Advances in Nuclear Imaging of Receptor Expression to Guide Targeted Therapies in Breast Cancer,” 2019.

[120] S. Sengupta, “Comparison of prostate - specific membrane antigen ligands in clinical translation research for diagnosis of prostate cancer,” no. November 2018, pp. 1–22, 2019, doi: 10.1002/cnr2.1169.

[121] K. A. Knapp *et al.*, “Evaluation of SAS1B as a target for antibody-drug conjugate therapy in the treatment of pancreatic cancer,” vol. 9, no. 10, pp. 8972–8984, 2018.

[122] M. A. Deri, B. M. Zeglis, L. C. Francesconi, and J. S. Lewis, “PET imaging with Zr : From radiochemistry to the clinic,” *Nucl. Med. Biol.*, vol. 40, no. 1, pp. 3–14, 2013, doi: 10.1016/j.nucmedbio.2012.08.004.

[123] T. J. Wadas, E. H. Wong, G. R. Weisman, and C. J. Anderson, “Coordinating Radiometals of Copper , Gallium , Indium , Yttrium , and Zirconium for PET and SPECT Imaging of Disease,” pp. 2858–2902, 2010, doi: 10.1021/cr900325.

[124] M. J. Merrick *et al.*, “Physics in Medicine & Biology Imaging and dosimetric characteristics of 67 Cu,” 2021.

[125] T. Fra, “Development of copper based drugs , radiopharmaceuticals and medical materials,” pp. 1089–1112, 2012, doi: 10.1007/s10534-012-9578-y.

[126] N. C. Okoye, J. E. Baumeister, F. N. Khosroshahi, H. M. Hennkens, and S. S. Jurisson, “Chelators and metal complex stability for radiopharmaceutical applications,” vol. 107, pp. 1087–1120, 2019.

[127] K. L. Haas and K. J. Franz, “Application of Metal Coordination Chemistry to Explore and Manipulate Cell Biology,” vol. 109, no. 10, pp. 4921–4960, 2010, doi: 10.1021/cr900134.

[128] E. W. Price and C. Orvig, "Chem Soc Rev Matching chelators to radiometals for radiopharmaceuticals," pp. 260–290, 2014, doi: 10.1039/c3cs60304.

[129] A. Shrivastava, H. Ding, S. Kothandaraman, S. Wang, and L. Gong, "HHS Public Access," vol. 16, no. 5, pp. 661–669, 2018, doi: 10.1007/s11307-014-0727-2.

[130] D. Oushiki *et al.*, "Near-Infrared Fluorescence Probes for Enzymes Based on Binding," 2012, doi: 10.1021/ac300061.

[131] B. M. Zeglis and J. S. Lewis, "The Bioconjugation and Radiosynthesis of Zr-DFO-labeled Antibodies," no. February, pp. 1–8, 2015, doi: 10.3791/52521.

[132] A. Bansal *et al.*, "Novel 89 Zr cell labeling approach for PET-based cell trafficking studies," pp. 1–11, 2015, doi: 10.1186/s13550-015-0098-y.

[133] N. B. Bhatt, D. N. Pandya, and T. J. Wadas, "Recent advances in zirconium-89 chelator development," *Molecules*, vol. 23, no. 3, 2018, doi: 10.3390/molecules23030638.

[134] M. A. Deri *et al.*, "Melissa A. Deri, † , ‡ , § Shashikanth Ponnala, † , ‡ Brian M. Zeglis, † Gabor Pohl, ∥ J. J. Dannenberg, * , ∥ Jason S. Lewis, * , † and Lynn C. Francesconi * , ‡ , § †," 2014, doi: 10.1021/jm500389b.

[135] A. N. A. I. Faustino-rocha *et al.*, "Ultrasonography as the Gold Standard for In Vivo Volumetric Determination of Chemically-induced Mammary Tumors," vol. 472, pp. 465–472, 2016.

[136] I. Novak-hofer and P. A. Schubiger, "Review article Copper-67 as a therapeutic nuclide for radioimmunotherapy," vol. 29, no. 6, 2002, doi: 10.1007/s00259-001-0724-y.

[137] Thaddeus J. Wadas et al, "Coordinating Radiometals of Copper, Gallium, Indium, Yttrium and Zirconium for PET and SPECT Imaging of Disease," *Chem Rev.*, vol. 110, no. 5, pp. 2858–2902, doi: 10.1021/cr900325.

[138] E. Boros and A. B. Packard, "Radioactive Transition Metals for Imaging and Therapy," 2019, doi: 10.1021/acs.chemrev.8b00281.

[139] J. K. Sosabowski and S. J. Mather, "Conjugation of DOTA-like chelating agents to peptides and radiolabeling with trivalent metallic isotopes," 2006, doi: 10.1038/nprot.2006.175.

[140] G. Schwarz, L. Mueller, and M. W. Linscheid, "DOTA based metal labels for protein quanti fi cation : a review," pp. 221–233, 2014, doi: 10.1039/c3ja50277.

[141] P. Debie and S. Hernot, "Emerging Fluorescent Molecular Tracers to Guide Intra-Operative Surgical Decision-Making," vol. 10, no. May, 2019, doi: 10.3389/fphar.2019.00510.

[142] H. S. Choi *et al.*, “Synthesis and In Vivo Fate of Zwitterionic Near-Infrared,” pp. 6258–6263, 2011, doi: 10.1002/anie.201102459.

[143] C. P. Toseland, “Fluorescent labeling and modification of proteins,” pp. 85–95, 2013, doi: 10.1007/s12154-013-0094-5.

[144] P. Debie *et al.*, “E ff ect of Dye and Conjugation Chemistry on the Biodistribution Pro fi le of Near-Infrared-Labeled Nanobodies as Tracers for Image-Guided Surgery,” 2017, doi: 10.1021/acs.molpharmaceut.6b01053.

[145] M. J. W. D. Vosjan *et al.*, “Conjugation and radiolabeling of monoclonal antibodies with zirconium-89 for PET imaging using the bifunctional chelate p -isothiocyanatobenzyl-desferrioxamine,” *Nat. Protoc.*, vol. 5, no. 4, pp. 739–743, 2010, doi: 10.1038/nprot.2010.13.

[146] P. Hong, S. Koza, E. S. P. Bouvier, and W. Corporation, “A review size-exclusion chromatography for the analysis of protein biotherapeutics and their aggregates,” pp. 2923–2950, 2012, doi: 10.1080/10826076.2012.743724.

[147] K. N. Baker *et al.*, “Rapid monitoring of recombinant protein products : a comparison of current technologies,” vol. 20, no. 4, pp. 149–156, 2002.

[148] L. M. Lechermann *et al.*, “Detection limit of 89 Zr-labeled T cells for cellular tracking : an in vitro imaging approach using clinical PET / CT and PET / MRI,” 2020.

[149] T. K. Nayak and M. W. Brechbiel, “Radioimmunoimaging with Longer-Lived Positron-Emitting Radionuclides : Potentials and Challenges,” pp. 825–841, 2009.

[150] H. Kvaternik, J. Gatterer, E. Plhak, J. F. Schwarzgruber, and H. Kvaternik, “Systematic Assessment of the Adsorption of 99m Tc- Radiopharmaceuticals onto Plastic Syringes,” pp. 1–21, 2019, doi: 10.2967/jnmt.119.235432.

[151] M. C. Chakrabarti, N. Le, C. H. Paik, W. G. De Graffand, and J. A. Carrasquillo, “Prevention of Radiolysis of Monoclonal Antibody during Labeling,” vol. 37, no. 8, pp. 1147–1151, 1996.

[152] P. R. Mcdonagh, G. Sundaresan, L. Yang, M. Sun, R. Mikkelsen, and J. Zweit, “Biodistribution and PET imaging of 89-zirconium labeled cerium oxide nanoparticles synthesized with several surface coatings,” *Nanomedicine Nanotechnology, Biol. Med.*, vol. 14, no. 4, pp. 1429–1440, 2018, doi: 10.1016/j.nano.2018.04.002.

[153] I. N. V. Biodistribution and A. Of, “IN VIVO BIODISTRIBUTION AND ACCUMULATION OF 89 Zr IN MICE,” vol. 38, no. 5, pp. 675–681, 2015, doi: 10.1016/j.nucmedbio.2010.12.011.IN.

[154] R. Raavé *et al.*, “Direct comparison of the in vitro and in vivo stability of DFO , DFO * and DFOcyclo * for 89 Zr-immunoPET,” pp. 1966–1977, 2019.

[155] E. S. Pires *et al.*, “Membrane associated cancer-oocyte neoantigen SAS1B / ovastacin is a candidate immunotherapeutic target for uterine tumors,” vol. 6, no. 30.

[156] R. Benedetto *et al.*, “Development of radioimmunoconjugate for diagnosis and management of head-and-neck subclinical cancer and colorectal carcinoma,” pp. 1–10, 2017.

[157] U. Karczmarczyk, W. Wojdowska, R. Mikołajczak, M. Maurin, and E. Laszuk, “Influence of DOTA Chelators on Radiochemical Purity and Biodistribution of 177 Lu- and 90 Y-Rituximab in Xenografted Mice,” vol. 17, no. October 2017, pp. 1201–1208, 2018.

[158] M. Y. Bartee and Æ. S. Lutsenko, “Hepatic copper-transporting ATPase ATP7B : function and inactivation at the molecular and cellular level,” pp. 627–637, 2007, doi: 10.1007/s10534-006-9074-3.

[159] I. Hamza, “yr ig,” no. January 2004, 2014, doi: 10.1007/978-1-4419-9034-1.

[160] J. Fan, T. Schoeb, T. V Strong, and E. L. Rosenthal, “NIH Public Access,” vol. 17, no. 1, pp. 49–57, 2015, doi: 10.1007/s11307-014-0773-9.IND-Directed.

[161] P. Nagy, “Article The Effect of Fluorophore Conjugation on Antibody Affinity and the Photophysical Properties of Dyes,” pp. 688–700, 2018, doi: 10.1016/j.bpj.2017.12.011.

[162] J. K. Yoon, B. N. Park, E. K. Ryu, Y. S. An, and S. J. Lee, “Current perspectives on 89Zr-PET imaging,” *Int. J. Mol. Sci.*, vol. 21, no. 12, pp. 1–18, 2020, doi: 10.3390/ijms21124309.

[163] A. J. Poot *et al.*, “Fully automated 89Zr labeling and purification of antibodies,” *J. Nucl. Med.*, vol. 60, no. 5, pp. 691–695, 2019, doi: 10.2967/jnumed.118.217158.

[164] N. Joubert *et al.*, “In vitro characterization and stability profiles of antibody–fluorophore conjugates derived from interchain cysteine cross-linking or lysine bioconjugation,” *Pharmaceuticals*, vol. 12, no. 4, 2019, doi: 10.3390/ph12040176.

[165] M. M. n, Eunsung Mouradian, “PET Imaging with 89 Zr: From Radiochemistry to the Clinic,” *Nucl Med Biol.*, vol. 23, no. 1, pp. 1–7, 2013, doi: 10.1016/j.nucmedbio.2012.08.004.PET.

[166] K. P. P. Javier E. Stern, Sookjin Son, Vinicia C. Biancardi, Hong Zheng, Neeru Sharma, “p-SCN-Bn-HOPO: A Superior Bifunctional Chelator for 89ZrImmunoPET,” *Bioconjug Chem.*, vol. 176, no. 1, pp. 139–148, 2015, doi: 10.1021/acs.bioconjchem.5b00572.p-.

Vita

Nouri Elmekharam was born on July 6th, 1971, in Tripoli, Libya, and he is a Libyan citizen. He received Bachelor degree in Medical Laboratory Science from Tripoli University, Libya in 1992. He worked as Medical laboratory technologist in Ali Omar Asker neurosurgery hospital. In January 2009, he received Master degree in Biomedical Engineering from The Libyan Academy of higher studies. Subsequently he worked at Tripoli University as teaching assistance. In 2014, he was awarded scholarship from the high education ministry of Libya to study for PhD degree in Chemical biology in USA. In August, 2015, he entered graduate school at Virginia Commonwealth University.